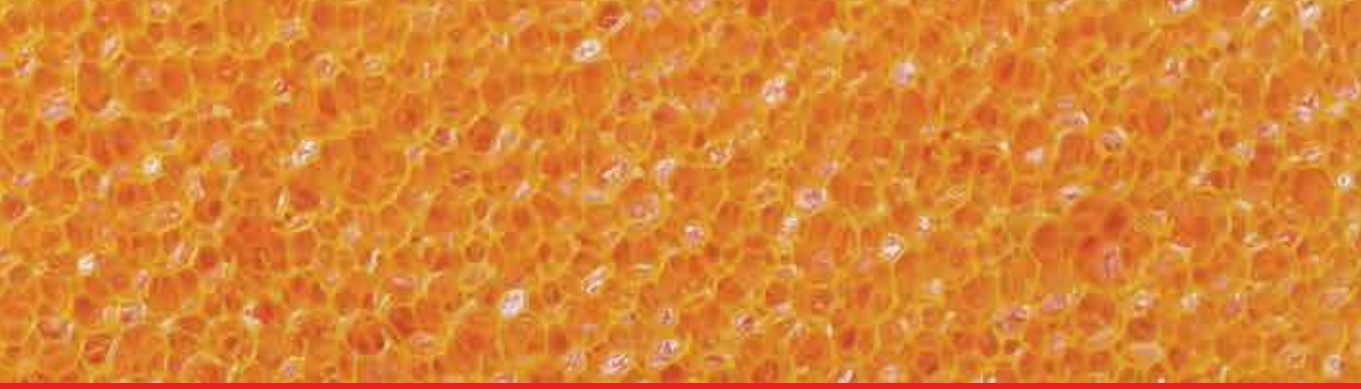

IntechOpen

Thermophysical Properties of Complex Materials

Edited by Aamir Shahzad

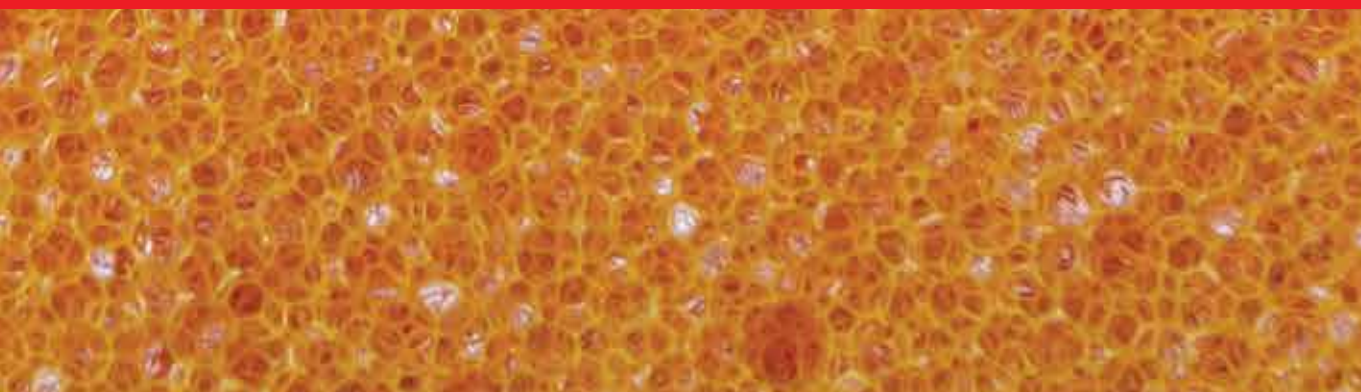

Thermophysical Properties of Complex Materials

Edited by Aamir Shahzad

Published in London, United Kingdom







IntechOpen






Supporting open minds since 2005

Thermophysical Properties of Complex Materials
http://dx.doi.org/10.5772/intechopen.81990
Edited by Aamir Shahzad

Contributors
Yong W Kim, Eric Kaiser, Mahmoud Ahmed, Mohamed Abdel Haddi, Hseen Baled, Isaac Gamwo, Fiseha Tesfaye, Mykola Moroz, Oleksandr Reshetnyak, Leena Hupa, Daniel Lindberg, Pekka Taskinen, G. Reza Vakili-Nezhaad, Ohoud Al Ghafri, Majid Al Wadhahi, Aamir Shahzad, Sukhmander Singh

First published in London, United Kingdom, 2020 by IntechOpen
IntechOpen is the global imprint of INTECHOPEN LIMITED, registered in England and Wales, registration number: 11086078, 7th floor, 10 Lower Thames Street, London, EC3R 6AF, United Kingdom
Printed in Croatia

British Library Cataloguing-in-Publication Data
A catalogue record for this book is available from the British Library

Additional hard and PDF copies can be obtained from orders@intechopen.com

Thermophysical Properties of Complex Materials
Edited by Aamir Shahzad
p. cm.
Print ISBN 978-1-78984-888-5
Online ISBN 978-1-78984-889-2
eBook (PDF) ISBN 978-1-83880-458-9

Meet the editor

Aamir Shahzad has over 14 years of experience of university research and teaching at home and abroad and due to his continuous efforts the thermophysical properties of materials was started at graduate and postgraduate levels. Dr. Shahzad received his postdoctoral and doctoral degrees from Xi'an Jiaotong University P.R. China in 2015 and 2012, respectively. He has proposed novel methods to explore the outcomes of complex materials, which shows his aptitude to comprehend computational physics and molecular modeling and simulations together with experimental understanding. Moreover, Dr. Shahzad is also exploring the fields of computational physics, complex fluids/plasmas, and, in addition, is currently working on plasma oncology and bio- and energy materials. Currently, Dr. Shahzad is working/has been promoted as a tenured associate professor in the Department of Physics, GC University Faisalabad (GCUF). Dr. Shahzad is a member of the ThermoPhysical Society of Xian Jiaotong University, China, and a member of the Physics Society GCUF and UAF, Pakistan.

Contents

Preface

This book introduces up-to-date information on the thermophysical properties (TPs) of complex materials. The TPs of complex materials is an interesting topic and a new frontier in applied science and technology that has applications in both basic and applied research. Recently, TPs have shown that modern advances in material development, experiments, and theoretical tools can embrace conventional refrigeration and power generation technologies. Device performance is a major task for TP control design and how material parameters can control devices. Different attempts have been made to increase the performance of devices with TPs and new improved methods are required for material structure efficiency from material parameters optimization. Considerable advances in this area have been made over the last few decades using a diverse set of theoretical, experimental, and computational techniques. This covers a wide spectrum of research areas in TPs, and is mainly based on the dusty plasmas and nanoscale materials in global universities.

The preferred research topics show a large range of well-matched syllabi that are presently being studied in different countries. The book consists of three sections with seven chapters and each section begins with fundamental ideas involving the TPs of materials, properties at the nanolevel, and complex plasmas, followed by a number of research issues and their clarifications. Developments in TPs are motivated by improvements in multidisciplinary areas of science and technology, including physics, chemistry, applied biology, engineering, and applied disciplines associated with routine applications (for instance, plasma oncology, semiconductor and chemical industries, etc.). This book is basically designed for postgraduate students of complex materials who need to formulate the establishment of information in this area. It is also a resource for interested readers from allied fields, for instance, materials science, plasma medicine, industrial technologies, energy production, and heating/cooling strategies. The first chapter provides a discussion on the structural behaviors of the transport properties of metallic alloys. The second chapter explains the modeling of viscosity and theory of entropy for hydrocarbons for a wide range of temperatures and pressures. The third chapter incorporates thermodynamics outcomes by using silver ionic conduction in solid-state electrolytes. In the fourth chapter, the authors elaborate on TPs at the nano-level. The fifth chapter provides experimental investigations into the dynamic viscosity of graphene and ferrous oxide-based nanofluids. In the sixth chapter, the authors tackle the thermal conductivity of complex dusty plasmas through molecular dynamics simulations. The final seventh chapter presents wave instabilities in Hall plasma devices.

Dr. Aamir Shahzad
Tenured Associate Professor,
Molecular Modeling and Simulation Laboratory,
Department of Physics,
Government College University,
Faisalabad, Pakistan

Key Laboratory of Thermo-Fluid Science and Engineering,
Ministry of Education (MOE),
Xi'an Jiaotong University,
People's Republic of China

Section 1

Thermophysical Properties of Materials

Chapter 1

Structural Disorder as Control of Transport Properties in Metallic Alloys

Eric R. Kaiser and Yong W. Kim

Abstract

Structural disorder is ubiquitous for a large class of metallic alloys. Such an alloy's transport properties are highly susceptible to change when the disorder is modified. A first-principle method has been developed for modeling of disorders in metallic alloys. In this approach, an alloy specimen is regarded as a randomly close-packed mixture of a population of nanocrystallites and constituent atoms in glassy state. The disorder is then represented by the size distribution function of the nanocrystallites. Under sustained exposure to thermal, stress, nuclear or chemical forcing at an elevated temperature, the distribution function becomes modified, and this process is predictable for a given forcing condition, and thus controllable. Transport of excitations is affected by the detail of the distribution function, making it possible to control transport properties, all at a fixed alloy composition. The modeling and experimental support will be presented.

Keywords: structural disorder, transport property, metallic alloys, thermal forcing

1. Modeling of structural disorder in alloys by nanocrystallites

Structural disorder is common in solid materials of daily use in general. The situation is particularly true of metallic alloys that define the scope and functionality of the myriad objects and structures that are devised of such alloys. The appropriate properties of metallic materials range from their intrinsic strength, resistance against shape change, the wide span of dimensions a metal may be worked into, myriad ways metallic objects may be assembled into different structures, wide temperature spans a metallic object may stably exist for a long period of time to the wide range of heat transport such metallic media can sustain. The listing of different thermophysical properties of metallic alloys appropriate for these applications can be rather extensive. In the great majority of cases, the regularity in the assembly of constituent atoms into a solid specimen plays a critical role. The degree of such regularity determines the material's ability to define its thermophysical properties. All of these properties are subject to structural disorder in the given metallic alloy medium.

Our group has formulated the world's first modeling approach to disordered metallic alloys in the past few years [1]. Each material specimen is modeled as a randomly-close packed assembly of constituent atoms in glassy state and an ensemble of nanocrystallites varying in size as large molecules. There is, however,

no single canonical view of the state of random close packing for a given material specimen but only a statistical view [2]. In order to help sharpen the scope of the disorder in alloys we have utilized a surrogate macroscopic material specimen in a two-dimensional assembly of steel spheres. The simulated material specimen is thermalized by driving the assembly in two mutually orthogonal directions by two independent stepping motors under digital control. The motors are driven by using a sequence of instructions derived from a chaotic algorithm. The simulated material specimen is continuously video imaged as a function of time, which is then analyzed for particle positions; the entire field of view is analyzed and reconstituted into a movie as a function of time. Analysis of the resulting sequence of particle positions shows that some of the single particles cluster into, and break out of, nanocrystallites in time. We thus obtain as a function of time the size-resolved distribution of nanocrystallites that are randomly close packed with single glassy particles in the simulated alloy medium. The size distribution is found to be stationary at each given intensity setting of the drive.

Operation of the digitally controlled drive of the simulated alloy specimen is fine tuned in such a way that the distribution of single particle velocities becomes Maxwellian to a high degree. When the digital drive intensity is changed, the single particle velocity distribution broadens or narrows linearly with the drive intensity to a good approximation. This feature provides the means to vary "the temperature" of the simulated specimen. The significant and interesting find is that the nanocrystallite size distribution function shows significant changes as the effective temperature of the simulated specimen increases. Here we find a nanocrystallite when it is composed of three or more particles where each constituent particle is in contact with two or more other particles within the nanocrystallite. The shape and size of nanocrystallites within the simulated alloy specimen change as a function of time but the average population of nanocrystallites maintains a stable functional form as a function of nanocrystallite size as defined by the number of constituent single particles.

2. Equilibrium nanocrystallite size distribution

The theoretical modeling formalism is thus constructed by means of the law of mass action. Nanocrystallites are regarded as large molecules that are mixed in the sea of single glassy particles. In the course of local fluctuations, nanocrystallites grow larger by merging or attachment, or become smaller by losing peripheral particles or breaking up into smaller nanocrystallites. This process maintains a detailed balance throughout over long time, much like the dissociation equilibrium in a gas medium consisting of large molecules mixed in a gas of monatomic particles.

As the medium temperature is increased toward the melting point of the given alloy, the population of nanocrystallites undergoes rapid large changes per unit change in temperature. Overall, nanocrystallites decrease in number density, and the medium becomes more populated by single atoms in glassy state. This pattern of temperature dependence is universal throughout metallic alloys. We model this phenomenon as equilibrium dissociation of nanocrystallites in the randomly close packed medium of glassy atoms and nanocrystallites in equilibrium.

By means of this theoretical framework, the temperature dependence of nanocrystallite populations has been computed for 44 different metals. They all follow the pattern of temperature dependence as outlined above. There are, however, small but distinct differences in these patterns of temperature dependence that are particular to the atomic properties of given metals. In order to formulate a realistic first order theory of alloys, we proceed to quantify the differences by grouping different alloys, according to their crystalline symmetry properties.

In this modeling we aim to model the nanocrystallites of different metals as realistically as known in solid state alloy literature. We first assert that all nanocrystallites are spherical in shape. Each nanocrystallite is cookie-cut out of the large lattice of the given alloy in such a way that the sphere of given radius contains the number of atoms in each given nanocrystallite. Since there are one or more ways this operation may be carried out depending on the crystalline symmetry property of the given alloy, all different versions of the sphere are considered in the subsequent dissociation potential calculations, and their average is taken in the final look-up table of dissociation potentials of atoms on the surface of each nanocrystallite. The interaction potentials between all possible pairs of atoms found in the nanocrystallite are calculated according to the interaction potentials of Lennard-Jones (L-J) type that have been obtained from quantum chemistry computation [3]. The L-J potentials are applied to find the dissociation potential for each of the atoms on the periphery of each given nanocrystallite in question. The dissociation potential computed in this manner grows larger asymptotically with increasing size of the nanocrystallite; the computed results are best fitted into a lookup table of dissociation potentials as a function of nanocrystallite size [1]. Individual values of the dissociation potential are obtained from the look-up table for the law of mass action calculation for the alloy in equilibrium.

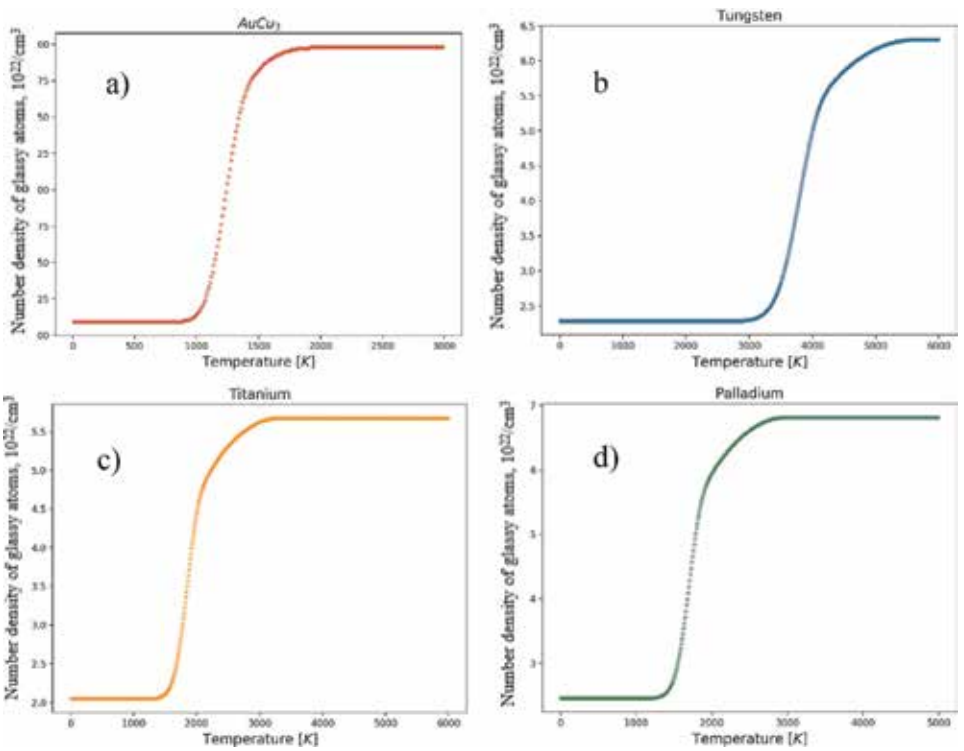

Figure 1.
Calculated number of glassy state atoms per cc as a function of temperature for: (a) binary alloy—$AuCu_3$ (1240.5 K); (b) BCC—tungsten (3695 K); (c) HCP—titanium (1948 K); and (d) FCC—palladium (1828 K). The melting points of the metals are listed in the parentheses. Operationally, we take the melting point to be at midpoint between the minimum and the maximum of the number density of glassy atoms, and this is in good agreement with the known data. By taking the midpoint between the maximum and the minimum number density. At room temperature when the population of nanocrystallites is largest, in each plot the number density of glassy state atoms starts off at the particular value, corresponding to its own randomly close packed state. In the case of $AuCu_3$ the number density of glassy state atoms at room temperature is 4.1×10^{22} atoms per cm^3. The rest of the atoms are tied up in the form of nanocrystallites with the degree of crystallinity at 0.314; the number of glassy state atoms increases to 5.98×10^{22} atoms per cm^3 when the specimen is fully molten [4].

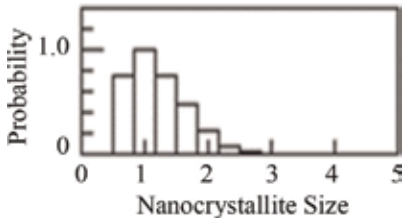

Figure 2.
Histogram by size of nanocrystallites of the single-element alloy at room temperature. Both the size axis (horizontal) and the probability axis (vertical) are shown in dimensionless form, the size as a fraction of the maximal size and the probability in fraction of the probability at the maximal size [1].

The result of such a calculation is shown in **Figure 1** for a gold-copper alloy. The calculation is carried out for the specimen of 1 cm^3 in volume. At room temperature, the degree of crystallinity is 0.314. The crystalline part of the specimen is in the form of nanocrystallites, whose size distribution function is shown in the histogram shown in **Figure 2**. The law of mass action is written out for each group of nanocrystallites of given size. Using the look-up table of dissociation potentials as a function of nanocrystallite size, the full complement of the coupled dissociation equations are solved numerically to find the number of atoms in glassy state as a function of temperature. The detailed procedure of iterative computation is described in detail elsewhere [1].

A perusal of **Figure 1** shows that the equilibrium population of glassy state atoms grows larger with increasing temperature for all different forms of metallic materials. The range of active temperature dependence is centered about the respective melting point in the form of a hyperbolic tangent function when the zero-crossing point of the function is aligned with the point of maximal slope. In fact, the temperature at which the slope of the function maximizes has a close match with the known melting point of the alloy [1]. On the other hand, there are a couple of small but definite differences among the four groups of alloys represented in **Figure 1**: one, the computed population of glassy atoms versus temperature is not symmetric about the maximal slope point; and two, the asymmetry varies on average according the crystalline lattice symmetry property of each given group of metals. We recognize that the asymmetry is reminiscent of the manner in which dissociation of molecules undergo in molecular gases or in plasma of gas mixtures of molecules and atomic gases as a function of temperature [1].

We have thus explored ways in which all groups of alloys of interest may be represented by a single function for the manner in which these alloys undergo structural transformation under thermal forcing. The hyperbolic tangent function is rewritten in such a way that the argument switches from one scaling with temperature below the melting point to another above it, and it is shifted upward so that its value remains bounded between zero and a positive constant.

3. Response of nanocrystallites to heating: a first order representation

The law of mass action calculation shows that when the temperature is increased through the melting point, the number of glassy atoms in the alloy specimen increases in the form of hyperbolic tangent (see **Figure 1**) to reach an asymptotic value in the limit of full melting. This pattern holds for all 44 metals for which the computation has been carried out (38 pure metals and six alloys) [5]. There are small but noticeable deviations from the ideal hyperbolic tangent profile: one, the functional form of the changing glassy atom population as a function of temperature is not exactly symmetric about the melting point; and two, the asymmetry is

dependent on the symmetry group of the metals. The width to melting temperature ratio is 0.139 ± 0.012 for BCC metals, 0.160 ± 0.010 for FCC, 0.177 ± 0.008 for HCP and 0.161 ± 0.016 for binary alloys. The two deviations mentioned above appear to reflect the groupings of the asymmetry.

The general shape of the number density of glassy atoms as a function of temperature rises from the glassy atom density at room temperature (n_0) to the maximum value ($n_{\max}$) past the melting point. The results shown in **Figure 1** are found from the system of the law of mass action equations; the number density of glassy atoms is always positive. The functional relationship may be well represented by the hyperbolic tangent function with the following modification:

$$n_g(T) = \frac{n_{max} + n_0}{2} + \frac{n_{max} - n_0}{2} tanh\left[s(T)\left(T - T_{mp}\right)\right] \tag{1}$$

Note that $n_{\max} = n_0 + \sum_{j=3}^{j_{max}} j n_{nanocrystallite}(j)$, where $n_{nanocrystallite}(j)$ denotes the number density of j-atom nanocrystallites at room temperature. s(T) is a switching function introduced in order to model the asymmetry in the glassy atom density about the melting point:

$$s(T) = \begin{cases} \eta, & T < T_{mp} \\ \lambda T_{mp}/T, & T \geq T_{mp} \end{cases} \tag{2}$$

Here η and λ are fitting constants for the computed glassy atom density versus temperature plot; they vary from one metallic specimen to another. T_{mp} denotes the melting point.

The goal here is to find a set of fitting parameters that will accurately capture the shape of all nanocrystallite species within each crystalline symmetry group (i.e., FCC, BCC, HCP and binary). We first normalize the fit with the following by introducing $T^* = T/T_{\mathrm{mp}}$, $n^* = [n_{\mathrm{g}}(T) - n_0]/(n_{\max} - n_0)$ and $s^* = s(T)\ T_{\mathrm{mp}}$. The fit to the computed glassy atom density becomes

Crystalline Symmetry	η^*	λ^*	Metals
FCC	8.84 ± 0.48	5.37 ± 0.32	*Ag, Al, Au, Ca, Ce, Cu, Ir, Ni, Pb, Pd, Pt, Rh, Th*
BCC	9.07 ± 0.96	7.74 ± 0.19	*Ba, Cr, Fe, K, Li, Na, Nb, Rb, Ta, V, W*
HCP	8.51 ± 0.67	5.22 ± 0.23	*Be, Cd, Co, Dy, Er, Hf, Mg, Re, Ru, Ti, Tl, Y, Zn, Zr*
Binary	8.48 ± 0.34	7.34 ± 0.91	*AlTi, Al_3Ti, $AlTi_3$, AuCu, Au_3Cu, $AuCu_3$*
Combined	8.74	6.19	

Table 1.
Summary table of normalization constants (η^* and λ^*) for four different groups of metals. The two constants for the entire group as combined are shown as combined normalization constants.

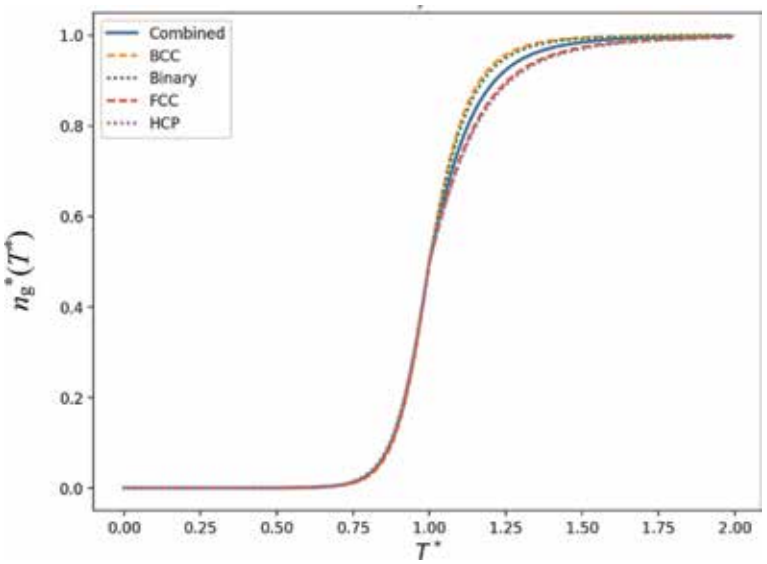

Figure 3.
Normalized best-fit plot of the computed glassy atom density as a function of temperature. The computed glassy atom density versus temperature plots for the alloys in the four different groups are rescaled into one combined fit (solid line). The four subgroup plots are shown individually, according to the legend within the figure. They appear evenly spread out on the two sides of the combined fit solid-line plot.

$$n_g^*(T) = \frac{1}{2} + \frac{1}{2} tanh[s^*(T^* - 1)] \tag{3}$$

where

$$s^* = \begin{cases} \eta^*, & T^* < 1 \\ \lambda^*/T^*, & T^* \geq 1 \end{cases} \tag{4}$$

The fitting parameters η^* and λ^* for the four groups of metals are tabulated together with their combined average values in **Table 1**. The list of metals in each individual crystalline symmetry group is given (**Figure 3**).

4. Effect of nanocrystallite size distribution on thermophysical properties

4.1 Annealing and thermal forcing

The dissociation potential of an atom on the surface of a nanocrystallite represents the energy needed to displace the atom to infinity and is of the order of several electron volts, depending on nanocrystallite size and alloy elements. On the other hand, rapid quenching involved in alloy-making leaves many constituent atoms small distances away from their local equilibria, fractions of an electron volt away in energy. This is where thermal forcing differs from annealing in the temperature scale.

Atomic transport is very slow in a metallic alloy medium compared with gaseous media even at elevated temperatures. Consequently, defects in the medium require long relaxation times. The computed number density of glassy atoms at elevated temperatures can be realized only when heating is sustained for very long times. Our laboratory experiments show that thermal forcing requires sustained heating of alloy specimens often for upward to 15 h at each temperature to fully realize the

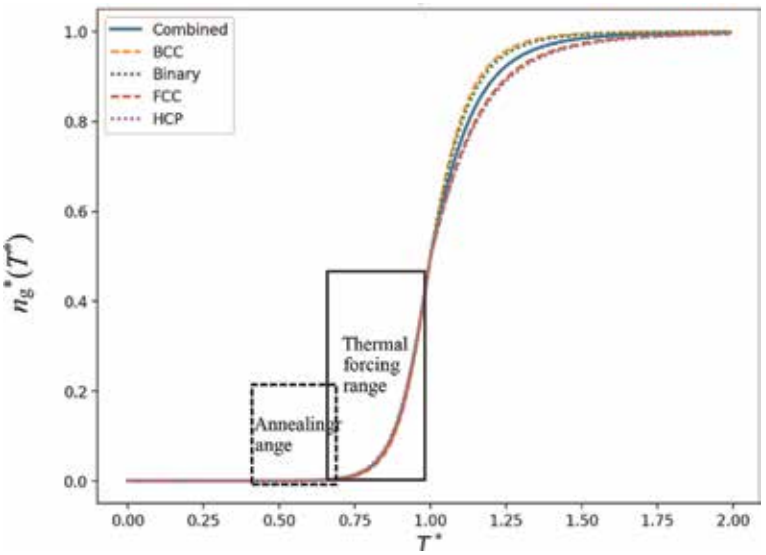

Figure 4.
Annealing and thermal forcing regimes of disordered alloys.

changes in the size distribution function of nanocrystallites. **Figure 4** shows two distinct opportunities for effecting significant changes in the transport properties of metallic alloy specimens.

4.2 Linear thermal expansion coefficient

Theory predicts decrease of the size of nanocrystallites and their number densities with increasing temperature. The temperature dependence of specimen's thermal expansion coefficient $\alpha(T)$ of a disordered alloy specimen would show a nonlinear scaling due to the change in the size distribution of nanocrystallites:

$$\alpha(T) = \gamma(T)\alpha_c(T) + [1 - \gamma(T)]\alpha_g(T) \tag{5}$$

Here $\gamma(T)$ denotes the degree of crystallinity, the probability that an atom is part of nanocrystallites within the specimen at temperature T. $\alpha_c(T)$ is the linear thermal expansion coefficient of the alloy in crystalline form, whereas $\alpha_g(T)$ signifies the linear thermal expansion coefficient of the alloy in fully glassy form. The expansion coefficient of the disordered specimen becomes nonlinear in its temperature dependence because of two different physics at play: one, the disordered specimen is an admixture of two materials that are compositionally identical but structurally different with different mass densities, and different thermal expansion properties; and two, the degree of crystallinity of the specimen, i.e., the fraction of the crystalline part of the specimen, changes when the specimen is thermally forced [6, 7]. **Figure 5** shows the degree of crystallinity computed for $AuCu_3$ as a function of temperature.

4.3 Speed of sound

The general trend of the changes in transport properties, when the specimen's degree of crystallinity is changed under thermal forcing, has been clearly demonstrated in an experiment on sound speed [7]. The measurement with a fresh specimen at room temperature gives the time of sound propagation over the specimen length of 38.2 mm at 90.2 ± 0.9 ms. After the thermal forcing run at 940 K for

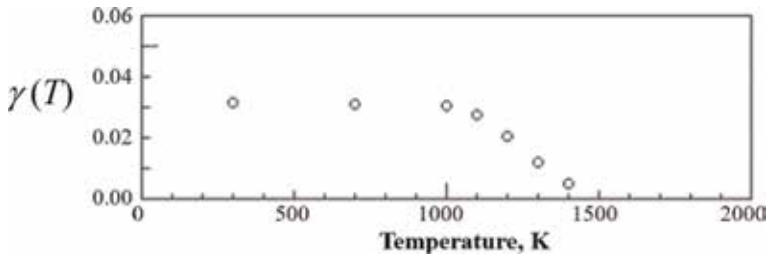

Figure 5.
The degree of crystallinity versus temperature for $AuCu_3$.

16.45 h and quenched in water, the corresponding time of sound propagation at room temperature is found to be 66.5 ± 1.8 ms. The thermal forcing run at 940 K is clearly a case of alloy annealing. For the specimen of 55 × 45 W% copper-nickel alloy, the melting point is 1543 K, which puts the forcing temperature of 940 K at 60.9% of the melting point. **Figure 4** shows the temperature to be in the alloy annealing regime; the temperature is not high enough to cause dissociation of nanocrystallites and affect their population significantly. The result above shows that the effect of thermal annealing on sound propagation is quite strong. It is in a way not surprising because sound propagation entails small movement of lattice spacing and annealing has nudged atoms within the specimen into positions of deeper binding energies that can be accessed within the thermal energy budget of the order of $k_B T$, or of the order of 0.1 eV. The dissociation potential for removal of an atom from the surface of a nanocrystallite is several eV.

4.4 Diffusion and thermal conduction

The temperature driven changes in the degree of crystallinity forces other thermophysical properties of the alloy specimen to undergo changes also. The temperature dependence of the transport properties, such as thermal conductivity, viscoelasticity, thermal expansion, electrical conductivity and many others, may be estimated approximately by treating the material specimen as a mixture of crystalline and glassy parts whose mixing ratio is variable as a function of temperature after a sustained heating. It is reasonable, however, to anticipate that the estimate may require a higher order correction when the forcing is further intensified.

Quantitative modeling of the temperature dependence of the alloy's transport properties may be addressed in a number of different ways:

i. An alloy specimen may be treated as two slabs of different lattice constants joined linearly. This approach may require appropriate modeling of the issues associated with transmission of excitations at the interface between the two slabs.

ii. Formal analyses may require separate considerations of phonon modes in nanocrystallites versus in the glassy medium. Additional issues of interest may include the structure of the atom pair distribution function and the distribution of coordination numbers.

iii. Computation of the transport properties by the method of Monte-Carlo simulation may entail sending off of random walkers at a given flux at one end of the alloy specimen. Meandering of the walkers and their arrivals at the other end through the medium of glassy matter and nanocrystallites can be tabulated. The alloy medium would be composed of a sampling of glassy atoms and of nanocrystallites, according to the solution of the system of the

law of mass action equations. The Monte-Carlo computation is carried out repetitively at a given temperature in order to develop a sufficiently large ensemble of events.

The size distribution of nanocrystallites evolves under thermal forcing as a function of temperature, and they affect the transport of excitations. In addition, scattering and transmission of random walkers at interfaces of glass-nanocrystallite and nanocrystallite-glass are also likely to play rate-controlling roles.

iv. Alloy specimen may be viewed as a network of interconnections (edges) between atoms. Edges between nanocrystallites are treated as linkages whose resistance to transport of excitation would be governed by the properties of the glassy medium as conduits. Differently from the Internet that carries information without delay or attenuation, the edges would bear the effects of time delays, signal attenuation and transmission speed. Nanocrystallites with multiple degrees (the number of edges) act as relay stations with delay constants that stem from the size of nanocrystallites and branching of the transmission of excitation. While many details of excitation transmission through nanocrystallites have to be worked out, the method holds promise as one with greatest potential [8].

5. Concluding remarks

Disordered metallic alloys have been modeled as a randomly close packed medium of glassy atoms and nanocrystallites of varying size. The model has been implemented by means of a large set of coupled algebraic equations, derived from the law of mass action relations in thermal equilibrium. The size distribution function of the nanocrystallites has been measured from a simulated alloy model in two-dimensions. The size distribution function has been found to depend on the alloy composition. The large system of dissociation equations is solved numerically for the population of constituent species as a function of temperature for 44 different metallic specimens. The theory predicts the degree of crystallinity changing for these alloys as a function of temperature. The melting point is found quite naturally in this alloy model calculations within 5–10% of known values.

It shows that the alloy's thermophysical properties can be changed by changing the size distribution of nanocrystallites. Sustained exposure to thermal forcing can exactly effect the change. By extension, the change of the nanocrystallite size distribution can be affected by means of chemical, mechanical stress or nuclear forcing at sustained elevated temperatures as well. We have shown that the change in the nanocrystallite size distribution function can be predicted by the first-principle model of structurally disordered alloys.

The modeling approach is based on the first-principle method of statistical physics. The model can be further refined and customized for any disordered metallic specimen. The model provides a roadmap for annealing and thermal forcing of disordered alloys. The interesting question is what mechanisms are responsible for the formation of nanocrystallites in metallic solids in the first place. Our continued investigation with the simulated alloy in two-dimensions strongly suggests that the structural disorder in metallic solids appear to originate from vortex-like flow patterns in liquid phase; at phase transition the flow patterns are solidified into disordered structures without recourse for relaxation due to specimen-wide slowing of dynamical processes [9, 10].

Author details

Eric R. Kaiser and Yong W. Kim*
Department of Physics, Lehigh University, Bethlehem, Pennsylvania, USA

*Address all correspondence to: ywk0@lehigh.edu

References

[1] Cress RP, Kim YW. Statistical physics modeling of disordered metallic alloys. In: Glebovsky V, editor. Progress in Metallic Alloys. Rijeka, Croatia: InTech; 2016. pp. 17-43

[2] Berryman JG. Random close packing of hard spheres and disks. Physical Review A. 1983;**27**:1053

[3] Zhen S, Davies GJ. Calculation of the Lennard-Jones N-m potential energy parameters for metals. Physica Status Solidi. 1983;**78**:595

[4] Kim YW, Cress RP. Effects of thermal forcing on morphology of disordered binary metallic alloys: Local equilibration and modification of near-surface elemental composition. High Temperatures-High Pressures. 2011;**40**:335

[5] Cress RP, Kim YW. Computed data files, unpublished. 2013

[6] Kim YW, Cress RP. Modeling of disordered binary alloys under thermal forcing: Effect of nanocrystallite dissociation on thermal expansion of $AuCu_3$. International Journal of Thermophysics. 2016;**37**:111

[7] Kim YW, Raffield RH. Sound propagation in thermally-forced copper-nickel alloy. High Temperatures-High Pressures. 2017;**46**:271

[8] Albert R, Barabasi AL. Statistical mechanics of complex networks. Reviews of Modern Physics. 2002;**74**:47

[9] Berthier L. Dynamic heterogeneity in amorphous materials. Physics. 2011;**4**:42

[10] Salez T, Salez J, Dalnoki-Veress K, Raphaël E, Forresta JA. Cooperative strings and glassy interfaces. PNAS. 2015;**112**:8227

Chapter 2

Viscosity Models Based on the Free Volume and Entropy Scaling Theories for Pure Hydrocarbons over a Wide Range of Temperatures and Pressures

Hseen O. Baled and Isaac K. Gamwo

Abstract

Viscosity is a critical fundamental property required in many applications in the chemical and oil industry. Direct measurements of this property are usually expensive and time-consuming. Therefore, reliable predictive methods are often employed to obtain the viscosity. In this work, two viscosity models based on the free-volume and entropy scaling theories are assessed and compared for pure hydrocarbons. The modeling results are compared to experimental data of 52 pure hydrocarbons including straight-chain alkanes, branched alkanes, cycloalkanes, and aromatics. This study considers viscosity data to extremely high-temperature and high-pressure (HTHP) conditions up to 573 K and 300 MPa. The results obtained with the free-volume theory viscosity in conjunction with the perturbed-chain statistical associating fluid theory (PC-SAFT) equation of state are characterized by an overall average absolute deviation (AAD%) of 3% from the experimental data. The overall AAD% obtained with the predictive entropy scaling method by Lötgering-Lin and Gross is 8%.

Keywords: high temperature, high pressure, hydrocarbons, modeling, viscosity

1. Introduction

Viscosity is a key property in many engineering disciplines, including chemical and petroleum engineering. For instance, viscosity influences the fluid flow through porous media and pipelines; hence, it is required for the design of pipelines and transport equipment as well as for the estimation of recoverable oil and flow rates in porous media or wellbores. Viscosity can be determined through experimental measurements. However, carrying out viscosity measurements at all conditions of interest is not only expensive and time-consuming but also may not be possible at extreme conditions such as those encountered in ultra-deep reservoirs including pressures up to 300 MPa and temperatures up to 573 K. Reliable prediction models provide an alternative approach to generating predicted and correlated viscosity data at conditions where experimental data are not readily available.

Unlike the viscosity of gases at low pressures which is well defined by the kinetic theory of the gases, the viscosity theory of liquids is still inadequately developed due to the complications caused by the intermolecular forces between the molecules [1]. Therefore, there is no widely accepted simple theoretical method for predicting liquid viscosities, and most estimation techniques used for viscosity prediction of liquids are of empirical or semiempirical nature. The empirical models are correlations based on experimental observation with no theoretical background, whereas semi-theoretical models have a fundamental basis but contain adjustable parameters determined by fitting the model to experimental data.

In the present study, two viscosity models based on the free-volume and entropy scaling theories are assessed and tested against viscosity data for pure hydrocarbons from different chemical families that are commonly found in crude oil at high-temperature and high-pressure (HTHP) conditions up to 573 K and 300 MPa. Pure components are well-suited for initial evaluation of the viscosity models because a viscosity model that has difficulty in correctly describing the viscosity of a single hydrocarbon is likely to fail when predicting multicomponent mixtures.

2. Free-volume theory (FVT)

The FVT model is based on the free-volume concept. The idea that the viscosity depends upon the free space was first introduced by Batschinski [2] about 100 years ago. The viscosity, η, can be expressed as a sum of two contributions given in Eq. (1):

$$\eta = \eta_0 + \Delta\eta \tag{1}$$

where η_0 is the dilute gas viscosity and the $\Delta\eta$ term dominates for liquid viscosity. The dilute gas term η_0 is determined from the kinetic gas theory at very low pressures. It should be noted, though, that for liquids and supercritical fluids, the dilute gas viscosity term η_0 is negligibly small in comparison to the total viscosity η; hence, η_0 can be neglected for such fluids. Doolittle [3] found that the viscosity of liquid n-alkanes can be represented by a simple function of the free space fraction, $f_v = \frac{v_f}{v_0} = \frac{v - v_0}{v_0}$:

$$\eta = A \ \exp\left(B/f_v\right) \tag{2}$$

where v_0 is the molecular volume of reference or hard-core volume, v is the specific molecular volume, B is characteristic of the free-volume overlap, and A is a material-specific constant. A viscosity model based on the relation between free volume, friction coefficient, and viscosity has been proposed by Allal and coauthors [4, 5]:

$$\Delta\eta = A \ \exp\left(B/f_v\right) \tag{3}$$

where the free-volume fraction f_v was defined by means of the fluctuation-dissipation theory as

$$f_v \propto \left(\frac{RT}{E}\right)^{\frac{3}{2}} \tag{4}$$

where R is the gas constant and T is the temperature. In this expression, $E = E_0 + \frac{PM}{\rho}$, where $E_0 = \alpha\rho$ is related to the energy barrier that the molecule has to

overcome in order to diffuse, ρ is the density, and P is the pressure. The viscosity of the dense state is linked to the fluid microstructure using the friction coefficient, ζ, which is related to molecular mobility and to the diffusion of linear momentum:

$$\Delta\eta = \frac{\rho N_A \zeta L^2}{M} \tag{5}$$

where N_A is Avogadro's number and L is a characteristic molecular length parameter. By combining the relations between free volume, friction coefficient, and viscosity, the following expression was obtained for the viscosity:

$$\Delta\eta = \frac{\rho l\left(\alpha\rho + \frac{PM}{\rho}\right)}{\sqrt{3RTM}} \exp\left[B\left(\frac{\alpha\rho + \frac{PM}{\rho}}{RT}\right)^{3/2}\right] \tag{6}$$

The unit for the viscosity is [Pa·s], when all other variables are in SI units. The term $\frac{PM}{\rho}$ is linked to the energy necessary to form vacant vacuums required for the diffusion of the molecules. l is the characteristic length parameter in Å. The unitless parameter B is characteristic of the free-volume overlap. The density appears explicitly in Eq. (6), and hence the values of the free-volume theory parameters are directly dependent on whether experimental or calculated densities are used.

The three pure component parameters l, α, and B are determined by fitting Eq. (1) to experimental viscosity data. The use of the FVT requires density information, either experimental or calculated values. In this study, FVT is used in conjunction with the hybrid group-contribution perturbed-chain statistical associating fluid theory equation of state (G-C PC-SAFT EoS) [6] since this EoS provides reliable density predictions over wide ranges of pressure and temperature. In this equation, the PC-SAFT parameters are determined using two different sets of group-contribution (G-C) parameters for two pressure ranges: low-to-moderate pressures ($\lesssim$7 MPa) and high pressures ($\gtrsim$7 MPa).

3. Entropy scaling model by Lötgering-Lin and Gross (ES-LG)

The basic idea of this method is to relate the viscosity to the residual entropy. The residual entropy is defined as the difference between a real state value and ideal gas state value at the same temperature and density, $s_{res}(\rho, T) = s(\rho, T) - s^{id}(\rho, T)$. Lötgering-Lin and Gross [7] proposed a predictive entropy scaling method for viscosities using a group-contribution (G-C) method based on the group-contribution perturbed-chain polar statistical associating fluid theory equation of state (G-C PCP-SAFT EoS) [8, 9]. Lötgering-Lin and Gross linked the Chapman-Enskog viscosity to PCP-SAFT segments in terms of G-C parameters, with

$$\eta_{\mathrm{CE,\,gc}} = \frac{5}{16}\frac{\sqrt{M_{mol} k_{\mathrm{B}} T/\left(m_{\mathrm{gc}} N_{\mathrm{A}} \pi\right)}}{\sigma_{\mathrm{gc}}^2 \Omega_{\mathrm{gc}}^{(2,\,2)^*}} \tag{7}$$

where M_{mol} is the molar mass, k_{B} is the Boltzmann constant, and T is the absolute temperature, N_A is Avogadro's number, m is the segment number, σ is the segment diameter, and $\Omega^{(2,\,2)^*}$ is the reduced collision integral. The index gc indicates pure component parameters that are calculated with the group-contribution method based on G-C-PCP-SAFT EoS.

A reduced viscosity is then defined as

$$\eta^* = \frac{\eta}{\eta_{\mathrm{CE,\,gc}}} \tag{8}$$

where the pure component reduced viscosity, η_{i}^*, is empirically correlated as

$$\ln \eta_{\mathrm{i}}^* = A_{\mathrm{i}} + B_{\mathrm{i}}\, z + C_{\mathrm{i}} z^2 + D_{\mathrm{i}}\, z^3 \tag{9}$$

with

$$z = \frac{s_{\mathrm{res}}}{k_{\mathrm{B}} m_{\mathrm{gc,\,i}}} \tag{10}$$

The residual entropy, s_{res}, is calculated from the G-C-PCP-SAFT EoS originally proposed by Vijande et al. [8] and reparametrized by Sauer et al. [9]:

$$s_{\mathrm{res}}(\rho, T) = -\left(\frac{\partial a_{\mathrm{res}}}{\partial T}\right)_{\rho} \tag{11}$$

where $a_{\mathrm{res}} = A_{res}/N$ is the specific Helmholtz energy given by Gross and Sadowski [10]. N is the total number of molecules.

The viscosity parameters A_{i} to D_{i} of pure substances are obtained from parameters A_{α} to D_{α} of functional group α, respectively. The following empirical expressions are proposed by Lötgering-Lin and Gross [7] for mixing group-contribution parameters:

$$A_i = \sum_{\alpha} n_{\alpha,\,i} m_{\alpha} \sigma_{\alpha}^3 A_{\alpha} \tag{12}$$

$$B_i = \sum_{\alpha} \frac{n_{\alpha,\,i} m_{\alpha} \sigma_{\alpha}^3}{V_{tot,\,i}^{\gamma}} B_{\alpha} \tag{13}$$

$$C_i = \sum_{\alpha} n_{\alpha,\,i} C_{\alpha} \tag{14}$$

$$D_i = D \sum_{\alpha} n_{\alpha,\,i} \tag{15}$$

With

$$V_{tot,\,i} = \sum_{\alpha} n_{\alpha,\,i} m_{\alpha} \sigma_{\alpha}^3 \tag{16}$$

where $n_{\alpha,\,i}$ denotes the number of functional groups of type α in the substance i. The exponent γ and the parameter D are kept constant for all studied substances and are optimized for n-alkanes ($D = -0.01245$ and $\gamma = 0.45$) [7]. The group-contribution parameters A_{α}, B_{α}, and C_{α} of all groups α are given in [7].

4. Modeling results

The two viscosity methods, FVT and ES-LG, are tested on a database consisting of 52 hydrocarbons (21 normal alkanes, 13 branched alkanes, 4 cycloalkanes, 14 aromatics) typically present in most of the crude oils from ambient conditions to

extremely high-temperature and high-pressure (HTHP) conditions up to 573 K and 300 MPa. The temperature and pressure ranges considered in this study are given for each substance in **Table 1**. The performance of each model is assessed by the following statistical measures:

$$\text{Absolute Average Deviation (AAD)} = \frac{100}{N}\sum_{i=1}^{N}\left|\frac{\eta_{i,\ \text{cal}} - \eta_{i,\ \text{exp}}}{\eta_{i,\ \text{exp}}}\right| \tag{17}$$

$$\text{Maximum Deviation (MD)} = 100 \cdot \max\left|\frac{\eta_{i,\ \text{cal}} - \eta_{i,\ \text{exp}}}{\eta_{i,\ \text{exp}}}\right| \tag{18}$$

$$\text{Bias} = \frac{100}{N}\sum_{i=1}^{N}\frac{\eta_{i,\ \text{cal}} - \eta_{i,\ \text{exp}}}{\eta_{i,\ \text{exp}}} \tag{19}$$

where N is the total number of data points, $\eta_{i,\ \text{cal}}$ represents the calculated viscosity value, and $\eta_{i,\ \text{exp}}$ is the experimental data point obtained from the literature. The absolute average deviation AAD is a measure of how close the calculated values are to the experimental data, while the bias indicates how well the calculated values are distributed around the literature data. Low values of the bias imply that the deviations are evenly distributed about zero. A positive bias indicates overestimation of the calculated viscosity, whereas a negative value indicates

Compound	Ranges of conditions		Reference	FVT			ES-LG		
	T/K	P/MPa		AAD/%	MD/%	Bias/%	AAD/%	MD/%	Bias/%
Straight-chain alkanes (normal alkanes)									
CH_4	298–573	0.1–300	[11–13]	3	33	−2	15	47	13
C_2H_6	298–573	0.1–70	[11, 14]	2	5	1	7	35	−6
C_3H_8	298–500	0.1–100	[14, 15]	5	21	1	6	20	−2
n-C_4H_{10}	298–573	0.1–69	[11]	4	20	2	5	21	2
n-C_5H_{12}	298–573	0.1–252	[16, 17]	3	18	1	6	15	−3
n-C_6H_{14}	298–573	0.1–300	[16, 18]	4	18	−2	5	19	−1
n-C_7H_{16}	298–573	0.1–100	[16, 19]	2	6	0	4	17	4
n-C_8H_{18}	298–523	0.1–242	[18, 20, 21]	2	6	0	2	7	2
n-C_9H_{20}	298–473	0.1–300	[16, 19, 21]	2	9	0	4	10	4
n-$C_{10}H_{22}$	298–573	0.1–300	[16, 17, 21–24]	2	6	0	4	14	2
n-$C_{11}H_{24}$	303–323	0.1–62	[19]	0.1	1	0	1	4	−1
n-$C_{12}H_{26}$	298–573	0.1–300	[16, 22–27]	3	13	0	4	17	2
n-$C_{13}H_{28}$	303–353	0.1–100	[28]	1	4	1	4	8	−4
n-$C_{14}H_{30}$	313–393	0.69–60	[29]	2	8	−1	5	12	−2
n-$C_{15}H_{32}$	310–408	0.1–320	[25]	2	7	0	4	11	0
n-$C_{16}H_{34}$	298–534	0.1–273	[30, 31]	3	9	0	10	24	1
n-$C_{17}H_{36}$	323–573	0.1–0.1	[3]	2	6	−2	8	16	−8
n-$C_{18}H_{38}$	326–534	0.1–280	[25, 31]	3	12	0	9	28	8
n-$C_{19}H_{40}$	333–523		[32]	3	8	0	4	10	2
n-$C_{20}H_{42}$	326–534	1.38–243	[31, 33]	4	13	0	12	40	9

Compound	Ranges of conditions		Reference	FVT			ES-LG		
	T/K	P/MPa		AAD/%	MD/%	Bias/%	AAD/%	MD/%	Bias/%
n-$C_{32}H_{66}$	373–458	0.3–0.3	[34]	1	2	0	2	4	2
Branched alkanes									
Isobutane	300–511	0.1–55	[35, 36]	3	11	2	3	13	−1
Isopentane	303–573	0.098–196	[16, 37]	6	22	−3	11	23	−7
Neopentane	311–444	0.7–55	[38]	7	23	−3	16	60	−13
2-Methylpentane	298–550	0.1–300	[16]	1	9	0	5	16	1
3-Methylpentane	313	0.1–147	[39]	1	4	1	8	10	8
2,2-Dimethylbutane	313	0.1–147	[39]	2	8	−1	27	37	−27
2,3-Dimethylbutane	313	0.1–147	[39]	0.3	1	0	7	11	−7
3-Ethylpentane	313	0.1–147	[39]	2	3	−2	17	20	17
2,4-Dimethylpentane	313	01.147	[39]	2	6	1	23	29	23
2,2,4-Trimethylpentane	298–523	0.1–300	[20, 40–42]	2	8	0	5	13	1
2,3,4-Trimethylpentane	298–453	0.1–195	[41]	3	11	0	7	15	−7
Squalane	303–473	1–202	[43, 44]	6	33	−2	26	49	23
2,2,4,4,6,8,8-Heptamethylnonane	298–453	0.1–195	[41, 45, 46]	7	49	−6	7	51	−5
Cycloalkanes									
Cyclopentane	298–353	0.1–300	[47, 48]	5	16	−2	2	6	−1
Cyclohexane	298–393	0.1–100	[49, 50]	2	7	0	4	14	1
Methylcyclohexane	298–343	0.1–300	[51, 52]	1	6	0	4	10	−4
Ethylcyclohexane	300–530	1–50	[53]	3	12	−1	7	23	−5
Aromatics									
Benzene	298–373	0.1–300	[54]	1	3	0	5	13	−4
Toluene	298–373	0.1–299	[55]	2	6	0	3	9	2
Ethylbenzene	298–453	0.1–195	[41]	2	4	1	16	40	16
Butylbenzene	313–373	0.1–100	[56]	2	9	0	4	11	4
Hexylbenzene	313–373	0.1–100	[56]	1	3	0	5	9	5
Octylbenzene	313–373	0.1–100	[56]	1	5	0	4	9	3
1,2-Diphenylethane	353–453	0.1–195	[41]	1	2	0	12	17	−12
m-Xylene	298–473	0.1–199	[20]	2	6	0	4	10	−2
o-Xylene	298–348	0.1–110	[57]	1	3	0	25	30	−25
p-Xylene	298–348	0.1–110	[57]	2	7	−1	6	8	−6
Naphthalene	375–454	0.1–101	[58]	8	33	1	11	22	−11
1-Methylnaphthalene	298–473	0.1–200	[20]	11	35	−7	32	60	−32
Tetralin	298–448	0.1–201	[20]	5	20	−1	29	53	28
Phenanthrene	396–573	0.1–101	[58]	13	41	−6	17	29	−17
Overall AAD%				**3**			**8**		

Table 1.
Performance of FVT and ES-LG models for pure hydrocarbons over wide ranges of pressure and temperature (entries are rounded to nearest whole number).

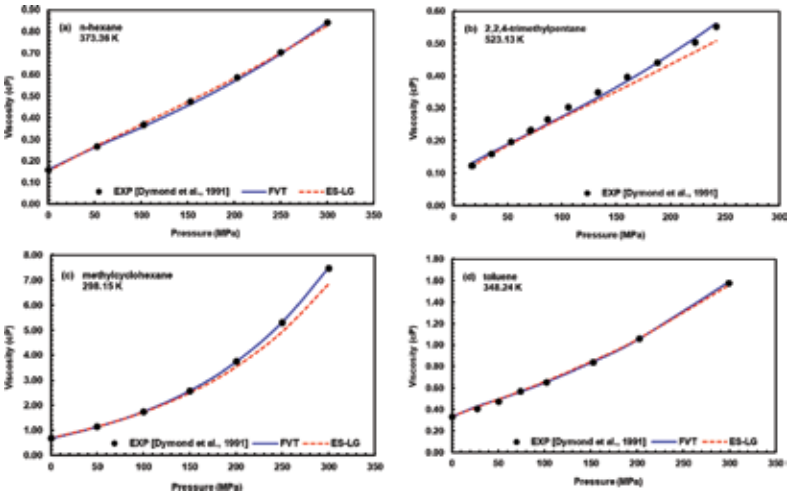

Figure 1.
Viscosity predictions obtained with FVT and ES-LG viscosity models compared with literature data (EXP) for (a) n-hexane, (b) 2,2,4-trimethylpentane, (c) methylcyclohexane, and (d) toluene.

underestimation. These statistical measures of the ability of each of the selected seven models to reproduce viscosity values at HTHP conditions for each of the 52 pure compounds are given in **Table 1**.

The overall AAD obtained with the FVT model in conjunction with the hybrid G-C PC-SAFT EoS is 3%. The three adjustable parameters (l, α, B) required in this method are obtained by fitting the FVT predictions for each pure compound to the corresponding literature data. These optimized parameters yield reliable viscosity values over the whole ranges of temperatures to 573 K and pressures to 300 MPa.

The results obtained with the entropy scaling method by Lötgering-Lin and Gross are generally in good agreement with experimental data with an overall AAD of 8%. The AADs obtained for n-alkanes, branched alkanes, cycloalkanes, and aromatics are within 1–15, 3–27, 2–7, and 3–32%, respectively. These results are impressive for a fully predictive model that requires only the input of the molecular mass and the number of functional groups in each molecule. Unfortunately, this model cannot differentiate between isomers, such as 2-methylpentane and 3-methylpentane, and xylene isomers. In addition, this model has not yet been extended to binary, ternary, and multicomponent mixtures, such as crude oils.

For comparison purposes, **Figure 1(a–d)** shows the performance of the two studied viscosity methods, FVT and ES-LG, for four pure compounds representative of straight-chain alkanes (n-hexane), branched alkanes (2,2,4-trimethylpentane), cycloalkanes (methylcyclohexane), and aromatics (toluene).

5. Conclusions

This work provides an assessment of the capabilities of two viscosity methods based on the free-volume and entropy scaling theories to model the viscosity of pure hydrocarbons over wide ranges of temperatures and pressures. The performance of the two studied viscosity models is discussed and evaluated by comparison to experimental viscosity data of 52 pure hydrocarbons from four different chemical families, namely, straight-chain alkanes, branched alkanes, cycloalkanes, and aromatics, at ambient and extremely high-temperature and high-pressure (HTHP) conditions up to 573 K and 300 MPa. The viscosity of pure components is

required in most mixture models as an input parameter, and hence accurate and reliable model for pure compounds, particularly under high-pressure conditions, is a prerequisite for the mixture viscosity to be accurately estimated using the mixture model. The predictive entropy scaling method proposed by Lötgering-Lin and Gross (ES-LG model) predicts the viscosity with an overall absolute average deviation of about 8%, and the predictions are reasonable for most engineering and industrial applications given that the accuracy of most experimental viscosity data is within 1–5%. The free-volume theory (FVT) viscosity model provides very satisfactory results with an overall AAD of 3%. However, it is important to note that unlike the entropy scaling method, the free-volume theory is not a predictive model and requires that sufficient experimental viscosity data are readily available over the temperature and pressure ranges of interest to determine the fluid specific parameters.

Acknowledgements

The Open Access Publishing fee for this chapter was fully paid by the University Library System, University of Pittsburgh, USA.

Author details

Hseen O. Baled[1,2*] and Isaac K. Gamwo[2]

1 Department of Chemical and Petroleum Engineering, University of Pittsburgh, Pittsburgh, PA, USA

2 National Energy Technology Laboratory, Research and Innovation Center, U.S. Department of Energy, Pittsburgh, PA, USA

*Address all correspondence to: hob9@pitt.edu

References

[1] Poling BE, Prausnitz JM, O'Connell JP. The Properties of Gases and Liquids. 5th ed. New York: McGraw-Hill; 2001

[2] Batschinski AJ. Untersuchungen über die innere Reibung der Fluessigkeiten. Zeitschrift für Physikalische Chemie. 1913;**84**:644-650

[3] Doolittle AK. Studies in Newtonian flow. II. The dependence of the viscosity of liquids on free-space. Journal of Applied Physics. 1951;**22**:1471-1475

[4] Allal A, Moha-Ouchane M, Boned C. A new free volume model for dynamic viscosity and density of dense fluids versus pressure and temperature. Physics and Chemistry of Liquids. 2001; **39**:1-30

[5] Allal A, Boned C, Baylaucq A. Free-volume viscosity model for fluids in the dense and gaseous states. Physical Review E. 2001;**64**:011203/1-011203/10

[6] Burgess WA, Tapriyal D, Gamwo IK, Wu Y, McHugh MA, Enick RM. New group-contribution parameters for the calculation of PC-SAFT parameters for use at pressures to 276 MPa and temperatures to 533 K. Industrial and Engineering Chemistry Research. 2014; **53**:2520-2528

[7] Lötgering-Lin O, Gross J. Group contribution method for viscosities based on entropy scaling using the perturbed-chain polar statistical associating fluid theory. Industrial and Engineering Chemistry Research. 2015; **54**:7942-7952

[8] Vijande J, Pineiro MM, Bessieres D, Saint-Guirons H, Legido JL. Description of PVT behaviour of hydrofluoroethers using the PC-SAFT EOS. Physical Chemistry Chemical Physics. 2004;**6**: 766-770

[9] Sauer E, Stavrou M, Gross J. Comparison between a homo-and a heterosegmented group contribution approach based on the perturbed-chain polar statistical associating fluid theory equation of state. Industrial and Engineering Chemistry Research. 2014; **53**:14854-14864

[10] Gross J, Sadowski G. Perturbed-chain SAFT: An equation of state based on a perturbation theory for chain molecules. Industrial and Engineering Chemistry Research. 2001;**40**: 1244-1260

[11] Younglove BA, Ely JF. Thermophysical properties of fluids. II. Methane, ethane, propane, isobutane, and normal butane. Journal of Physical and Chemical Reference Data. 1987;**16**: 577-798

[12] Evers C, Lösch H, Wagner W. An absolute viscometer-densimeter and measurements of the viscosity of nitrogen, methane, helium, neon, argon, and krypton over a wide range of density and temperature. International Journal of Thermophysics. 2002;**23**: 1411-1439

[13] van der Gulik PS, Mostert R, van den Berg HR. The viscosity of methane at 25°C up to 10 kbar. Physica A: Statistical Mechanics and its Applications. 1988;**151**:153-166

[14] Seibt D, Vo K, Herrmann S, Vogel E, Hassel E. Simultaneous viscosity-density measurements on ethane and propane over a wide range of temperature and pressure including the near-critical region. Journal of Chemical & Engineering Data. 2011;**56**:1476-1493

[15] Vogel E, Küchenmeister C, Bich E, Laesecke A. Reference correlation of the viscosity of propane. Journal of Physical

and Chemical Reference Data. 1998;**27**: 947-970

[16] Lemmon EW, McLinden MO, Friend DG. Thermophysical properties of fluid systems. In: Linstrom PJ, Mallard WG, editors. NIST Chemistry WebBook, NIST Standard Reference Database Number 69. Gaithersburg, MD: National Institute of Standards and Technology; retrieved 2018

[17] Oliveira C, Wakeham W. The viscosity of five liquid hydrocarbons at pressures up to 250 MPa. International Journal of Thermophysics. 1992;**13**: 773-790

[18] Dymond JH, Robertson J, Isdale JD. Transport properties of nonelectrolyte liquid mixtures-III. Viscosity coefficients for n-octane, n-decane, and equimolar mixtures of n-octane + n-dodecane and n-hexane + n-dodecane from 25 to 100°C at pressures up to the freezing pressure or 500 MPa. International Journal of Thermophysics. 1981;**2**:133-154

[19] Assael MJ, Papadaki M. Measurements of the viscosity of n-heptane, n-nonane, and n-undecane at pressures up to 70 MPa. International Journal of Thermophysics. 1991;**12**: 801-810

[20] Caudwell DR, Trusler JPM, Vesovic V, Wakeham WA. Viscosity and density of five hydrocarbon liquids at pressures up to 200 MPa and temperatures up to 473 K. Journal of Chemical & Engineering Data. 2009;**54**: 359-366

[21] Huber ML, Laesecke A, Xiang HW. Viscosity correlations for minor constituent fluids in natural gas: n-octane, n-nonane and n-decane. Fluid Phase Equilibria. 2005;**228-229**:401-408

[22] Knapstad B, Skolsvik PA, Oye HA. Viscosity of pure hydrocarbons. Journal of Chemical & Engineering Data. 1989; **34**:37-43

[23] Knapstad B, Skjolsvik PA, Oye HA. Viscosity of three binary hydrocarbon mixtures. Journal of Chemical & Engineering Data. 1991;**36**:84-88

[24] Dymond JH, Young KJ. Transport properties of nonelectrolyte liquid mixtures. I. Viscosity coefficients for n-alkane mixtures at saturation pressure from 283 to 378 K. International Journal of Thermophysics. 1980;**1**:331-344

[25] Hogenboom DL, Webb W, Dixon JA. Viscosity of several liquid hydrocarbons as a function of temperature, pressure, and free volume. The Journal of Chemical Physics. 1967; **46**:2586-2598

[26] Huber ML, Laesecke A, Perkins RA. Transport properties of n-dodecane. Energy & Fuels. 2004;**18**:968-975

[27] Giller EB, Drikamer HG. Viscosity of normal paraffins near the freezing point. Industrial and Engineering Chemistry. 1949;**41**:2067-2069

[28] Daugé P, Canet X, Baylaucq A, Boned C. Measurements of the density and viscosity of the tridecane + 2,2,4,4,6,8,8-heptamethylnonane mixtures in the temperature range 293.15-353.15 K at pressures up to 100 MPa. High Temperatures - High Pressures. 2001;**33**:213-230

[29] Hernández-Galván MA, García-Sánchez F, Macías-Salinas R. Liquid viscosities of benzene, n-tetradecane, and benzene + n-tetradecane from 313 to 393 K and pressures up to 60 MPa: Experiment and modeling. Fluid Phase Equilibria. 2007;**262**:51-60

[30] Dymond JH, Young KJ, Isdale JD. Transport properties of nonelectrolyte liquid mixtures-II. Viscosity coefficients for the n-hexane + n-hexadecane system at temperatures from 25 to 100°C at

pressures up to the freezing pressure or 500 MPa. International Journal of Thermophysics. 1980;**1**(4):345-373

[31] Baled HO, Xing D, Katz H, Tapriyal D, Gamwo IK, Soong Y, et al. Viscosity of n-hexadecane, n-octadecane and n-eicosane at pressures up to 243 MPa and temperatures up to 534 K. The Journal of Chemical Thermodynamics. 2014;**72**:108-116

[32] Guseinov S, Naziev Y. Izvestiya Vysshikh Uchebnykh Zavedenii, Russian (USSR). Neft i Gaz. 1974;**17**: 38-62

[33] Rodden JB, Erkey C, Akgerman A. High-temperature diffusion, viscosity, and density measurements in n-eicosane. Journal of Chemical & Engineering Data. 1988;**33**:344-347

[34] Aasen E, Rytter E, Oye HA. Viscosity of n-hydrocarbons and their mixtures. Industrial and Engineering Chemistry Research. 1990;**29**:1635-1640

[35] Diller DE, Van Poolen LJ. Measurements of the viscosities of saturated and compressed liquid normal butane and isobutane. International Journal of Thermophysics. 1985;**6**:43-62

[36] Gonzalez MH, Lee AL. Viscosity of isobutene. Journal of Chemical & Engineering Data. 1966;**11**:357-359

[37] Bridgman PW. The effect of pressure on the viscosity of forty-three pure liquids. Proceedings of the American Academy of Arts and Sciences. 1926;**61**:57-99

[38] Gonzalez MH, Lee AL. Viscosity of 2,2-dimethylpropane. Journal of Chemical & Engineering Data. 1968;**13**:66-69

[39] Kuss E, Pollmann P. Viskositäts-Druckabhängigkeit und Verzweigungsgrad flüssiger Alkane. Zeitschrift für Physikalische Chemie. 1969;**68**:205-227

[40] Dymond JH, Glen NF, Isdale JD. Transport properties of nonelectrolyte liquid mixtures-VII. Viscosity coefficients for isooctane and for equimolar mixtures of isooctane + n-octane and isooctane + n-dodecane from 25 to 100°C at pressures up to 500 MPa or to the freezing pressure. International Journal of Thermophysics. 1985;**6**: 233-250

[41] Krahn UG, Luft G. Viscosity of several liquid hydrocarbons in the temperature range 298-453 K at pressures up to 200 MPa. Journal of Chemical & Engineering Data. 1994;**39**: 670-672

[42] Pádua AAH, Fareleira JMNA, Calado JCG, Wakeham WA. Density and viscosity measurements of 2,2,4-trimethylpentane (isooctane) from 198 K to 348 K and up to 100 MPa. Journal of Chemical & Engineering Data. 1996; **41**:1488-1494

[43] Schmidt KAG, Pagnutti D, Curran MD, Singh A, Trusler JPM, Maitland GC, et al. New experimental data and reference models for the viscosity and density of squalane. Journal of Chemical & Engineering Data. 2015;**60**:137-150

[44] Ciotta F, Maitland G, Smietana M, Trusler JPM, Vesovic V. Viscosity and density of carbon dioxide + 2,6,10,15,19,23-hexamethyltetracosane (squalane). Journal of Chemical & Engineering Data. 2009;**54**:2436-2443

[45] Canet X, Daugé P, Baylaucq A, Boned C, Zéberg-Mikkelsen C, Quiñones-Cisneros SE, et al. Density and viscosity of the 1-methylnaphthalene + 2,2,4,4,6,8,8-heptamethylnonane system from 293.15 to 353.15 K at pressures up to 100 MPa. International Journal of Thermophysics. 2001;**22**:1669-1689

[46] Et-Tahir A, Boned C, Lagourette B, Xans P. Determination of the viscosity of various hydrocarbons and mixtures

of hydrocarbons versus temperature and pressure. International Journal of Thermophysics. 1995;**16**:1309-1334

[47] Harris KR, Newitt PJ, Woolf LA. Temperature and density dependence of the viscosity of cyclopentane. Journal of Chemical & Engineering Data. 2004;**49**: 138-142

[48] Kurihara K, Kandil ME, Marsh KN, Goodwin ARH. Measurement of the viscosity of liquid cyclopentane obtained with a vibrating wire viscometer at temperatures between (273 and 353) K and pressures below 45 MPa. Journal of Chemical & Engineering Data. 2007;**52**:803-807

[49] Hernández-Galván MA, García-Sánchez F, García-Flores BE, Castro-Arellano J. Liquid viscosities of cyclohexane, cyclohexane + tetradecane, and cyclohexane + benzene from (313 to 393) K and pressures up to 60 MPa. Journal of Chemical & Engineering Data. 2009;**54**:2831-2838

[50] Tanaka Y, Hosokawa H, Kubota H, Makita T. Viscosity and density of binary mixtures of cyclohexane with n-octane, n-dodecane, and n-hexadecane under high pressures. International Journal of Thermophysics. 1991;**12**: 245-264

[51] Jonas J, Hasha D, Huang SG. Self-diffusion and viscosity of methylcyclohexane in the dense liquid region. The Journal of Chemical Physics. 1979;**71**:3996-4000

[52] Baylaucq A, Boned C, Dauge P, Lagourette B. Measurements of the viscosity and density of three hydrocarbons and the three associated binary mixtures versus pressure and temperature. International Journal of Thermophysics. 1997;**18**:3-23

[53] Stephan K, Lucas K. Viscosity of Dense Fluids. 1st ed. New York: Plenum Press; 1979

[54] Dymond JH, Robertson J, Isdale JD. Transport properties of nonelectrolyte liquid mixtures - IV. Viscosity coefficients for benzene, perdeuterobenzene, hexafluorobenzene, and an equimolar mixture of benzene + hexafluorobenzene from 25 to 100°C at pressures up to the freezing pressure. International Journal of Thermophysics. 1981;**2**:223-236

[55] Dymond JH, Awan MA, Glen NF, Isdale JD. Transport properties of nonelectrolyte liquid mixtures. VIII. Viscosity coefficients for toluene and for three mixtures of toluene + hexane from 25 to 100°C at pressures up to 500 MPa. International Journal of Thermophysics. 1991;**12**:275-287

[56] Ducoulombier D, Zhou H, Boned C, Peyrelasse J, Saint-Guirons H, Xans P. Pressure (1-1000 bars) and temperature (20-100°C) dependence of the viscosity of liquid hydrocarbons. The Journal of Physical Chemistry. 1986;**90**:1692-1700

[57] Kashiwagi H, Makita T. Viscosity of twelve hydrocarbon liquids in the temperature range 298-348 K at pressures up to 110 MPa. International Journal of Thermophysics. 1982;**3**: 289-305

[58] Roetling JA, Gebhardt JJ, Rouse FG. Effect of pressure on viscosity of naphthalene, phenanthrene and impregnation pitches. Carbon. 1987;**25**: 233-242

Chapter 3

The Fast Silver Ion Conducting Solid-State Electrolytes for Deriving Thermodynamic Data

Fiseha Tesfaye, Mykola Moroz, Oleksandr Reshetnyak, Daniel Lindberg, Pekka Taskinen and Leena Hupa

Abstract

The electromotive force (EMF) method was described and some characteristic examples from the past and recent literatures were reviewed. The important experimental procedures for a successful measurement of an EMF of different galvanic cells at a certain temperature and determination of the thermodynamic properties of chemical compounds from the obtained EMF values were described. A typical galvanic cell arrangement in a furnace was presented. The two most common types of AgI-based solid electrolytes, AgI and $RbAg_4I_5$, were discussed in detail. The ionic conduction mechanisms and the application of the solid electrolytes in the EMF cells were described. In this work, we have also conducted EMF measurements using the fast Ag^+ ion conducting solid-state electrolyte. The solid-state electrolyte Ag_3GeS_3I glass and the cathode material $Ag_4HgSe_2I_2$ were synthesized and electrochemical cell (−)graphite|Ag|Ag_3GeS_3I glass|$Ag_4HgSe_2I_2$|graphite(+) was assembled to measure the activity of Ag in the quaternary phase. The extremely low values of activity of silver in $Ag_4HgSe_2I_2$ in the temperature range 412–482 K indicate that $Ag_4HgSe_2I_2$ has superionic property. The obtained results and the determined thermodynamic values are presented and discussed.

Keywords: EMF method, solid electrolyte, silver iodide, thermal stability, Gibbs free energy

1. Introduction

Thermochemical data of chemical compounds is of great importance in the modeling of high temperature materials processing and their applications. Accurate thermodynamic data are important for meaningful modeling of phase equilibria and thermodynamics of multiphase material systems. These accurately determined thermodynamic properties and their chemical behaviors under different conditions promote improved extractive metallurgy of valuable metals and the design of novel multi-component functional materials.

Calorimetry, vapor pressure measurements and EMF methods are the main experimental techniques to investigate thermodynamic properties of phases and phase assemblages. Extensive reviews on these methods have been published in the past. For the determination of enthalpy, precisely, calorimetry is a well proven.

In the vapor pressure methods, partial pressures of individual components can be measured and the thermodynamic activities and partial Gibbs energies can be derived from them. When partial pressures can also be measured as a function of temperature, the partial enthalpies and entropies can be derived, although these derived quantities are usually less accurate than the directly measured partial Gibbs energies. Introduced by Kiukkola and Wagner [1] for solid-state thermodynamic investigations, the EMF method has proven to be direct, effective, and the most accurate method for determining the Gibbs free energies of formation, chemical potentials, thermodynamic activities and partial pressures in equilibrium conditions. Furthermore, the entropies and enthalpies of chemical reactions can be derived from the measured temperature versus EMF relations of the cell [2].

This paper reviews, updates and discusses the EMF method that applies the fast Ag^+ ion conducting solid electrolytes. Furthermore, we have also conducted EMF measurements using the fast Ag^+ ion conducting solid-state electrolyte. The solid electrolyte Ag_3GeS_3I glass and the cathode material $Ag_4HgSe_2I_2$ were synthesized and electrochemical cell was assembled to measure the activity of Ag in the quaternary phase $Ag_4HgSe_2I_2$. The obtained results and the determined thermodynamic values are presented in the subsequent sections.

1.1 Principles of the EMF method

In a galvanic cell for thermodynamic studies there is generally one electrode at which electrons would be consumed (the cathode) and one electrode at which electrons are produced (the anode) as the cell reaction proceeds. If the electrolyte system conducts electricity by the migration of ions only, then the electrons must move from cathode to anode via an external electronic conductor, which is usually Pt or Au or pure graphite lead. It is along this conductor that the electric potential which is generated by the cell reaction can be measured. Any meaningful thermodynamic investigation requires that the cell function in a complete reversible manner, i.e., no external current is flowing. This is usually assured by the use of high-resistance (above 10^{10} Ω) measuring devices, resulting in the measurement of an "open circuit" potential [3, 4].

In most practical high temperature systems, electrolytes usually have a small component of non-electrolytic conduction, which make the open circuit unattainable. In this case, in addition to ionic, electronic conduction will also takes place, because electrons can migrate through the electrolyte and permit the cell reaction to proceed at speed which is not determined by the resistance of the external electronic conductor. A real electrochemical system therefore has a potential which is given by Eq. (1) [4]:

$$E = \frac{RT}{zF} \int_{a_i'}^{a_i''} t_i \cdot dlna_i \tag{1}$$

where t_i is the transfer number of the ionic species, which is conducted through the electrolyte having the thermodynamic activity a_i' at one electrode and a_i'' at the other. When the electrolyte conducts significantly by electron migration, then the cell reaction can proceed spontaneously and one electrode is depleted of atoms while the other receives atoms.

It follows that the electrodes can only be maintained at a constant chemical potential of all components providing that equilibrium can be established more rapidly than the rate of arrival or loss of material at the electrode-electrolyte interface. Consider a cell which has two metal-metal oxide electrodes with a leaky

electrolyte. The electrode with the higher oxygen dissociation pressure can lose oxygen through the electrolyte by the arrival of electrons through the electrolyte to form oxygen ions, and hence the oxide is reduced at this electrode. At the other electrode, oxygen ions absorbed and the electrode is oxidized continuously. Providing the electrode reactions can accommodate this corrosion reaction as a result of metal-oxygen reactions at the electrodes which restore the original mixture at the electrode-electrolyte interface, and then the cell can be used for thermodynamic studies. Failing to do so, the EMF of the cell will drift continuously and results are difficult to interpret. At the higher temperatures, solid electrolyte systems can be permeable to gases, and interaction between electrodes and their surrounding gaseous atmospheres can also play an important role in making experiments difficult.

The porosity of a solid electrolyte depends very much upon the manufacturing method as well as on the temperature of the cell operation, and therefore no general description can be given of the conditions under which this effect could become significant. The effects of atmospheric reactions with electrode systems can be minimized, or eliminated to all practical extents, by providing samples of the electrode to the gas phase for pre-equilibration of the gas approaching the cell electrode and by separating the atmospheres surrounding the electrodes from one another.

The corresponding phenomena in molten salt electrolytes which can lead to drifting EMFs are reactions which result from the solubility of metals in the molten electrolyte, which confer electron conducting properties on the electrolyte, or the possibility of cations of more than one valency for a given cation in the melt. Both mechanisms can lead to the transport number of the ions less than unity and to oxidation/reduction reactions at the electrode [4].

1.2 The EMF method with solid-state electrolytes

Electrochemical cells with solid-state electrolytes for thermodynamic studies typically consist of a solid electrolyte between the reference and the cathode electrodes [2]. These electrodes are connected to wires, which are usually Pt or Au, for measuring the EMF of the cell. In thermodynamic measurements, the EMF must be measured under open circuit conditions. This is usually assured by the use of high impedance ($R > 10^{10}\ \Omega$) measuring devices, which enable measurement of an "open circuit" EMF [3, 5]. Utilization of the EMF technique for thermodynamic investigation of metallic systems, and its basic principles and the main requirements has been recently discussed in detail by a few researchers [2, 3, 5–9].

The EMF technique is a direct method that enables one to determine the Gibbs energies of formation, chemical potentials, thermodynamic activities or partial pressures precisely [10, 11]. Furthermore, the entropies and enthalpies of reactions can be calculated from the temperature dependence of EMF of the cell. Electrochemical cells with solid electrolytes consist in most cases of a solid electrolyte between two electrodes [11]. A typical galvanic cell arrangement for thermodynamic measurements is shown in **Figures 1** and **2**.

The alumina sheaths indicated in **Figure 2** should press the cell from both directions to insure good contact at the interfaces. Flow of the protective gas (Ar) must always be away from the reference electrode. The design of the galvanic cell should be such that the reaction of interest harnesses the cell reaction and the Gibbs energy for the reaction could be calculated from the EMF of the galvanic cell. One of the criteria for the application of this method is that the electrolyte is a pure ionic conductor under the very experimental conditions.

For instance, in experimental investigation of Ag-based compounds below 713 K, solid-electrolytes $RbAg_4I_5$ and AgI are the two widely known and used

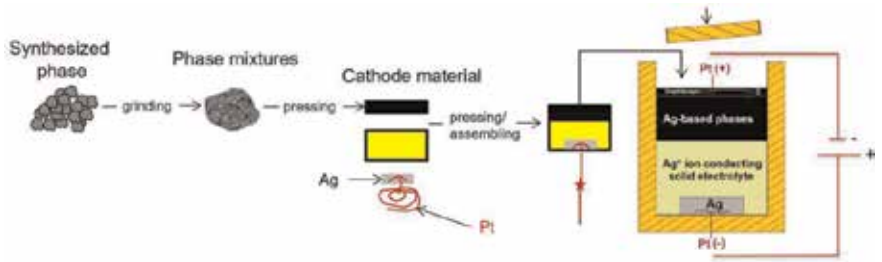

Figure 1.
Illustration showing preparation of galvanic cells for the solid-state EMF experiments.

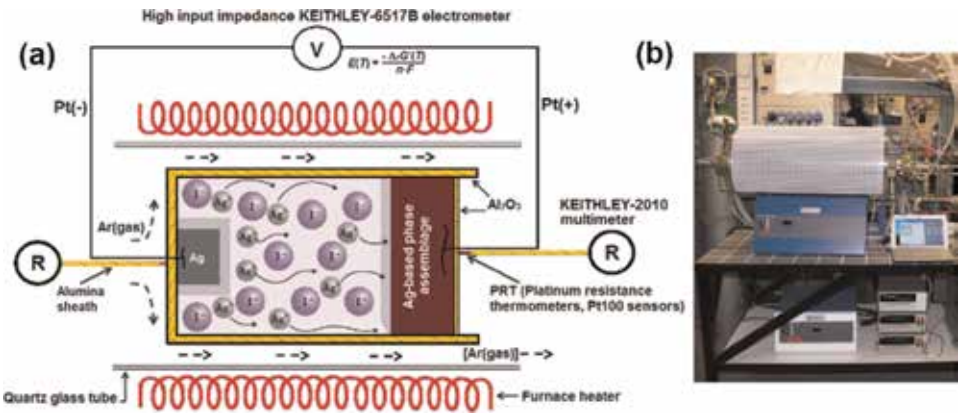

Figure 2.
(a) Schematic diagram of the experimental setup for an EMF-measurements in a horizontal tube furnace; [12]. (b) A picture of a high-temperature electrochemical stations for thermodynamic measurements in the laboratory.

superionic conductors of silver ion. For example, to determine the Gibbs energies of formation of the compound Ag_5Te_3 at different temperature conditions galvanic cells are constructed as cells in Eqs. (2) and (3):

$$Ag|RbAg_4I_5|Ag_5Te_3, Te \quad 300 < T/K < 505 \tag{2}$$

$$Ag|AgI|Ag_5Te_3, Te \quad 420 < T/K < 713 \tag{3}$$

Current flows from the right to the left. Temperature ranges for accurate measurements are those in which the electrolytes are superionic conductors. At equilibrium conditions, the virtual cell reaction in both cells is expressed as Eq (4):

$$5Ag + 3Te = Ag_5Te_3 \tag{4}$$

Based on the EMF of the galvanic cells, at certain temperatures, it is possible to determine the thermodynamic properties by using the basic thermodynamic equations at constant pressure.

2. Experimental requirements

In EMF measurements for the determination of thermodynamic properties, it is important to ascertain the conditions under which the electrolyte shows the best

T (K)	E (mV)	T (K)	E (mV)
412.87	91.37	450.12	109.26
415.36	92.65	452.59	111.16
417.85	93.92	455.07	112.81
420.34	95.41	457.54	113.85
422.84	96.26	460.21	114.85
425.31	97.97	462.58	115.91
427.80	98.71	465.26	117.04
430.28	100.51	468.12	118.04
432.77	100.95	470.34	119.37
435.25	102.41	472.54	120.86
437.73	103.75	475.22	121.71
440.21	105.14	477.62	122.78
442.69	106.4	479.75	124.80
445.17	107.23	482.21	125.58
447.64	108.61	—	—

Table 1.
A summary of experimental values of EMF vs. T obtained in the electrochemical cell in Eq. (17).

performance. The main problems for successful electrochemical cell operation are selection of a suitable electrolyte and the exact identification of the single reversible process occurring at each electrode. The corresponding electrolyte should provide purely ionic conductivity in the temperature range where it is used, i.e., one single ion should be responsible for establishing the potential. A well-defined reversible reaction is required to establish the potential. Practically, there are many additional requirements [3, 5]:

- the equilibrium potential at a given temperature should be established within a reasonable time,
- after temperature changes, the same equilibrium potential has to be established regardless of whether the temperature has been increased or lowered, and
- following polarization of the cell by a potential imposed from outside, again the same equilibrium potential has to be established.

In addition, there are a number of purely experimental requirements that have to be considered, especially in measurements at high temperatures [5, 9]:

- any reaction between electrodes and electrolyte or between electrodes and lead wires must be negligible,
- if lead wires of different materials are used it is necessary to consider the corresponding thermal-EMF,
- any temperature gradient in the cell should be avoided;
- reactions between crucible materials and electrodes or electrolyte should be excluded,

- concentration changes due to the vapor pressure of the electrodes must be taken into consideration,
- any direct exchange of matter between the two electrodes (e.g., via the gas phase) has to be excluded, and
- any electrical interference between the furnace in which the cell is heated and the cell itself should be avoided, either by a proper winding of the furnace or by appropriate grounding.

Thermal-EMF and temperature gradients can be minimized by using similar lead material at both electrodes and by placing the cell within the constant heating zone of the experimental assembly, respectively [9]. Proper design of the galvanic cells and their flexibility in the furnace while measurements are conducted will also help to minimize temperature differences at both ends of the electrodes, as described in [12]. In this work, all these experimental requirements were fulfilled.

2.1 Ag^+ ion conducting solid electrolytes

Solid electrolytes are solid phases, which transfer electric charge by moving ions only. Good ionic conductivity requires a large amount of movable ions and a lot more free sites in the lattice than movable ions, so that the jump probability is as high as possible. The solid electrolytes can be oxides, halides, iodides, sulfides and other types of solid materials. For example, in the AgI-based electrolytes electrical current is carried by Ag^+ ions.

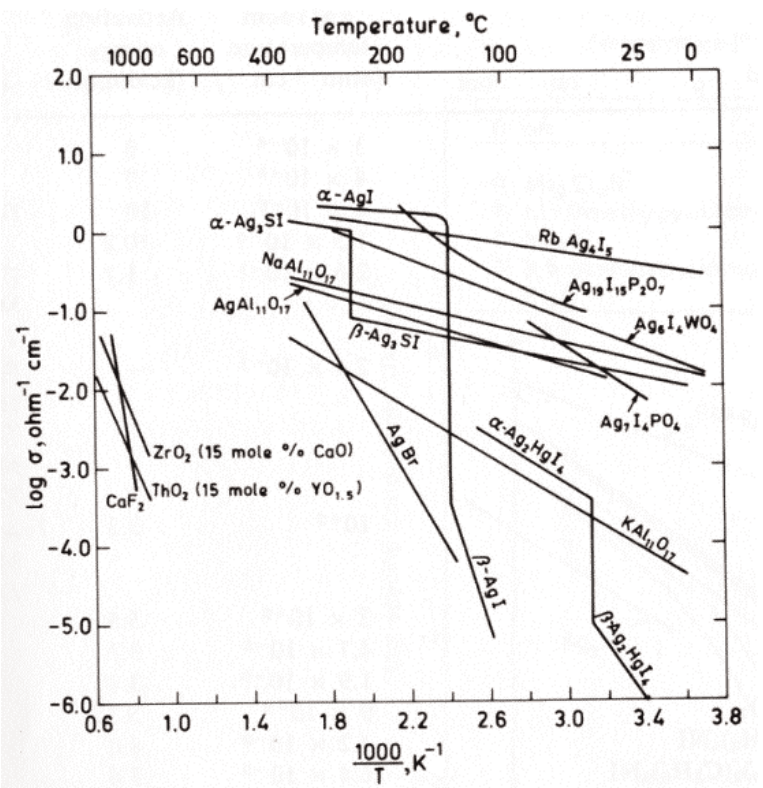

Figure 3.
The ionic conductivity of some solid electrolytes as a function of temperature [2].

Recently, the importance of solid electrolytes has increased remarkably due to their role in various applications. They are commonly used in electrochemical cells to measure chemical potentials of gases, liquids and solids. Detailed theory and practical applications of the solid electrolytes have been discussed in many review papers [3, 6, 13–22]. **Figure 3** shows ionic conductivity of some of the solid electrolytes in different temperature regions.

One of the most important criteria for a solid electrolyte to be used in EMF cells for thermodynamic studies is that it should be a purely ionic conductor, or at least has only a negligible contribution of electronic conduction. Thus, if electric current is carried solely by moving ions, the ion transference number t, in Eq. (5), should be >0.99 at a given experimental conditions [3, 4].

$$t = \frac{\sigma(ion)}{\sigma(ion) + \sigma(electronic)} \tag{5}$$

where σ(ion) is ionic conductivity and σ(electronic) is electronic conductivity.

In any case where $t < 0.99$, an accurate knowledge of the conductivity of the solid electrolyte becomes important [3]. When solid electrolytes are used for EMF measurements, one additional experimental requirement has to be fulfilled: a good and reliable contact between electrodes and electrolyte in order to obtain stable and reversible EMF values. In the thermodynamic studies of silver-based alloys and compounds, $RbAg_4I_5$ and AgI are two widely used fast ionic conductors of Ag^+ ions. These electrolytes were also used in our study by the EMF method. Properties of the solid electrolytes and their usage limits in the EMF method are reviewed in Section 2.2.1.

2.1.1 Properties of AgI and $RbAg_4I_5$

Crystalline forms γ-, β- and α-AgI are stable at ambient pressure conditions. The β-AgI → α-AgI phase transition takes place at 420 K, accompanied with a significant increase in ionic conductivity [10, 23–25]. At the phase transition temperature, the ionic conductivity of α-AgI is 1.31 S cm^{-1} [26]. As shown in **Figure 4**, the superionic compound $RbAg_4I_5$ is thermodynamically stable within the temperature range

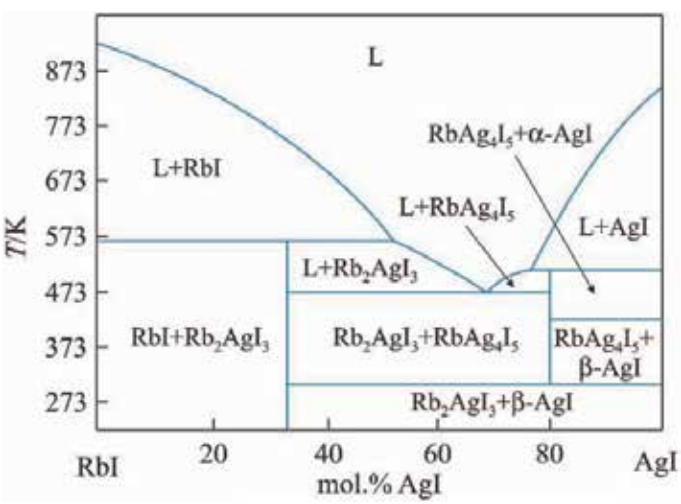

Figure 4.
The phase diagram of RbI–AgI system [27].

300–505 K and in the AgI rich region coexists with the β- and α-AgI phases [27]. At about 300 K, $RbAg_4I_5$ shows a high ionic conductivity of ~0.21 S cm^{-1} [28]. Therefore, $RbAg_4I_5$ can be used as an electrolyte even close to room temperature (>300 K) [24, 29]. Ag^+ is the moving ion in both AgI-based solid electrolytes. In general, the AgI-based electrolytes possess a large amount of free sites for the Ag^+ ions to move.

Ionic conductivity in solid electrolytes is usually due to lattice defects, and in AgI-based electrolytes these defects are caused by large cation disorders [3, 25]. Chemical diffusion occurs in the presence of concentration or chemical potential gradient and it results in net transport of mass. For example, when local differences in stoichiometry equilibrate, metal or non-metal ions and electrons diffuse simultaneously. These phenomena are described by the chemical diffusion coefficient D [2]. At low-temperatures, the ionic conductivity generally follows the Arrhenius-type temperature dependence [24, 25, 30].

AgI-based electrolytes possess a large amount of free sites for the Ag^+ ions to move. Due to the presence of these excess sites for Ag^+ ions [31] and quasi-molten state of Ag^+ ions in the structure [24], as well as the presence of passageways for Ag^+ ions which are formed by the face-sharing tetrahedral [32]; α-AgI is a fast ionic conductor of Ag^+ ions. In α-$RbAg_4I_5$, iodide ions are arranged in a similar structure as manganese atoms are in β-Mn, so that one unit cell, which includes $RbAg_4I_5$, contains 56 tetrahedral sites, such that Ag^+ ions can move freely in the lattice. The large Rb^+ ions are surrounded by highly distorted iodide octahedral and are not mobile [26, 28]. Therefore, the structure of superionic compounds can be treated as two-component system where exist the highly mobile ions like molten sublattice and another type of ions in fixed positions that formed a framework and determined the mechanical properties of the sample.

The ion transference number of α-AgI in the temperature range 420–713 K is 1 ± 0.01 [33]. Below its melting temperature, at T_m = 505 K, α-$RbAg_4I_5$ is a high ionic conductor of Ag^+ ions with negligible electronic conduction [24, 35].

Based on various conductivity data and/or EMF data, Patterson [34] has shown that in the electrolytic conduction domain of AgI, the chemical potential of silver in AgI changes only slightly. Using the compiled thermodynamic data of Barin [36], we calculated activities of silver (a_{Ag}) in AgI at $P_{I_2(g)} = 1$ atm (for the dissociation reaction $2AgI \rightleftarrows 2Ag + I_2(g)$), as a function of temperature. According to results from our analysis, the a_{Ag} in AgI varied between $2.5 \cdot 10^{-9}$ at 420 K, $1.2 \cdot 10^{-7}$ at 500 K and $3.6 \cdot 10^{-5}$ at 700 K. Thus, the chemical potential of silver in AgI does not change significantly, in its ionic conduction domain. Therefore, the solid electrolytes AgI and $RbAg_4I_5$ can be safely used in their respective pure ionic conduction domains (420–713 and 298–505 K, respectively) for EMF cells in the experimental thermodynamic studies of silver-based phases. The super ionic conducting temperature range of α-AgI (420–713 K) may be increased by adding PbI_2, in the lower temperature region.

AgI is a photosensitive material. According to the calculated curves shown in **Figure 7**, which was calculated by the HSC chemistry software [37] below 773 K, AgI reaction with H_2O, $O_2(g)$, $H_2(g)$ and $S_2(g)$ is not spontaneous. However, its relative sensitiveness to the $H_2(g)$ is clear.

In $RbAg_4I_5$ iodide ions are arranged in very same way as in manganese atoms are in β-manganese, so that one unit cell, which includes four $RbAg_4I_5$, contains 56 tetrahedra sites, so that Ag^+ ions can move freely in the lattice. The $RbAg_4I_5$ electrolyte has a wider temperature stability range and do not be affected by moisture [11]. The ionic conductivity of $RbAg_4I_5$ is illustrated in **Figure 3**.

The thermodynamic stability of $RbAg_4I_5$ is an important property that must be considered in any long term application. $RbAg_4I_5$ is unstable at temperatures below 300 K where it decomposes into AgI + Rb_2AgI_3, as shown in **Figure 4**.

Therefore the conducting phase would be nonexistent at low temperature. However, it was found that this reaction requires a catalyst such as H_2O vapor in order to initiate. By handling the materials in a dry atmosphere and hermetically sealing the batteries, the conducting phase has been maintained in devices for 5 years at temperatures below 300 K.

The synthesis of $RbAg_4I_5$ is straightforward. One method involves intimately mixing stoichiometric amounts of RbI and AgI, adding sufficient H_2O to form a thick fluid paste, and then removing the H_2O by air drying at slowly increasing temperatures, finally drying and combining the remaining reactant phases at a temperature between 483 and 502 K that is between the eutectic and the incongruent melting point [38]. By performing this reaction process over a 2 day period, single phases $RbAg_4I_5$ is formed. The materials is then powdered and stored in a vacuum oven at 343 K to prevent any environmental degradation [39].

2.1.2 Properties of superionic Ag-based glassy electrolytes

Another class of superionic materials is superionic glassy electrolytes (SGE). Inorganic SGE have a number of advantages compared to crystal compounds. Some advantages include easier regimes of synthesis, absence of grain boundaries, isotopic properties, single ion conductivity, etc. [40, 41]. In the vicinity of the glass transition temperature (T_g) the glassy material becomes very soft. It is mean a good contact between the electrolyte and electrodes. In contrast to the crystal compounds such as AgI and $RbAg_4I_5$ some glassy materials have the high values of ionic conductivity at room temperature [42]. The high ionic conductivity in SGE can be explained by the presence of open free space in the glass structure [42]. Moreover, using the glass matrix we can fixed the high ionic conductivity modification of superionic phase in the temperature range where it is metastable [43]. For example, at crystallization of AgI-Ag_2O-M_xO_y (M = B, Ge, P, Mo) glasses that include the high concentration of silver iodide, the α-AgI phase was successfully stabilized in a glass matrix. As a result, the value of ionic conductivity for this material at room temperature is found $\sigma = 10^{-1}$ S cm^{-1} [43, 44].

The glass formation regions in the GeS_2-Ag_2S and GeS_2-Ag_2S-AgI systems were investigated in [45]. It was found that glasses from these regions are purely ionic (Ag^+) conductors. The influence of the silver iodide addition on conductivity of different sulfide based glasses has been established. The maximum value of conductivity and minimum value of activation energy for the sample with highest content of AgI (52.3 mol%) is found to be $\sigma \sim 10^{-2}$ S cm^{-1} and E_a = 0.25 eV, respectively at room temperature. The mechanism of the Ag^+ diffusion in AgI based superionic glasses has been investigated by using NMR method [46]. The NMR time scale shows that all Ag^+ ions are moving by hopping from one iodine ion to the other.

Moroz et al. [47] investigated the glass forming region in the Ag_2GeS_3-AgBr system. The formation of the Ag_3GeS_3Br glassy phase has been established for the first time. Based on results of electrical conductivity measurements it was established that Ag_3GeS_3Br glass is purely ionic conductor and belong to class of superionic materials. The model of the drift motion of ions has been proposed. According to [48], the glass forming region in the Ag_3GeS_3Br-AgBr system is found to be 0–52 mol% GeS_2. In this system the new quaternary phase $Ag_3Ge_2S_5Br$ (space group $P2_13$, a = 1.016702(7) nm, Z = 4 [49]) has been synthesized for the first time.

It can be obtained in both crystalline and glassy state. Electronic structure calculations support the experimental results. The electrical conductivity measurements of glassy and crystalline samples were performed by direct current probe method using different constructions electrochemical cells. It was found that the glassy materials are purely ionic conductors [48, 49].

The purely ionic conductivity in the wide temperature range and simple method of obtaining glassy materials make them interesting for different applications. For example, Ag_2GeS_3, Ag_3GeS_3Br, and Ag_3GeS_3I glassy materials were used as ion selective membranes in electrochemical cells to calculate the thermodynamic functions of some superionic compounds [50–53].

2.2 Thermodynamics of electrochemical cells

For an electrochemical cell with a solid-electrolyte and elements M and Z:

$$\mathrm{M\ (solid, Liq)|electrolyte\ (M^{+n}\ or\ M^{-n})|\ M_xZ_{1-x}(solid, Liq) - Z}, \tag{6}$$

at equilibrium, the incorporation of M^{+n} or M^{-n} at the interface into the cathode (M_xZ_{1-x}(solid, Liq)-Z) or the overall electrochemical reaction of the electrochemical cell can be expressed by a virtual electrochemical cell reaction Eq. (7).

$$\mathrm{M^{+n}\ or\ M^{-n} + Z = M_xZ_{1-x}}. \tag{7}$$

The amount of work, other than the work for volume expansion, which is necessary for the transfer of 1 mole of element M in a valence state n from its pure state into a M-Z-compound, is related to the transfer of a charge $n \bullet F$ by;

$$\mu_M(\mathrm{M - Z - compound(s)}) - \mu_M^{\circ}(\mathrm{M}) = -n \cdot F \cdot E_{\mathrm{EMF}}, \tag{8}$$

or

$$\Delta_r G^{\circ} = -n \cdot F \cdot E_{\mathrm{EMF}} \tag{9}$$

where μ_A is the chemical potential of substance M in the M-N-compound(s) and μ_M° is the standard chemical potential of substance M in pure substance M, which is 1. $\Delta_r G^{\circ}$ is the change in the Gibbs energy of the reaction, E is the electromotive force produced by the cell in volts, F is the Faraday constant, 96485.332896 C mol^{-1} [54] and n is the number of electrons involved in the virtual electrochemical cell reaction.

The Gibbs energies of our isobaric equilibrium reactions were calculated directly from the measured E_{EMF} vs. T relations, by using the basic thermodynamic Eq. (9) of an electrochemical cell. In a similar way, the entropies, enthalpies and heat capacities of the studied virtual reactions were calculated using Eqs. (10)–(12).

$$\Delta_r S^{\circ} = -n \cdot F \cdot \left(\frac{\partial E_{\mathrm{EMF}}}{\partial T}\right), \tag{10}$$

$$\Delta_r H^{\circ} = -n \cdot F \cdot \left[E_{\mathrm{EMF}} - \left(\frac{\partial E_{\mathrm{EMF}}}{\partial T}\right) \cdot T\right], \tag{11}$$

$$\Delta_r C_P = -n \cdot F \cdot \left(\frac{\partial^2 E_{\mathrm{EMF}}}{\partial^2 T}\right) \cdot T \tag{12}$$

2.2.1 Gibbs energy of formation

By definition, the reaction of formation of a species A can be written as:

$$\mathrm{mM} + \mathrm{nN} + \ldots \rightleftarrows \mathrm{aA} \tag{13}$$

where a, n, m etc. are stoichiometric coefficients, and the standard Gibbs energy of formation is:

$$\Delta_f G^{\circ} = G^{\circ}_{\text{products}} - G^{\circ}_{\text{reactants}} = aG^{\circ}_{\mathrm{A}} - mG^{\circ}_{\mathrm{M}} - bG^{\circ}_{\mathrm{N}} - \tag{14}$$

The standard Gibbs energies of formation of the studied multicomponent phases were calculated by combining the Gibbs energies of the virtual electrochemical cell reactions (calculated according to Eq. (9)) and the standard Gibbs energies of the pure components, for which literature data are available. The standard entropies of pure compounds have been calculated by:

$$S^{\circ}_{\mathrm{A}} = \Delta_{\mathrm{f}} S^{\circ}_{\mathrm{A}} + S^{\circ}_{\mathrm{M}} + S^{\circ}_{\mathrm{N}} + \ldots \tag{15}$$

Gibbs energy of phase transition at the transformation temperature T_{tr} can be expressed by:

$$\Delta_{\mathrm{tr}} G^{\circ} = \Delta_{\mathrm{tr}} H^{\circ} - \left(\frac{\Delta_{\mathrm{tr}} H^{\circ}}{T_{\mathrm{tr}}} \right) \cdot T. \tag{16}$$

The high or low temperature experimental points can be extrapolated to low or high temperatures, respectively, by using the Gibbs energies of phase transitions expressed by Eq. (16). Two types of electrolyte are used in thermodynamic measurements: liquid electrolytes and solid electrolytes, each with characteristic advantages and disadvantages. In the following chapter, experimental study with the solid-state electrolyte is presented.

3. Experimental section

The phases were synthesized from the pure elements Ag (99.999 wt%), Hg (99.99 wt%), Se (99.999 wt%), and I_2 (99.999 wt%). The synthesis and annealing were performed in an evacuated quartz glass ampoules with a total residual pressure of <1 Pa. Ag_2Se and HgI_2 compounds were obtained by cooling the melt mixtures of the corresponding elements, at the rate of 2 K min^{-1}, to room temperature. The $Ag_4HgSe_2I_2$ compound was obtained by cooling the melted mixture of Ag_2Se and HgI_2 in the molar ratio 2:1 to room temperature. The thermodynamic equilibrium of $Ag_4HgSe_2I_2$ crystals powdered to particle size ≤5 μm was achieved by two-stage annealing at 510 and 400 K for 500 h. The synthesized material was analyzed by the SEM-EDS technique. The SEM-EDS analyses confirmed the existence of a homogenous quaternary phase with a composition of $Ag_4HgSe_2I_2$. Results of the SEM-EDS analysis are presented in **Figure 5**.

The potential-forming processes were performed by cell in Eq. (17):

$$(-)\ \text{graphite}|\mathrm{Ag}|\mathrm{Ag_3GeS_3I}\ \text{glass}|\mathrm{Ag_4HgSe_2I_2}|\text{graphite}\ (+), \tag{17}$$

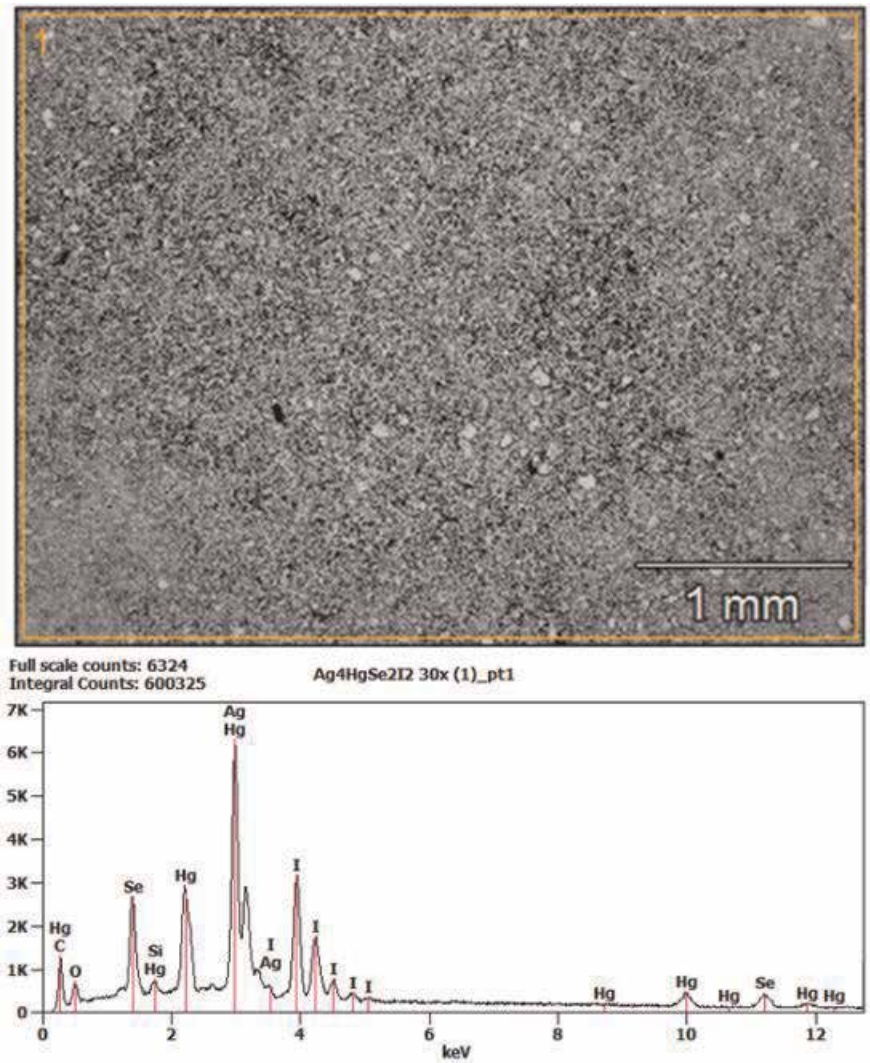

Figure 5.
The SEM-EDS analysis of the synthesized phase $Ag_4HgSe_2I_2$. Traces of Si and O peaks are as a result of the quartz glass SiO_2 ampoule particles after depressurization and crushing operation to remove the synthesized sample.

where Ag_3GeS_3I glass is the solid electrolyte with fast Ag^+ ion conductivity [45], $Ag_4HgSe_2I_2$ is the cathode material. Ag_3GeS_3I glass, as well as Ag_3GeS_3Br [48], belongs to the category of superionic materials [55]. The linear dependencies of the EMF of the electrochemical cell on temperature were used to determine the standard thermodynamic properties of $Ag_4HgSe_2I_2$.

Components of the electrochemical cells in powder form were pressed at 10^8 Pa through a 2 mm diameter hole arranged in the fluoroplast matrix up to density $\rho = (0.93 \pm 0.02)\cdot\rho_0$, where ρ_0 is the experimentally determined density of cast alloys. To eliminate possible defects of plastic deformation during the pressing of alloys, we performed five-fold thermal cycling of electrochemical cells in the range of 400–470 K, with heating and cooling rates of 2 K min^{-1}. The electrochemical cells were heated in a resistance furnace similar to that described in [12] filled with a mixture of H_2 and Ar (both 0.9999 volume fraction) in a molar ratio of 1:9, with $P = 1.2\cdot10^5$ Pa. Argon gas was purified from traces of oxygen in a quartz glass tube by passing it through copper foil heated at 673 K. The flow of gas at the rate of

$2{\cdot}10^{-3}$ m^3 h^{-1} had the direction from the positive to the negative electrodes of the electrochemical cells. The temperature was maintained with an accuracy of ±0.5 K. The EMF values of the cells were measured using the voltmeter U7–9 electrometric amplifier (Ukraine) with an input impedance of above 10^{12} Ω. The equilibrium in electrochemical cells at each temperature was achieved within 2 h. The equilibrium was considered to have been reached when the EMF values were constant or their variations were not significant (below ΔE = ±0.2 mV or ± 0.1 mV for electrochemical cells (A)). The dependences of the EMF of the cells on temperature $E(T)$ were analyzed by the method described in [56, 57].

4. Results and discussion

The activity of silver in $Ag_4HgSe_2I_2$ compound was investigated using the electrochemical cell in Eq. (17). The electrochemical process in this cell can be written as follows:

$$\begin{aligned} &\mathrm{Ag} = \mathrm{Ag}^+ + e^- \text{ left side electrode (reference system)},\\ &\mathrm{Ag}^+ + e^- = \mathrm{Ag} \text{ right side electrode (sample system)},\\ &\mathrm{Ag} = \mathrm{Ag}\ (\text{in } \mathrm{Ag_4HgSe_2I_2}) \text{ overall cell reaction} \end{aligned} \tag{18}$$

The temperature dependences of the EMF of the cell (17) are shown in **Table 1** and **Figure 6**.

The relationship of *EMF* vs. *T* measured with electrochemical cell (17) was approximated by Eq. (19):

$$E/\mathrm{mV} = (-110.178 \pm 1.244) + (488.66 \pm 2.78) \cdot 10^{-3} T/\mathrm{K}\ 412 \le T/\mathrm{K} \le 482 \tag{19}$$

As described in [29], the Gibbs energy of reaction of the electrochemical cell (17) as expressed by Eq. (20) is the difference of the chemical potential (μ) of silver in $Ag_4HgSe_2I_2$ and in the standard state (pure silver):

$$\Delta_r G_r^\circ = \mu_{\mathrm{Ag}}(\mathrm{Ag_4HgSe_2I_2}) - \mu_{\mathrm{Ag}}^\circ = -EF. \tag{20}$$

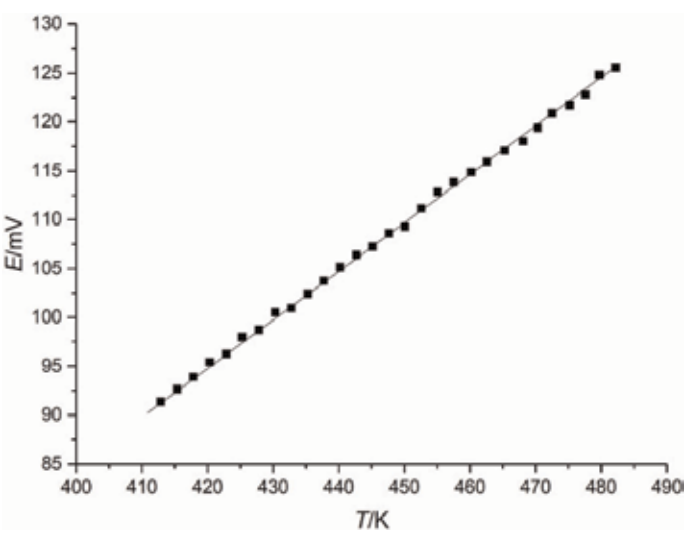

Figure 6.
The temperature dependence of EMF vs. T of electrochemical cell [17].

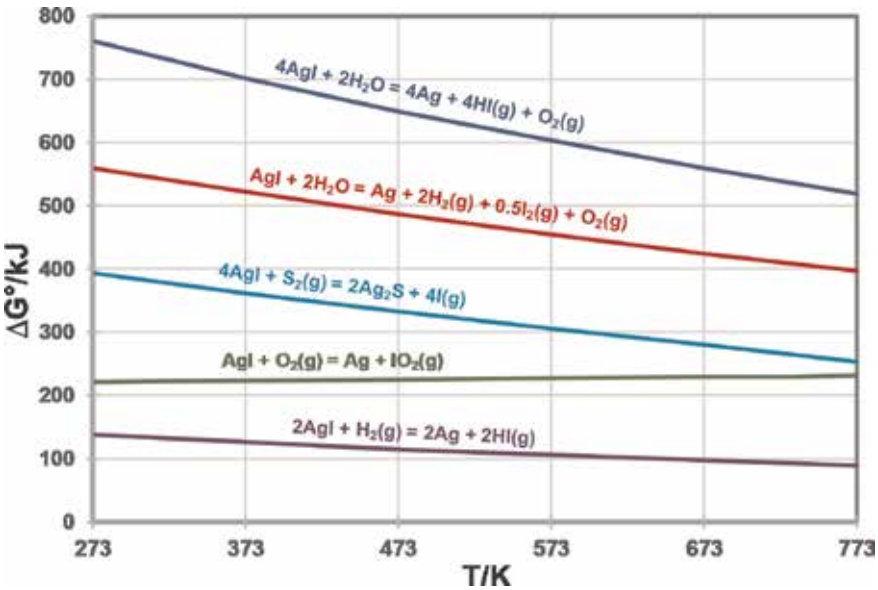

Figure 7.
Gibbs energies of reaction of AgI with $H_2O(g)$, $O_2(g)$, $H_2(g)$, and $S_2(g)$, as a function of temperature.

Using the relation

$$\mu_{Ag} = \mu^{\circ}_{Ag} + RT\ln a_{Ag}, \tag{21}$$

the activity of silver a_{Ag} in $Ag_4HgSe_2I_2$ is determined to be:

$$a_{Ag} = e^{-\frac{E_2F}{RT}} = e^{-\frac{[(-110.178\pm1.244)+(488.66\pm2.78)\cdot10^{-3}T]F}{RT}} \quad 412 \le T/K \le 482. \tag{22}$$

According to Eq. (22), the activity of silver in $Ag_4HgSe_2I_2$ compound varies between 0.075 and 0.048 in temperature range 412–482 K and decrease in accordance with the exponential law. The decrease of a_{Ag} in $Ag_4HgSe_2I_2$ with increasing temperature indicates that an increase of Ag^+ cations in the quasi-free state due to the release of the one-type capture levels [30]. Such low values of a_{Ag} indicate that $Ag_4HgSe_2I_2$ is superionic phase in the temperature range 412–482 K.

5. Summary and conclusions

Deficiencies in reliable and reproducible data have been deriving the quest for accurate experimentation. Experiences in different experimental techniques are also extremely important to the modeler to get an idea as to the errors involved in the various experimental data available in literature. This would minimize the uncertainties in thermodynamic assessments and modeling.

EMF-method is one of the versatile methods to obtain the thermodynamic data of different chemical compounds in equilibrium conditions. Since its introduction, in the late 1950s, it has been widely used to determine the thermodynamic properties of oxides, sulfides, intermetallic and several other material systems. This chapter focused on the thermodynamic investigation of solid-state materials, however, the method is applicable to investigate liquid and gas phases as well. It is the most accurate method to determine the Gibbs energies of alloys and compounds.

In studies that apply the EMF technique, selection of an appropriate electrolyte plays the key role. It is important to ascertain the conditions under which the electrolyte shows the best performance. The super ionic conducting temperature range of α-AgI is 420–713 K and that of $RbAg_4I_5$ is 298–505 K. In addition to the superionic properties even at room temperature, $RbAg_4I_5$ is more moisture resistant than AgI.

$Ag_4HgSe_2I_2$ compound was synthesized through a peritectic reaction L + β-$Ag_2Se \leftrightarrow Ag_4HgSe_2I_2$ at T = 917 K. Using the EMF method, standard thermodynamic properties of $Ag_4HgSe_2I_2$ and activity of silver in it are determined for the first time. The extremely low values of activity of silver in $Ag_4HgSe_2I_2$ in the temperature range 412–482 K are indicative of the superionic nature of the quaternary compound.

Acknowledgements

The authors are grateful to the Academy of Finland (311537) for financial support. This work was made under a project "Thermodynamic investigation of complex inorganic material systems for improved renewable energy and metals production processes" as part of the activities of the Johan Gadolin Process Chemistry Centre at Åbo Akademi University.

Conflict of interest

The authors declare no conflict of interest.

Author details

Fiseha Tesfaye[1*], Mykola Moroz[2], Oleksandr Reshetnyak[3], Daniel Lindberg[4], Pekka Taskinen[4] and Leena Hupa[1]

1 Johan Gadolin Process Chemistry Centre, Laboratory of Inorganic Chemistry, Åbo Akademi University, Turku, Finland

2 Department of Chemistry and Physics, National University of Water and Environmental Engineering, Rivne, Ukraine

3 Department of Physical and Colloid Chemistry, Ivan Franko National University of Lviv, Lviv, Ukraine

4 Department of Chemical and Metallurgical Engineering, Aalto University, Aalto, Finland

*Address all correspondence to: fiseha.tesfaye@abo.fi

References

[1] Kiukkola K, Wagner C. Measurements on galvanic cells involving solid electrolytes. Journal of the Electrochemical Society. 1957;**104**: 379-387

[2] Hannay NB (Ed.), Treatise on Solid State Chemistry. Reactivity of Solids. Volume 4. Plenum Press, New York-London, 1976. DOl: 10.1007/978-1-4684-8082-5.

[3] Ipser H, Mikula A, Katayama I. Overview: The emf method as a source of experimental thermodynamic data. CALPHAD: Computer Coupling of Phase Diagrams and Thermochemistry. 2010;**34**:271-278

[4] Kissin SA, Scott SD. Device for the measurement of sulfur fugacity mountable on the precession camera. American Mineralogist. 1979;**64**: 1306-1310

[5] Kubaschewski O, Alcock CB. Metallurgical Thermochemistry, International Series on Metallurgical Science and Technology. 5th ed. Vol. 24. Oxford; New York: Pergamon Press; 1979. p. 449

[6] Mikula A, Chang YA, Sommer F, editors. Thermodynamics of Alloy Formation. Warrendale, PA: TMS; 1997. p. 77

[7] Mikula A. The physical properties of electronic materials as determined by EMF measurements. JOM. 2007;**59**(1): 35-37

[8] Moser Z, Fitzner K. The use of experimental thermodynamic data in the phase equilibria verification. Thermochimica Acta. 1999;**332**(1):1-19

[9] Aune RE, Fredriksson P, Seetharaman S. Impact of experimentation in thermodynamic studies of some metallic and oxydic systems. Journal of Mining and Metallurgy. 2002;**38B**(3–4):213-227

[10] Tubandt C. Über elektrizitätsleitung in festen kristallisierten verbindungen, zweite mitteilung, überführung und wanderung der ionen in einheitlichen festen elektrolyten. Zeitschrift für Anorganische Chemie. 1921;**115**:105-126

[11] Takahashi T, Yamamoto O, Yamada S, Hayashi S. Solid-state ionics: High copper ion conductivity of the system CuCl-CuI-RbCl. Journal of the Electrochemical Society. 1979;**126**(10): 1654. DOI: https://doi.org/10.1149/1.2128770

[12] Tesfaye F, Taskinen P, Aspiala M, Feng D. Experimental thermodynamic study of intermetallic phases in the binary Ag–Te system by an improved EMF method. Intermetallics. 2013;**34**: 56-62

[13] Lebedev VA. Dynamic versions of EMF method in studies of phase formation and thermodynamic properties of metal alloys. Russian Journal of Electrochemistry. 2010; **46**(6):646-651

[14] Kummer JT. β-Alumina electrolytes. Progress in Solid State Chemistry. 1972; 7:141-175

[15] Pratt JN. Applications of solid electrolytes in thermodynamic studies of materials: A review. Metallurgical and Materials Transactions. 1990;**21**(4): 1223-1250. DOI: 10.1007/BF02656541

[16] Katayama I, Kozuka Z. Galvanic sensors for oxygen, SO_x or sodium using beta-alumina. Nippon Kinzoku Gakkai Kaiho. 1985;**24**:630

[17] Katayama I, Kozuka Z. Thermodynamic study of alloys and oxides by solid electrolyte cells. Nippon Kinzoku Gakkai Kaiho. 1986;**25**:528

[18] Stevens R, Binner JGP. Structure, properties and production of P-alumina. Journal of Materials Science. 1984;**19**: 695-715

[19] Collongues R, Gourier D, Kahn A, Boilot JP, Ph C. β-Alumina, a typical solid electrolyte: Latest developments in fundamental approach and in battery utilization. Journal of Physics and Chemistry of Solids. 1984;**45**:981

[20] Itoh M, Kozuka Z. Ion selectivity of beta-alumina during the coulometric titration of liquid Pb-Na alloys. Journal of Electrochemical Society. 1988;**135**(9): 2238-2242

[21] West AR. Solid electrolytes. Berichte der Bunsengesellschaft für Physikalische Chemie. 1989;**93**:1235-1241

[22] Ferloni P, Magistris A. Recent developments en electrochemie. Le Journal de Physique IV. 1994;**4**(3):C1

[23] Tatsumisago M, Saito T, Minami T. Fabrication of mesoscopic composites composed of α-AgI and AgI-based superionic glass. Thermochimica Acta. 1996;**280/281**:333-341

[24] Choudhary CB, Maiti HS, Subbarao EC. Defect structure and transport properties. In: Subbarao EC, editor. Solid Electrolytes and their Applications. New York and London: Plenum Press; 1980. pp. 1-80

[25] Johan MR, Tay SL, Hawari NL, Suan S. Phase transition and complex impedance studies of mechano-chemically synthesized AgI-CuI solid solutions. International Journal of Electrochemical Science. 2011;**6**:6235-6243

[26] Geller S. In: Geller S, editor. Solid Electrolytes, Topics in Applied Physics. Vol. 21. New York: Springer-Verlag; 1977

[27] Takahashi T. Solid silver ion conductors. Journal of Applied Electrochemistry. 1973;**3**:79-80

[28] Hull S, Keen DA, Sivia DS, Berastegui P. Crystal structures and ionic conductivities of ternary derivatives of the silver and copper monohalides. Journal of Solid State Chemistry. 2002;**165**:363-371

[29] Johnston WV, Wiedersich H, Lindberg GW. Heat capacity, transformations, and thermal disorder in the solid electrolyte RbAg4I5. The Journal of Chemical Physics. 1969;**51**: 3739-3747

[30] Sato H. Some theoretical aspects of solid electrolytes. In: Geller S, editor. Solid Electrolytes, Topics in Applied Physics. Vol. 21. Berlin, Heidelberg, New York: Springer-Verlag; 1977. pp. 3-39

[31] Seok C, Oxtoby W. Phase transitions in AgI. Physical Review B. 1997;**56**: 11485-11492

[32] Wiedersich H, Geller S. Properties of highly conducting halide and chalcogenide solid electrolytes. In: Eyring L, O'Keeffe M, editors. The Chemistry of Extended Defects in Non-metallic Solids. Amsterdam: North-Holland; 1970. p. 629

[33] Tubandt C, Reinhold H. Über die wirkung geringer zusätze auf des elektrische leitvermögen fester salze. Zeitscrift für Elektrochemie. 1923;**29**: 313-317

[34] Owens BB, Oxley JE, Sammells AF. Application of halogenide solid electrolytes. In: Geller S, editor. Solid Electrolytes, Topics in Applied Physics. Vol. 21. Berlin, Heidelberg, New York: Springer-Verlag; 1977. pp. 67-104

[35] Patterson JW. Conduction domains for solid electrolytes. Journal of the Electrochemical Society. 1971;**118**: 1033-1039

[36] Barin I. Thermochemical Data of Pure Substances, Part I and II. New

York: VCH Verlagsgesellschaft, Weinheim/VCH Publishers; 1989

[37] Roine A. HSC Chemistry 6. Finland: Outotec Oy Research Centre; 2010

[38] Geller S. Solid electrolytes. Topics in Applied Physics. 1977;**21**:77

[39] Choudary CB, Maiti HS, Subbarao EC. In: Subbarao EC (ed). Solid Electrolytes and their Applications. New York: Plenum Press; 1980. p. 40

[40] Tsutomu M. Fast ion conducting glasses. Journal of Non-Crystalline Solids. 1985;**73**:273-284

[41] Chandra A, Bhatt A, Chandra A. Ion conduction in superionic glassy electrolytes: An overview. Journal of Materials Science and Technology. 2013; **29**:193-208

[42] Hayashi A, Yoshizawa M, Angell CA, Mizuno F, Minami T, Tatsumisago M. Electrochem. Solid State Letters. 2003;**6**:E19

[43] Tatsumisago M, Shinkuma Y, Minami T. Stabilization of superionic α-Agl at room temperature in a glass matrix. Nature. 1991;**354**:217-218. DOI: 10.1038/354217a0

[44] Tatsumisago M, Hayashi A. Superionic glasses and glass–ceramics in the Li_2S–P_2S_5 system for all-solid-state lithium secondary batteries. Solid State Ionics. 2012;**225**:342-345. DOI: 10.1016/j.ssi.2012.03.013

[45] Robinel E, Carette B, Ribes M. Silver sulfide based glasses (I): Glass forming regions, structure and ionic conduction of glasses in GeS_2–Ag_2S and GeS_2–Ag_2S–AgI systems. Journal of Non-Crystalline Solids. 1983;**57**:49-58. DOI: 10.1016/0022-3093(83)90407-6

[46] Roos J, Brinkmann D, Mali M, Pradel A, Ribes M. $(AgI)_x(Ag_2S{\cdot}GeS_2)_{1-x}$ glasses studied by ^{109}Ag NMR. Solid State Ionics. 1988;**28–30**:710-712

[47] Moroz MV, Demchenko PY, Prokhorenko SV, Moroz VM. Physics of the Solid State. 2013;**55**:1613-1618. DOI: 10.1134/S1063783413080209

[48] Moroz MV, Demchenko PY, Mykolaychuk OG, Akselrud LG, Gladyshevskii RE. Synthesis and electrical conductivity of crystalline and glassy alloys in the Ag_3GeS_3Br-GeS_2 system. Inorganic Materials. 2013; **49**:867-871. DOI: 10.1134/S0020168513090100

[49] Moroz M, Demchenko P, Romaka V, Serkiz R, Akselrud L, Gladyshevskii R, et al. $Ag_3Ge_2S_5Br$: Synthesis, structure and ionic conductivity. Chemistry of Metals and Alloys. 2014;**7**:139-148

[50] Moroz MV, Prokhorenko MV, Prokhorenko SV. Determination of thermodynamic properties of Ag_3SBr superionic phase using EMF technique. Russian Journal of Electrochemistry. 2015;**51**:886-889. DOI: 10.1134/S1023193515090098

[51] Moroz MV, Prokhorenko MV, Demchenko PY, Reshetnyak OV. Thermodynamic properties of saturated solid solutions of Ag_7SnSe_5Br and Ag_8SnSe_6 compounds in the Ag–Sn–Se–Br system measured by the EMF method. The Journal of Chemical Thermodynamics. 2017;**106**:228-231. DOI: 10.1016/j.jct.2016.12.004

[52] Moroz M, Prokhorenko MV, Reshetnyak OV, Demchenko PY. Journal of Solid State Electrochemistry. 2017;**21**:833-837. DOI: 10.1007/s10008-016-3424-z

[53] Moroz M, Tesfaye F, Demchenko P, Prokhorenko M, Lindberg D, Reshetnyak O, et al. Determination of the thermodynamic properties of the $Ag_2CdSn_3S_8$ and Ag_2CdSnS_4 phases in the Ag–Cd–Sn–S system by the

solid-state electrochemical cell method. The Journal of Chemical Thermodynamics. 2018;**118**:255-262. DOI: 10.1016/j.jct.2017.12.001

[54] Mohr PJ, Newell DB, Taylor BN. CODATA Recommended Values of the Fundamental Physical Constants: 2014. Gaithersburg, MD: National Institute of Standards and Technology; 2015. pp. 1-11

[55] Agrawal RC, Gupta RK. Superionic solid: Composite electrolyte phase—An overview. Journal of Materials Science. 1999;**34**:1131-1162. DOI: 10.1023/A: 1004598902146

[56] Osadchii EG, Echmaeva EA. The system Ag-Au-Se: Phase relations below 405 K and determination of standard thermodynamic properties of selenides by solid-state galvanic cell technique. American Mineralogist. 2007;**92**: 640-647

[57] Owens BB, Argue GR. High-conductivity solid electrolytes: MAg_4I_5. Science. 1967;**157**(3786):308-310. DOI: 10.1126/science.157.3786.308

Section 2

Thermophysical Properties at Nano Scale

Chapter 4

Nanofluid: New Fluids by Nanotechnology

Mahmoud Salem Ahmed

Abstract

Recently, nanotechnology has played a major part in multifields of heat transfer processes and developed a remarkable progress in the energy applications. One of the most plausible applications of nanotechnology is to produce nanoparticles of high thermal conductivity and mixing with the base fluids that transfer energy forming what is called nanofluids. Adding of nanoparticles to the base fluid shows a remarkable enhancement of the thermal properties of the base properties. Nanotechnology has greatly improved the science of heat transfer by improving the properties of the energy-transmitting fluids. A high heat transfer could be obtained through the creation of innovative fluid (nanofluids). This also reduces the size of heat transfer equipment and saves energy.

Keywords: nanofluids, nanoparticles, thermal conductivity, base fluids

1. Introduction

Nowadays, the energy demand worldwide is steadily increasing due to the fast progress in technology in all fields of life. On the other hand, the fossil fuel had been taken to decrease, and the alternatives of energy sources are still under research to raise their efficiency. Besides, the fossil fuel has led to the environment degradation and global warming [1].

Revolution of nanotechnology and its unique features compared with the large scale of its originality has been given a major focus. This dramatic growth stemmed from the multiapplications in various fields of life: medicine, agriculture, engineering, and industry. Nanotechnology, as a scientific major, studies the properties of nanoscale materials. Nanotechnology-based techniques could be produced by small particles in the size of nano of some solid materials such as alumina and titanium oxide that have relatively high thermal conductivity. The word "nano" is described as 1 billionth of meter or 10^{-9} m. **Figure 1** shows a comparative sample of different sizes of materials from large scales to nanoscales. These nanosized particles are mixed in the base fluid of heat transfer forming a colloidal solution in the stable case, while its addition to the base fluids of low thermal conductivity probably increases the heat transfer characteristics of the base fluids. This creative fluid is known as nanofluid, which has a new heat transfer characteristic as one of the recent outcomes of nanotechnology. This makes, of course, saving energy exactly similar to reducing the volume of heat transfer equipment.

Nanotechnology has been widely used in various engineering applications as a promising alternative in saving energy and reducing the cost of producing

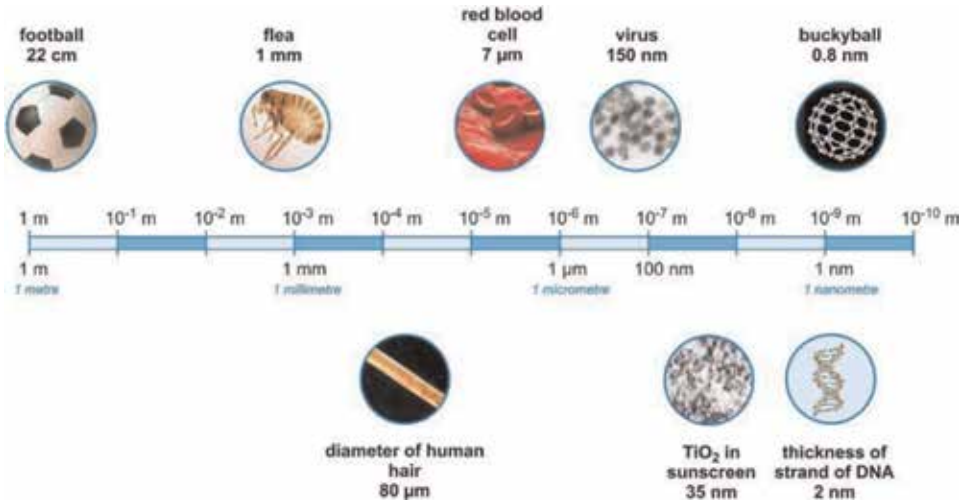

Figure 1.
A comparative of things from large scale to nanoscale.

engineering facilities. This important application is represented by the reduction of nanoparticles to the size of the nanoparticles and their mixing with fluids of low thermal properties to give a good type of fluid known as nanofluid.

2. Nanofluids

With the advancement of nanotechnology and its ability to increase the performance of solar devices by exploiting it, a new fluid known as nanofluid has been originated. This is assembled by mixing the base fluid of low thermal conductivity with solid nanoparticles of high thermal conductivity, and hence the new fluid (nanofluids) has high transfer characteristic compared with the base fluids [1, 2]. A nanofluid is a fluid in which nanometer-sized particles, suspended in the base fluid, form a colloidal solution of nanoparticles in a base fluid. The nanoparticles used in nanofluids are typically made of metals, oxides, carbides, or carbon nanotubes, while the base fluids include water, ethylene glycol, and oil. Nanofluids have novel properties that make them potentially useful in many applications in heat transfer, including microelectronics, fuel cells, pharmaceutical processes, and hybrid-powe red engines, engine cooling/vehicle thermal management, domestic refrigerator, chiller, and heat exchanger and in grinding, machining, and in boiler flue gas temperature reduction.

2.1 Methods of preparing nanofluids

Nanofluids are produced by several techniques: first step, second step, and other techniques. To avoid the sedimentation of nanoparticles during its operation, surfactant may be added to them. Nanofluid preparation is the first step ahead of any implementations. Therefore, it entails more focus from researchers to obtain a good stage of stability. Colloidal theory states that sedimentation in suspensions ceases when the particle size is below a critical radius due to counterbalancing gravity forces by the Brownian forces. Nanoparticles of a smaller size may be a better size in the different applications. However, it has a high surface which leads to the formation of agglomerates among them [3, 4]. Therefore, to obtain a stable nanofluid with optimum particle diameter and concentration, it is considered a big challenge

for researchers. Two common methods are used to produce nanofluids, the two-step method and the one step method, and others have worked up some innovations.

2.1.1 The two-step method

The two-step method is the common method to produce nanofluids. Nanoparticles of different materials including nanofibers, nanotubes, or other nanomaterials are first produced as nanosized from 10 to 100 nm by chemical or physical methods. Then, the nanosized powder will be dispersed in base fluids with the help of intensive magnetic force agitation, ultrasonic agitation, high-shear mixing, homogenizing, and ball milling. As resulting from high surface area and surface activity, nanoparticles tend to aggregate reflecting adversely on the stability of nanofluid [4–8]. To avoid that effect, the surfactant is added to the nanofluids.

The two-method preparation has been done by many researchers [9–14].

Figure 2 shows a block diagram of preparation of two-step method [15].

2.1.2 One-step method

The one-step process is simultaneously making and dispersing the particles in the base fluids which could be reduced to the agglomeration of nanoparticles. This method makes the nanofluid more stable with a limitation of the high cost of the process [16–25].

2.1.3 Other created methods

Some researchers create other methods to obtain new prepared methods for nanofluid with relatively high characteristics and more stability. Wei et al. [26] developed a method to synthesize copper nanofluids. This method can be synthesized through a novel precursor transformation with the help of ultrasonic and microwave irradiation [27]. Chen et al. [28] obtain monodisperse noble-metal colloids through using a phase-transfer method. Feng et al. [29] have used the aqueous-organic phase-transfer method for preparing gold, silver, and platinum nanoparticles with the solubility in water. Phase-transfer method is also used to prepare stable kerosene-based F_3O_4 nanofluids [30]. As stated above, the research proved that nanofluids synthesized by chemical solution method could be enhanced in conductivity with more stability [31].

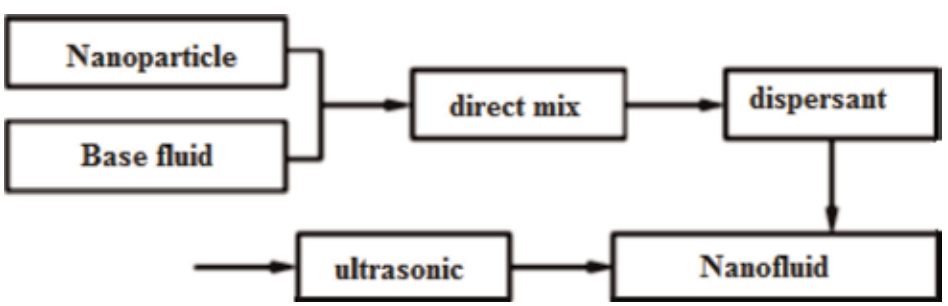

Figure 2.
Two-step method of preparation of nanofluids [15].

2.2 Thermophysical properties of nanofluids

Nanofluids have novel properties different from base fluids that included thermophysical properties such as specific heat, density, viscosity, and thermal conductivity.

Mixing the nanoparticles into the base fluid changes the thermophysical properties of the base fluid. The most important thermophysical properties of nanofluids are nanofluid viscosity, nanofluid convective heat transfer, nanofluid thermal conductivity, and nanofluid specific heat.

The value of specific heat and density of the nanofluids can be determined by correlations, whereas the viscosity and thermal conductivity have different correlations.

2.2.1 Nanofluid thermal conductivity

Conventional heat transfer fluids, such as oil, water, and ethylene glycol (EG) mixture, are poor heat transfer fluids. Hence, many trials by researchers to enhance the heat transfer convection of these fluids through increasing their thermal conductivity. High thermal conductivity is obtained for the nanofluids by adding nanoparticle of solid materials of high thermal conductivity.

Nanofluids are basically advanced heat transfer fluids as an alternative to the pure base fluids to improve the heat transfer process through the addition of nanoparticle materials that have the properties of higher thermal conductivity. This attracted the attention of researchers to test many nanoparticles that have different thermal conductivity to obtain a high rate of heat transfer and use them in different applications.

The literature reported multiequations describing the thermal conductivity of nanofluids. The prominent results reported that there are improvements of 5–10% of the thermal conductivity of nanofluids using the base fluid (water, PAO). As is reported, there is no critical improvement in the thermal conductivity in comparison to the conventional base fluid dependent on particle size and base fluid thermal conductivity [32–37].

Conventional models of effective thermal conductivity of suspensions are reported for some researchers [32].

$$\frac{\mathrm{k_{eff}}}{\mathrm{k_m}} = 1 + \frac{3\,(\alpha - 1)\,\mathrm{v}}{(\alpha + 2) - (\alpha - 1)\mathrm{v}} \tag{1}$$

$$\frac{k_{eff}}{k_m} = \frac{\alpha + (n-1) - (n-1)(1-\alpha)\,v}{(\alpha+2) - (\alpha-1)v} \tag{2}$$

$$\frac{k_{eff}}{k_m} = 1 + 3\beta v + \left(3\beta^2 + \frac{3\beta^2}{4} + \frac{9\beta^2(\alpha+2)}{16(2\alpha+3)} + \ldots\right)v^2 \tag{3}$$

$$\frac{k_{eff}}{k_m} = 1 + \frac{3(\alpha-1)}{(\alpha+2)-(\alpha-1)v}\left[v + f(\alpha)v^2 + 0\left(\alpha^3\right)\right] \tag{4}$$

where k_{eff} is the effective thermal conductivity of the suspension, n is a shape factor of nanoparticle, ν is nanoparticle volume fraction, and k_m and k_c are the thermal conductivity of the suspending medium and solid particle, respectively. Also α and β are empirical fitting parameters which are defined as (k_c/k_m) and $(\alpha - 1)/(\alpha + 1)$.

2.2.2 Nanofluid convective heat transfer

Nanofluids have been proven a great potential for heat transfer enhancement [44–47]. Nanofluids have been presented as a promising tool and a good

alternative to base fluids to save energy, compact devices of low cost and design of multiequipment used in a different applications with nanofluids as working fluids.

Experimental investigation [38] on Cu- or water-based nanofluids has demonstrated great enhancement of heat transfer and also reported that friction factor has a very meager part in the application process. Other scholars [39] have concluded that a systematic and definite deterioration of the natural convective heat transfer occurs for the forced convection reliant on the solution concentration, the particle density, and the aspect ratio of the cylinder. Experimental investigation on Al_2O_3 nanofluids using water as base fluid has been studied by various research groups, and they concluded that the heat transfer coefficient in laminar flow [40–42] increases up to 12–15% and in the case of turbulent flow, it ranges up to 8% [43, 44]. CNT, CuO, SiO, and TiO_2 nanofluids using water have been investigated [45–47]. Among these, CNT nanofluid produced similar results to that of Al_2O_3 nanofluid. Ding et al. [48] have concluded that the enhancement of heat transfer could be obtained by varying the flow condition and the fluid concentration. Alternatively, CuO has been investigated for several wall boundary conditions, and it has reached good results [3]. The increase in the concentration of the nanofluid on contrary gives very weak results on the heat transfer coefficient for volume fraction greater than 0.3% [49]. It is noted from the experiments that the heat transfer coefficient enhancement can be achieved in the range of 2–5%.

2.2.3 Nanofluid viscosity

Viscosity is one of the parameters that influences the behavior of nanofluids. Researchers have conducted experiments to test the viscosity through adding the nanoparticles to the different base fluids, and hence they found out that the viscosity is significantly affected by both variations of temperature and volume fraction of nanoparticles [50–56]. They have reported correlated equations to quantify the viscosity based on their experiments using different nanofluids. The following correlated equations are examples that have been reported by some researchers.

$$\mu_{eff} = \left(1 + 2.5\varnothing_p + 7.349\varnothing_p^2 + \ldots\right)\mu_b \tag{5}$$

Model for spherical nanoparticles [57]:

$$\mu_{nf} = \mu_f \frac{1}{(1-\varnothing)^{2.5}} \tag{6}$$

Model for simple hard sphere systems, the relative viscosity increases with particle volume fraction ø [57]:

$$\mu_{eff} = \frac{9}{8}\frac{\left(\varnothing_p/\varnothing_{pmax}\right)^{\frac{1}{3}}}{1-\left(\varnothing_p/\varnothing_{pmax}\right)^{\frac{1}{3}}}\mu_b \tag{7}$$

The model is valid for spherical nanoparticles and for $0.5236 \leq \Phi \leq 0.7405$ [55]. Meaning of Φ = volume fraction and μ = dynamic viscosity.

The SiO_2 nanofluid has been investigated [48] and concluded that nanofluid viscosity is dependent on the volume fraction. Other researchers [58] have analyzed commercial engine coolants dispersed with alumina particles. They found out that the nanofluid produced with calculated amount of oleic acid (surfactant) has been tested for stability. While the pure base fluid demonstrates Newtonian behavior over the measured temperature, it turns to a non-Newtonian fluid with addition of a few alumina nanoparticles.

2.2.4 Nanofluid specific heat

The specific heat of material is quite an important property to define the thermal performance of any material [36]. Specific heats of nanofluids may differ according to the type of base fluids, nanomaterials, and concentration of nanoparticles found in base fluids. Pak and Cho [59] have investigated the impact of volume fraction of Al_2O_3 on specific heat. The investigation showed that 1.10–2.27% decrease in specific heat occurred for 1.34–2.78% volume fraction of nanoparticle size of 13 nm. Zhao et al. [68] also noticed a fall in the specific heat capacity of CuO nanofluid by 1.16–5% compared to base fluid EG for volume fraction of 0.1–0.6% and particle size which ranges from 25 to 500 nm. Some nanofluids show inconsistent behavior with volume convergence. Shahrul et al. [60] have conducted a comparative revision on the specific heat of nanofluids used in energy applications. They have concluded that for most nanomaterials in base fluids, specific heat decreases with the increase in volume fraction. Sonawane et al. [61] have investigated specific heat of Al_2O_3/ATF and reported the anomalous conduct of specific heat with volume convergence. Increase in specific heat capacity has also been reported in experimental observations [36, 62–68]. Fakoor Pakdaman et al. [69] have found out that there is 21–42% decrease in specific heat capacity of MWCNT/water nanofluid for 0.1–0.4% vol. a fraction in the range of 5–20 nm size. However, Kumaresan et al. [64] have observed 2.31–9.35% gain. In specific heat capacity of MWCNT/(EG/DW, 30/70) nanofluid for 0.15–0.45% concentration, particle size was kept at 30–50 nm. Nowadays, the result of experimental data does not signal a discreet and clear-cut indication that there is the only reduction in the heat capacity with an increment of volume concentration, as has been reported by several academic figures. Experimental observations on various nanofluids show increase of specific heat capacity [62–70], whereas experimental observations exhibit decrease in specific heat capacity performed by many researchers [59, 61, 71–81].

The specific heat of nanofluid can be determined as function of the particle volume concentration using the following equation [80]:

$$\left(\rho C_p\right)_{eff} = (1-\varphi)\left(\rho C_p\right)_{bf} + \varphi\left(\rho C_p\right)_p \tag{8}$$

And

$$\rho_{eff} = (1-\varphi)\rho_{bf} + \varphi\rho_p \tag{9}$$

3. Applications of nanofluids for heat transfer process

Nowadays, nanofluids play a vital role in heat transfer equipment as a good alternative in developing the efficiency of the heat transfer equipment and in turn of reducing the size of the equipment and saving energy.

Since water is a good medium for heat transfer and it is also a good medium for receiving and storing solar energy during sunrise time, therefore, water is a good medium for the heating processes and one important source for the application of solar energy [2, 82, 83]. It is granted that the thermal efficiency of the FPSWH is relatively low, and therefore researchers have exerted many efforts to increase its performance. The thermal efficiency of the FPSWH has improved by using specific techniques [84]. Researchers to enhance the performance of FPSWH and the thermal efficiency using different methods [85–89] have conducted many studies.

The recent researches have revealed that nanofluids have a large effect on increasing heat transfer. This is done through mixing the nanoparticles materials that have high thermal conductivity into the working fluid (or called the base fluid).

Now, nanofluids are promising mediums as alternatives to the base fluids, and hence the researches are still under investigation to improve and develop the heat transfer equipment systems.

Many works have been conducted to improve the performance of flat plate solar water heater using different nanoparticles to the base fluid [63–73].

To improve the performance of flat plate solar collector, scholars had conducted experimental and theoretical studies on flat plate solar collector using nanofluids with different binary materials (nanoparticles + base fluids) as a working fluid.

Salem Ahmed et al. [90] have conducted an experimental work on the performance of chilled water air conditioning unit with and without alumina nanofluids.

They have used the first method to prepare Al_2O_3 water nanofluids with different concentrations by weight, which vary from 0.1, 0.2, 0.3, and 1% wt. Under operation conditions, experiments have been investigated including a variation of flow rate of chilled water/alumina nanofluids and the air through the cooling coil. The results have shown that less time is scored to get the desired chilled fluid temperature for all the different concentrations of nanofluids (Al_2O_3-water) compared with pure water.

Again, the findings have shown a reduction of the power consumption and increase in the cooling capacity, which is in turn an increase in the COP by about 5 and 17% for alumina nanoparticles, concentration of 0.1 and 1% by weight, respectively. A schematic diagram of the experimental work shown in **Figures 3** and **4** shows the TEM image of the alumina nanoparticles (Al_2O_3) used in the experiments.

Xu et al. [91] have conducted experimental and theoretical studies comparing a novel of parabolic trough concentrator with traditional solar water heater using nanofluid, CuO/oil. **Figure 5** shows a configuration of the novel parabolic trough concentrator and the traditional solar heater.

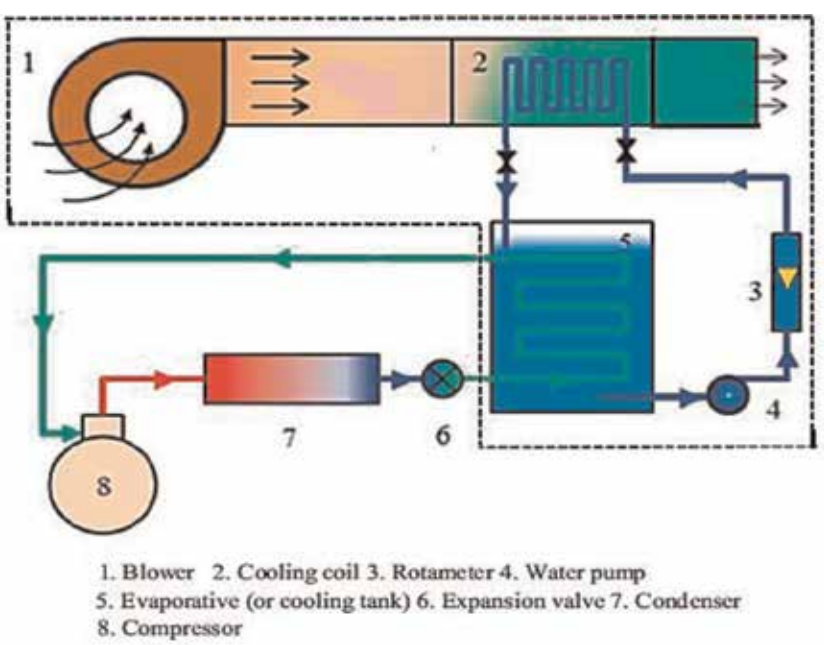

Figure 3.
A schematic diagram of the chilled-water air conditioning unit [90].

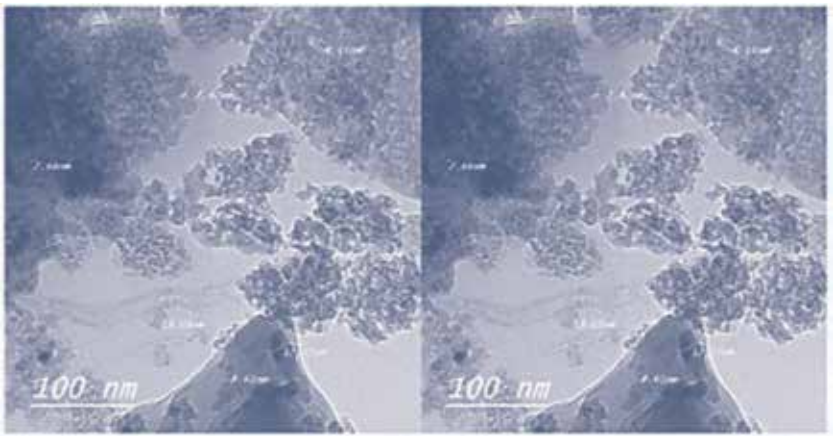

Figure 4.
TEM image of Al_2O_3 nanoparticles used in the experiments [90].

As is shown in **Figure 5b**, a kind of oil added with certain nanoparticles (CuO) acts as a working fluid. The nanoparticles dispersed in the oil inside the inner tube directly capture the solar radiation instead of the tube wall coating. The solar collection efficiency curves for the two collectors suggested that the NDASC was superior to a conventional IASC within a preferred working temperature range, but inferior when the tf exceeded a specific critical temperature (*t*cr) as shown in **Figure 6**.

Said et al. [92] have used TiO_2-water nanofluid as a working fluid for enhancing the performance of a flat plate solar collector for the volume fraction of the nanoparticles 0.1 and 0.3%, respectively, and mass flow rates of the nanofluid vary from 0.5 to 1.5 kg/min, respectively. Thermophysical properties and reduced sedimentation for TiO_2 nanofluid have been obtained using PEG 400 dispersant. Energy efficiency has increased by 76.6% for 0.1% volume fraction and 0.5 kg/min

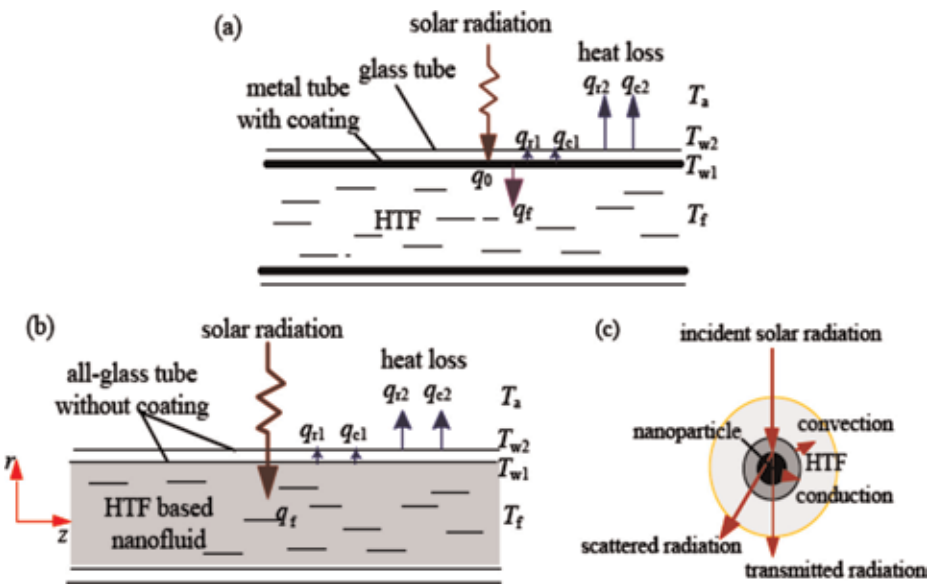

Figure 5.
Schematics of solar collection principles. (a) A conventional indirect absorption solar collector (IASC); (b) the proposed novel nanofluid-based direct absorption solar collector (NDASC); and (c) the heat transfer around nanoparticles inside the tube of NDASC [91].

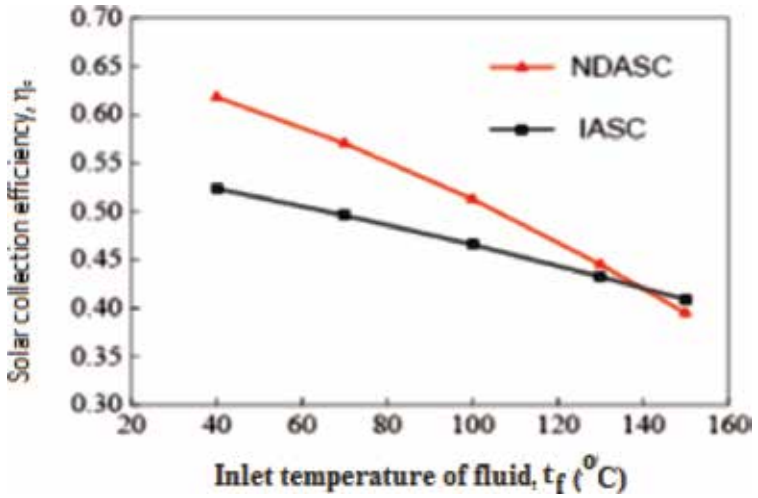

Figure 6.
Variations of solar collection efficiencies with tf,i for both the NDASC and the IASC [91].

flow rate, whereas the highest energy efficiency obtained has been 16.9% for 0.1% volume fraction and 0.5 kg/min flow rate.

The thermal efficiency of the FPSC (μ) and the energy efficiency are given, respectively, as [92].

The schematic of the solar collector and the experiment is presented in **Figure 7**. They also showed that the pressure drop and pumping power of TiO_2 nanofluid were very close to the base fluid for the studied volume fractions [92].

Polvongsri et al. [93] have performed an experimental work to study the performance of a flat plate solar collector (**Figure 8**) using a silver nanofluid as the

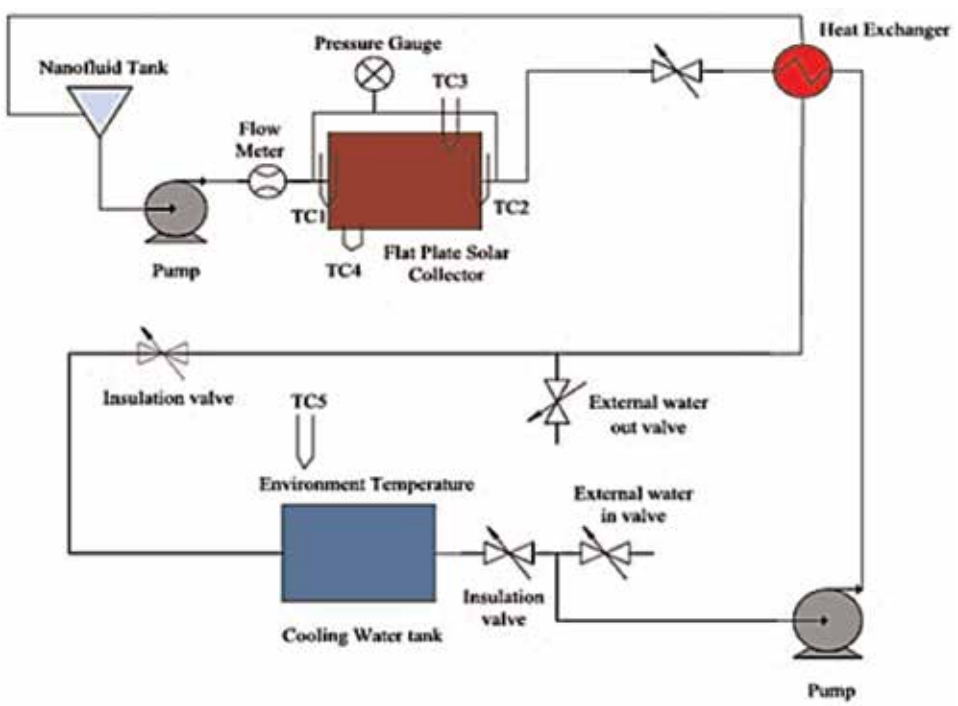

Figure 7.
The presentation of the experimental setup in schematic diagram [92].

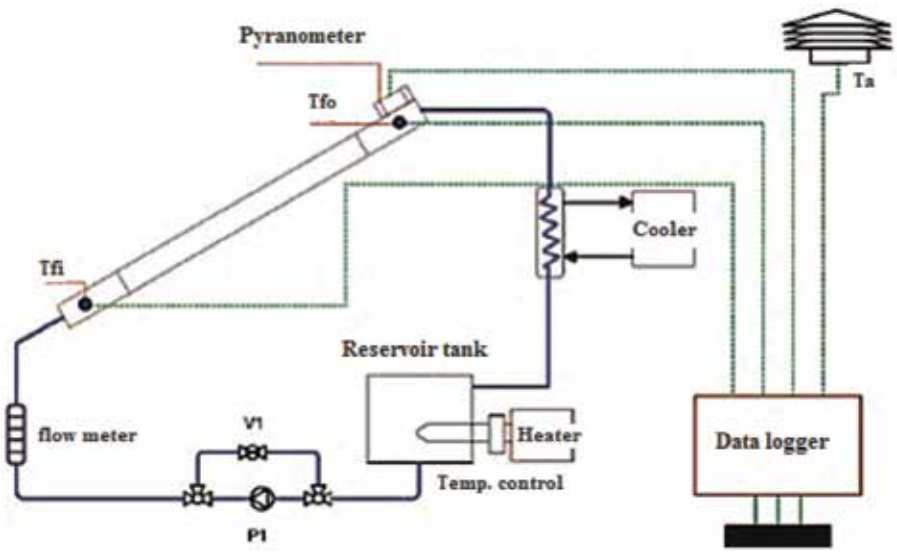

Figure 8.
Diagram of the experimental setup [93].

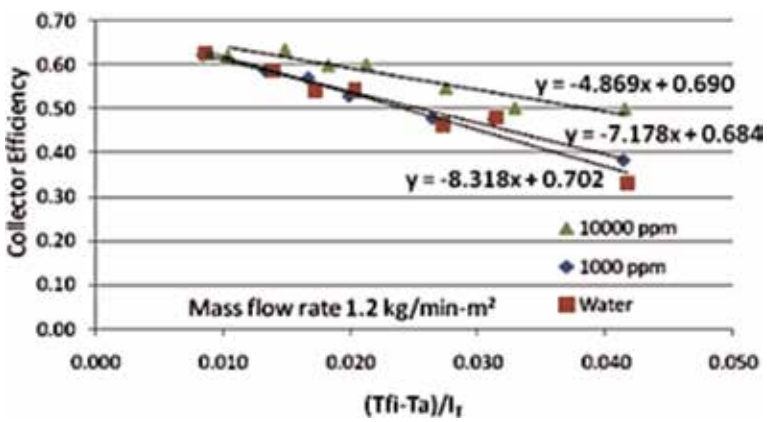

Figure 9.
The performance curves of silver nanofluid at 10,000 and 1000 ppm and water [93].

working fluid, while water was mixed with 20 nm silver nano with concentrations of 1000 and 10,000 ppm. The operating conditions of experiments to be done at a flow rate of working fluid between 0.8 and 1.2 l/min-m^2 and the inlet temperature were controlled in a range of 35–65°C.

It is remarkable that using silver nanofluid as a working fluid could improve the thermal performance of flat plate collector compared with water, especially at high inlet temperature as shown in **Figure 9**.

4. Conclusions

This chapter reviews the recent applications of nanotechnology for nanofluids. These applications revealed that nanofluids have a promising alternative to enhance the performance of heat transfer equipment considering the cost, safety, potential of size reduction, and environmental protection. The present chapter provides a

comprehensive overview of nanofluid as one of the important applications of nanotechnology and how to obtain it and its thermal properties. There are challenges hindering the preparation of nanomaterials, including the stability of nanofluids to take into consideration and worthy of attention on the part of researchers.

Author details

Mahmoud Salem Ahmed
Faculty of Industrial Education, Mechanical Department, Sohag University, Sohag, Egypt

*Address all correspondence to: mahmoudsalem.ahmed@yahoo.com

References

[1] Bozorgan N, Shafahi M. Performance evaluation of nano-fluids in solar energy: A review of the recent literature. Micro and Nano Systems Letters. 2015;**35**:1-15

[2] Hussain HA, Jawad Q, Sultan KF. Experimental analysis on thermal efficiency of evacuated tube solar collector by using nano-fluids. International Journal of Sustainable and Green Energy. 2015;**4**:19-28

[3] Witharana S, Palabiyik I, Musina Z, Ding Y. Stability of glycol nanofluids—The theory and experiment. Powder Technology. 2013;**239**:72-77

[4] Jailani S, Franks GV, Healy TW. The potential of nanoparticle suspensions: Effect of electrolyte concentration, particle size and volume fraction. Journal of the American Ceramic Society. 2008;**91**:1141-1147

[5] Yu W, Huaqing XA. Review on nano-fluids: Preparation, stability mechanisms, and applications. Journal of Nanomaterials. 2012;**2012**:435873. 17p

[6] Quddoos A, Anand A, Mishra GK, Nag P. Nano-fluids: Introduction, preparation, stability analysis and stability enhancement techniques. IJPAS. 2014;**1**:31-36

[7] Neto ET, Filho EPB. Preparation methods of nano-fluids to obtain stable dispersions. In: 13th Brazilian Congress of Thermal Sciences and Engineering; December 5–10, 2010

[8] Micha D, Marcin L, Grzegorz D, Andrzej G. Preparation of metal oxide-water nanofluids by two-step method. Prosimy Cytowa Jako: Inżynieria I Aparatura Chemiczna. 2012; **51**:213-215

[9] Barrett TR et al. Investigating the use of nanofluids to improve high heat flux cooling systems. Fusion Engineering. 2013;**88**:2594-2597

[10] Patel HE, Das SK, Sundararajan T, Sreekumaran Nair A, George B, Pradeep T. Thermal conductivities of naked and monolayer protected metal nanoparticle based nanofluids: Manifestation of anomalous enhancement and chemical effect. Applied Physics Letters. 2003;**83**: 2931-2933

[11] Xuan Y, Li Q. Heat transfer enhancement of nanofluids. International Journal of Heat and Fluid Flow. 2000;**21**:58-64

[12] Hu P, Shan W-L, Yu F, Chen Z-S. Thermal conductivity of AlN-ethanol nanofluids. International Journal of Thermophysics. 2008;**29**:1968-1973

[13] Kole M, Dey TK. Thermal conductivity and viscosity of AIN-ethanol nanofluids based on car engine coolant. Journal of Physics D: Applied Physics. 2010;**43**:10

[14] Beck MP, Sun T, Teja AS. The thermal conductivity of alumina nanoparticles dispersed in ethylene glycol. Fluid Phase Equilibria. 2007;**260**: 275-278

[15] Nerella S, Sudheer NVVS, Bhramara P. Enhancement of heat transfer by nanofluids in solar collectors. International Journal of Innovations in Engineering and Technology (IJIET). 2014;**3**:115-120

[16] Mukherjee S, Paria S. Preparation and stability of nano-fluids—A review. IOSR Journal of Mechanical and Civil Engineering. 2012;**9**:63-69

[17] Eastman JA, Choi SUS, Li S, Yu W, Thompson LJ. Anomalously increased effective thermal conductivities of ethylene glycol-based nano-fluids

containing copper nanoparticles. Applied Physics Letters. 2001;**78**: 718-720

[18] Li Y, Zhou J, Tung S, Schneider E, Xi S. A review on development of nano-fluid preparation and characterization. Powder Technology. 2009;**196**:89-101

[19] Lo CH, Tsung TT, Chen LC. Shape-controlled synthesis of Cu-based nano-fluid using submerged arc nanoparticle synthesis system (SANSS). Journal of Crystal Growth. 2005;**277**:636-642

[20] Lo CH, Tsung TT, Chen LC, Su CH, Lin HM. Fabrication of copper oxide nano-fluid using submerged arc nanoparticle synthesis system (SANSS). Journal of Nanoparticle Research. 2005; **7**:313-320

[21] Zhu HT, Lin YS, Yin YS. A novel one-step chemical method for preparation of copper nano-fluids. Journal of Colloid and Interface Science. 2004;**277**:100-103

[22] Bonnemann H, Botha SS, Bladergroen B, Linkov VM. Monodisperse copper- and silver-nanocolloids suitable for heat-conductive fluids. Applied Organometallic Chemistry. 2005;**19**: 768-773

[23] Singh AK, Raykar VS. Microwave synthesis of silver nano-fluids with polyvinylpyrrolidone (PVP) and their transport properties. Colloid & Polymer Science. 2008;**286**:1667-1673

[24] Kumar A, Joshi H, Pasricha R, Mandale AB, Sastry M. Phase transfer of silver nanoparticles from aqueous to organic solutions using fatty amine molecules. Journal of Colloid and Interface Science. 2003;**264**:396-401

[25] Yu W, Xie H, Wang X, Wang X. Highly efficient method for preparing homogeneous and stable colloids containing graphene oxide. Nanoscale Research Letters. 2011;**6**:1-7

[26] Wei X, Wang L. Synthesis and thermal conductivity of microfluidic copper nano-fluids. Particuology. 2010; **8**:262-271

[27] Zhu HT, Zhang CY, Tang YM, Wang JX. Novel synthesis and thermal conductivity of CuO nano-fluid. Journal of Physical Chemistry C. 2007;**111**: 1646-1650

[28] Chen Y, Wang X. Novel phase-transfer preparation of monodisperse silver and gold nanoparticles at room temperature. Materials Letters. 2008;**62**: 2215-2218

[29] Feng X, Ma H, Huang S, et al. Aqueous-organic phase transfer of highly stable gold, silver, and platinum nanoparticles and new route for fabrication of gold nanofilms at the oil/water interface and on solid supports. Journal of Physical Chemistry B. 2006; **110**:12311-12317

[30] Yu W, Xie H, Chen L, Li Y. Enhancement of thermal conductivity of kerosene-based Fe_3O_4 nano-fluids prepared via phase-transfer method. Colloids and Surfaces, A: Physicochemical and Engineering Aspects. 2010;**355**:109-113

[31] Wang L, Fan J. Nano-fluids research: Key issues. Nanoscale Research Letters. 2010;**5**:1241-1252

[32] Nagarajan PK, Subramani J, Suyambazhahan S, Sathyamurthy R. Nano-fluids for solar collector applications: A review. Energy Procedia. 2014;**61**:2416-2434

[33] Xue Q, Xu W-M. A model of thermal conductivity of nanofluids with interfacial shells. Materials Chemistry and Physics. 2005;**90**:298-301

[34] Muhammad MJ, Muhammad IA, Sidik NAC, Yazid MNAWM, Mamat R, Najafi G. The use of nano-fluids for enhancing the thermal performance of stationary solar collectors: A review. Renewable and Sustainable Energy Reviews. 2016;**63**:226-236

[35] Toshihiro W, Atsushi T, Masahiro E, Toshiyuki S, Daigo M-I, Shigehiko I, et al. Radiological impact of the nuclear power plant accident on freshwater fish in Fukushima: An overview of monitoring results. Journal of Environmental Radioactivity. 2016;**151**: 144-155

[36] Verma SK, Tiwari AK. Progress of nano-fluid application in solar collectors: A review. Energy Conversion and Management. 2015;**100**:324-346

[37] Kundan L, Sharma P. Performance evaluation of a nano-fluids (CuO-H_2O) based low flux solar collector. International Journal of Engine Research. 2013;**2**:108-112

[38] Putra N, Roetzel W, Das SK. Natural convection of nano-fluids. Heat and Mass Transfer. 2003;**39**:775-784

[39] Yang Y, Zhang ZG, Grulke EA, Anderson WB, Wu G. Heat transfer properties of nanoparticle-in-fluid dispersions (nano-fluids) in laminar flow. International Journal of Heat and Mass Transfer. 2005;**48**:1107-1116

[40] Chun BH, Kang HU, Kim SH. Effect of alumina nanoparticles in the fluid on heat transfer in double-pipe heat exchanger system. Korean Journal of Chemical Engineering. 2008;**25**:966-971

[41] Chandrasekar M, Suresh S, Chandra BA. Experimental studies on heat transfer and friction factor characteristics of Al_2O_3/water nano-fluid in a circular pipe under laminar flow with wire coil inserts. Experimental Thermal and Fluid Science. 2010;**24**:122-130

[42] Suresh S, Venkitaraj KP, Selvakumar P. Comparative study on thermal performance of helical screw tape inserts in laminar flow using Al_2O_3 water and CuO/water nano-fluids. Superlattices and Microstructures. 2011; **49**:608-622

[43] Zamzamian A, Oskouie SN, Doosthoseini A, Joneidi A, Pazouki M. Experimental investigation of forced convective heat transfer coefficient in nano-fluids of Al_2O_3/EG and CuO/EG in a double pipe and plate heat exchangers under turbulent flow. Experimental Thermal and Fluid Science. 2011;**35**: 495-502

[44] Corcione M, Cianfrini M, Quintino A. Heat transfer of nano-fluids in turbulent pipe flow. International Journal of Thermal Sciences. 2012;**56**:58-69

[45] He Y, Jin Y, Chen H, Ding Y, Cang D, Lu H. Heat transfer and flow behavior of aqueous suspensions of TiO_2 nanoparticles (nano-fluids) flowing upward through a vertical pipe. International Journal of Heat and Mass Transfer. 2007;**50**:2272-2281

[46] Yu W, France DM, Smith DS, Singh D, Timofeeva EV, Routbort JL. Heat transfer to a silicon carbide/water nano fluid. International Journal of Heat and Mass Transfer. 2009;**52**:3606-3612

[47] Anoop KB, Sundararajan T, Das SK. Effect of particle size on the convective heat transfer in nano-fluid in the developing region. International Journal of Heat and Mass Transfer. 2009;**52**: 2189-2195

[48] Ding Y, Alias H, Wen D, Williams RA. Heat transfer of aqueous suspensions of carbon nanotubes (CNT nano-fluids). International Journal of Heat and Mass Transfer. 2006;**49**: 240-250

[49] Corcione M. Empirical correlating equations for predicting the effective

thermal conductivity and dynamic viscosity of nano-fluids. Energy Conversion and Management. 2011;**52**: 789-793

[50] Chen L, Xie H, Li Y, Yu W. Nano-fluids containing carbon nanotubes treated by mechano-chemical reaction. Thermochimica Acta. 2008;**477**:21-24

[51] Li JM, Li ZL, Wang BX. Experimental viscosity measurements for copper oxide nanoparticles suspensions. Tsinghua Science and Technology. 2002;**7**:198-201

[52] Wang X, Xu X, Choi SUS. Thermal conductivity of nanoparticles—Fluid mixture. Journal of Thermophysics and Heat Transfer. 1999;**13**:474-480

[53] Frankel N, Acrivos A. On the viscosity of concentrated suspension of solid spheres. Chemical Engineering Science. 1967;**22**:847-853

[54] Namburu PK, Kulkarni DP, Debasmita M, Das Debendra K. Viscosity of copper oxide nanoparticles dispersed in ethylene glycol and water mixture. Experimental Thermal and Fluid Science. 2007;**32**:397-402

[55] Masoumi N, Sohrabi N, Behzadmehr A. A new model for calculating the effective viscosity of nano-fluids. Journal of Physics D: Applied Physics. 2009;**42**:055501

[56] Vand V. Viscosity of solutions and suspensions. The Journal of Physical and Colloid Chemistry. 1948;**52**:277-299

[57] Zhao J-F, Luo Z-Y, Ni M-J, Cen K-F. Dependence of nano-fluid viscosity on particle size and pH value. Chinese Physics Letters. 2009;**26**:256-307

[58] Kole M, Dey TK. Viscosity of alumina nanoparticles dispersed in car engine coolant. Experimental Thermal and Fluid Science. 2010;**34**:677-683

[59] Pak BC, Cho YI. Hydrodynamic and heat transfer study of dispersed fluids with submicron metallic oxide particles. Experimental Heat Transfer. 1998;**11**: 151-1700

[60] Shahrul IM, Mahbubul IM, Khaleduzzaman SS, Saidur R, Sabri MFM. A comparative review on the specific heat of nano-fluids for energy perspective. Renewable and Sustainable Energy Reviews. 2014;**38**:88-98

[61] Sonawane S, Patankar K, Fogla A, Puranik B, Bhandarkar U, Sunil KS. An experimental investigation of thermo-physical properties and heat transfer performance of Al_2O_3-aviation turbine fuel nano-fluids. Applied Thermal Engineering. 2011;**31**:2841-2849

[62] Shin D, Banerjee D. Specific heat of nano-fluids synthesized by dispersing alumina nanoparticles in alkali salt eutectic. International Journal of Heat and Mass Transfer. 2014;**74**:210-214

[63] Shin D, Banerjee D. Enhanced thermal properties of SiO_2 nanocomposite for solar thermal energy storage applications. International Journal of Heat and Mass Transfer. 2015; **84**:898-902

[64] Kumaresan V, Mohaideen Abdul Khader S, Karthikeyan S, Velraj R. Convective heat transfer characteristics of CNT nano-fluids in a tubular heat exchanger of various lengths for energy efficient cooling/heating system. International Journal of Heat and Mass Transfer. 2013;**60**:413-421

[65] Mohebbi A. Prediction of specific heat and thermal conductivity of nano-fluids by a combined equilibrium and non-equilibrium molecular dynamics simulation. Journal of Molecular Liquids. 2012;**175**:51-58

[66] Murshed SMS, Nieto de Castro CA. Superior thermal features of carbon nanotubes-based nano-fluids—A review.

Renewable and Sustainable Energy Reviews. 2014;**37**:155-167

[67] Nelson IC, Banerjee D, Ponnappan R. Flow loop experiments using polyalphaolefin nano-fluids. Journal of Thermophysics and Heat Transfer. 2009;**23**:752-761

[68] Akhavan-Behabadi MA, Pakdaman MF, Ghazvini M. Experimental investigation on the convective heat transfer of nano-fluid flow inside vertical helically coiled tubes under uniform wall temperature condition. International Communications in Heat and Mass Transfer. 2012;**39**:556-564

[69] Fakoor Pakdaman M, Akhavan-Behabadi MA, Razi P. An experimental investigation on thermo-physical properties and overall performance of MWCNT/heat transfer oil nano-fluid flow inside vertical helically coiled tubes. Experimental Thermal and Fluid Science. 2012;**40**:103-111

[70] Ho MX, Pan C. Optimal concentration of alumina nanoparticles in molten Hitec salt to maximize its specific heat capacity. International Journal of Heat and Mass Transfer. 2014;**70**:174-184

[71] Choi J, Zhang Y. Numerical simulation of laminar forced convection heat transfer of Al_2O_3–water nano-fluid in a pipe with return bend. International Journal of Thermal Sciences. 2012;**55**: 90-102

[72] Pandey S, Nema VK. Experimental analysis of heat transfer and friction factor of nano-fluid as a coolant in a corrugated plate heat exchanger. Experimental Thermal and Fluid Science. 2012;**38**:248-256

[73] Zhou S-Q, Ni R. Measurement of the specific heat capacity of water-based Al_2O_3 nano-fluid. Applied Physics Letters. 2008;**92**:1-3

[74] Kulkarni DP, Vajjha RS, Das DK, Oliva D. Application of aluminum oxide nano-fluids in diesel electric generator as jacket water coolant. Applied Thermal Engineering. 2008;**28**: 1774-1781

[75] Vajjha RS, Das DK. A review and analysis on influence of temperature and concentration of nano-fluids on thermophysical properties, heat transfer and pumping power. International Journal of Heat and Mass Transfer. 2012;**55**:4063-4078

[76] Pantzali MN, Kanaris AG, Antoniadis KD, Mouza AA, Paras SV. Effect of nano-fluids on the performance of a miniature plate heat exchanger with modulated surface. International Journal of Heat and Fluid Flow. 2009;**30**:691-699

[77] De Robertis E, Cosme EHH, Neves RS, Kuznetsov AY, Campos APC, Landi SM, et al. Application of the modulated temperature differential scanning calorimetry technique for the determination of the specific heat of copper nano-fluids. Applied Thermal Engineering. 2012;**41**:10-17

[78] Liu J, Wang F, Zhang L, Fang X, Zhang Z. Thermodynamic properties and thermal stability of ionic liquid-based nano-fluids containing graphene as advanced heat transfer fluids for medium-to-high-temperature applications. Renewable Energy. 2014; **63**:519-523

[79] He Q, Wang S, Tong M, Liu Y. Experimental study on thermophysical properties of nano-fluids as phase-change material (PCM) in low temperature cool storage. Energy Conversion and Management. 2012;**64**: 199-205

[80] Chandrasekar M, Suresh S, Senthilkumar T. Mechanisms proposed through experimental investigations on thermophysical properties and forced

convective heat transfer characteristics of various nano-fluids—A review. Renewable and Sustainable Energy Reviews. 2012;**16**:3917-3938

[81] Kumar R, Rosen MA. Integrated collector—Storage solar water heater with extended storage unit. Applied Thermal Engineering. 2011;**31**:348-354

[82] Wongsuwan W, Kumar S. Forced circulation solar water heater performance prediction by TRNSYS and ANN. International Journal of Sustainable Energy. 2005;**24**:69-86

[83] Zhang Q, Uchaker E, Candelaria SL, Cao G. Nanomaterials for energy conversion and storage. Chemical Society Reviews. 2013;**42**:3127-3171

[84] Rezania A, Taherian H, Ganji DD. Experimental investigation of a natural circulation solar domestic water heater performance under standard consumption rate. International Journal of Green Energy. 2012;**9**:322-334

[85] Koffi PME, Andoh HY, Gbaha P, Toure S, Ado G. Theoretical and experimental study of solar water heater with internal exchanger using thermo siphon system. Energy Conversion and Management. 2008;**49**:2279-2290

[86] Jaisankar S, Radhakrishnan TK, Sheeba KN. Experimental studies on heat transfer and friction factor characteristics of thermosyphon solar water heater system fitted with spacer at the trailing edge of twisted tapes. Applied Thermal Engineering. 2009;**29**: 1224-1231

[87] Jaisankar S, Radhakrishnan TK, Sheeba KN. Experimental studies on heat transfer and friction factor characteristics of forced circulation solar water heater system fitted with helical twisted tapes. Solar Energy. 2009;**83**: 1943-1952

[88] Alshamaileh E. Testing of a new solar coating for solar water heating applications. Solar Energy. 2010;**84**: 1637-1643

[89] Kumar R, Rosen MA. Thermal performance of integrated collector-storage solar water heater with corrugated absorber surface. Applied Thermal Engineering. 2010;**30**: 1764-1768

[90] Salem Ahmed M, Mohamed R, Hady A, Abdallah G. Experimental investigation on the performance of chilled-water air conditioning unit using alumina nanofluids. Thermal Science and Engineering Progress. 2018;**5**: 589-596

[91] Xu G, Chen W, Deng S, Zhang X, Zhao S. Performance evaluation of a nano-fluid-based direct absorption solar collector with parabolic trough concentrator. Nanomaterials. 2015;**5**: 2131-2147

[92] Said Z, Sabiha MA, Saidur R, Hepbasli A, Rahim NA, Mekhilef S, et al. Performance enhancement of a flat plate solar collector using titanium dioxide nano-fluid and polyethylene glycol dispersant. Journal of Cleaner Production. 2015;**92**:343-353

[93] Polvongsri S, Kiatsiriroat T. Enhancement of flat-plate solar collector thermal performance with silver nano-fluid. In: The Second TSME International Conference on Mechanical Engineering; October 19–21, 2011

Chapter 5

Dynamic Viscosity of Graphene- and Ferrous Oxide-Based Nanofluids: Modeling and Experiment

Majid Al-Wadhahi, G. Reza Vakili-Nezhaad and Ohoud Al Ghafri

Abstract

This study focused on measuring the viscosity and analyzing the behavior of two types of nanofluids: ferrous oxide-deionized (DI) water nanofluids and graphene-DI water nanofluids at different temperatures and volume fractions. Zeta potential measurement, which was performed to check the stability of the nanofluids, showed stable suspensions. All viscosity measurements were conducted using a capillary viscometer at temperatures ranging between 25 and 65°C. Both types of nanofluids showed increasing viscosity with increasing nanoparticle loading and decreasing viscosity with increasing temperature. Furthermore, experiments on different-sized ferrous oxide-based nanofluids revealed inverse relation between the size of nanoparticles and viscosity. An accurate model was developed based on the Buckingham Pi theorem to fit all factors affecting viscosity in a dimensionless form. These factors are the viscosity of the base fluid, nanoparticles' volume fraction, nanoparticles' size, the temperature of the system, some molecular properties, and zeta potential.

Keywords: nanofluids, dynamic viscosity, Buckingham Pi theorem, correlation, zeta potential

1. Introduction

Nanofluids have found many applications in science and industry. Because of the very complex nature of such fluids, the prediction of their thermophysical properties has become a challenging problem for research. Among these properties, viscosity has a vital role in all nanofluids' transport phenomena. Therefore, a great deal of effort has been made in the last two decades for developing reliable models to predict the viscosity of nanofluids. Some studies on nanofluids' rheological behavior were devoted to understanding whether these fluids are Newtonian or non-Newtonian toward finding their viscosity based on the relation between the shear stress and the shear rate. However, in fact, there are many factors affecting viscosity of nanofluids, such as temperature, pH, volume fraction, particles' size, particle size distribution, electrical double layer (EDL), zeta potential, base fluid

type, aspect ratio of particles, packing coefficient, particles' agglomeration, nanolayers, and magnetic properties for ferromagnetic type of nanoparticles. In the following, the most recent well-known models for estimating the viscosity of nanofluids will be summarized. Their application for our experimental data set will be elaborated. Then, a summary of the experimental works in the literature followed by our experiments will be presented. Finally, we will discuss the newly developed model and its performance with regard to the generated data set in the present chapter.

2. Theoretical models on viscosity of nanofluids

Classical models have predated the invention of the nanofluids, and they were on the rheological behavior of micrometer- or millimeter-sized suspensions. Nanofluids are solid-liquid binary fluids; however, they are closer to the fluid state, unlike conventional fluid containing micrometer- or millimeter-sized particles. Therefore, most classical theoretical models such as those developed by Einstein, Smoluchowski, Booth, Ward and Whitmore, Vand, Moony, Roscoe, Brinkman, Williams, Krieger and Dougherty, Frankel and Acrivos, Farris, Nielsen, Lundgren, Batchelor, Kitano, Graham, and others are inconvenient to estimate the viscosity of nanofluids, and we are not going to review them. Since our focus here is only on the viscosity of nanofluids, we will just present those models that have been developed for nanofluids. Therefore, the models proposed by Chen, Masoumi, Hosseini, Selvakumar, Dhinakaran, and White are presented in the following in brief.

In 2007, Chen et al. [37] modified the work of Krieger and Dougherty. They assumed a suspension of polydisperse particles (different sized particles), containing agglomerates, and therefore they derived a new correlation by introducing maximum packing fraction of agglomerates (Φ_{ma}) and the fractal index of agglomerates. This model is given by Eq. (1) where Φ_a is given by ($\Phi_a = \Phi/\Phi_{ma}$). The viscosity was assumed to follow a power law with a fractal index (D). Thus, Φ_a becomes $\left[\Phi_a = \Phi(a_a/a)^{3-D}\right]$, where (a_a/a) is the ratio of effective radii of aggregates and primary nanoparticles.

$$\mu_{nf}/\mu_{bf} = \left(1 - \left(\frac{\Phi_a}{\Phi_m}\right)\right)^{-[\eta]\Phi_m} \tag{1}$$

In 2009, Masoumi et al. [39] developed a new semiempirical model, in which the effects of nanoparticle's density, Brownian motion, and some physical properties of the base fluid were considered. They analyzed the dispersion of nanoparticles in a fluid medium as a two-phase problem and considered five parameters affecting the viscosity of nanofluids, which are temperature, volume fraction, particles' size, nanoparticles' density, and the physical properties of the base fluid. Eqs. (2)–(4) show the proposed model with four empirical constants c_1, c_2, c_3, and c_4.

$$\mu_{nf} = \mu_0 + \frac{\rho_P v_B d_P^2}{72C\delta} \tag{2}$$

$$\delta = 3\sqrt{\frac{\pi}{6\phi}}\, d_p \tag{3}$$

$$C = \mu_0^{-1}\left[(c_1 dp + c_2)\phi + \left(c_3 d_p + c_4\right)\right] \tag{4}$$

In 2010, Hosseini et al. [38] proposed a new semiempirical dimensionless model for the viscosity of nanofluids. They formulated their equation of relative viscosity based on four dimensionless groups, which consider the effect of the viscosity of the base fluid, volume fraction of nanoparticles, size of the nanoparticles, thickness of the capping layer, and temperature on the viscosity of the nanofluid. This model is given by Eq. (5), in which, $\pi_1 = \frac{\mu_{nf}}{\mu_{nf}}$, $\pi_2 = \Phi_i$, $\pi_3 = \frac{d}{1+r}$, and $\pi_4 = \frac{T}{To}$.

$$\pi_1 = \exp\left(m + \omega\,\pi_2 + \gamma\,\pi_3 + \alpha\,\pi_4\right) \tag{5}$$

In 2017, Selvakumar and Dhinakaran made a modification on the proposed model by Chen et al. by introducing the term of interfacial layers surrounding the clusters [1]. This correlation is given as follows:

$$\mu_{nf}/\mu_{bf} = \left(1 - \left(\frac{\Phi_{ecl}}{\Phi_m}\right)\right)^{[\eta]\Phi_m} \tag{6}$$

$$\Phi_{ecl} = \Phi_{cl}(1+\beta) \tag{7}$$

where Φ_{ecl} is the effective volume fraction of the clusters with interfacial layers, and β is the ratio of the interfacial layer thickness to the average cluster radius.

3. Summary of experimental studies

Dependence of the viscosity of nanofluids on the nanoparticle loading is widely studied as mentioned in the previous section. The viscosity of nanofluids containing various types of nanoparticles like metals, oxides, and carbon nanotubes has been examined against nanoparticle concentration. Despite extensive experimental studies on the effect of nanoparticle loading on the viscosity of nanofluids, there is no universal equation that can predict this property with high accuracy [2]. Moreover, almost all investigations on the viscosity of nanofluids showed an increase in viscosity with increasing nanoparticle volume fraction [3]. This is noticed in all formerly mentioned nanofluids, except for carbon nanotube-based nanofluids that exhibit inverse relation between viscosity and particle loading. In addition, Nadooshan et al. [4] in their comprehensive study on the rheological behavior of nanofluids have concluded that most nanofluids display Newtonian behavior at low volume fractions and non-Newtonian behavior at high nanoparticle volume fractions. Furthermore, it has been proven that increasing volume fraction can lead to clustering of nanoparticles, and accordingly the viscosity of the fluid will rise. This increase in viscosity is due to the increase in surface-to-volume ratio during the aggregate formation. Duan et al. [5] investigated the effect of aggregation on the viscosity of Al2O3-water nanofluids and the results confirmed an increase in relative viscosity with the growth of cluster formation. Gaganpreet and Srivastava [6] also studied the effect of particle size, particle volume concentration, and concentration of particle aggregation on viscosity. The results revealed that nanofluid's volume fraction does not affect the viscosity directly, and increasing particle loading will result in aggregates. Therefore, viscosity increases as the size of aggregation increases [7].

In all studies on viscosity dependence of temperature in literature, an inverse relationship between viscosity and temperature has been observed, except for few works that show antithetical results such as Prasher et al. [8]. Investigations on the temperature effect on the viscosity of nanofluids have not reached a universal formula that describes viscosity behavior of such complex fluids as a function of

temperature. This might be due to the effect of other factors such as the type of base fluid, volume fraction, and particles' size on viscosity. Therefore, it was found that using the relative viscosity term (μnf/μbf) is more beneficial over using the viscosity in its absolute scale, which results in an easier understanding about the dependence of viscosity on temperature [2].

In all early cited studies, the relative viscosity was almost stable with temperature increase at low to moderate particle loading for nearly all nanofluid types, while at high nanoparticle concentrations, the relative viscosity starts to increase with increasing temperature. Few studies showed hysteresis in relative viscosity of nanofluids with temperature, where the relative viscosity started to increase and then decrease with increasing temperature. This behavior can be seen in the study done by Namburu et al. [9] for 29-nm CuO-(60:40) EG/water nanofluid. Other researchers concluded a reduction in relative viscosity with increasing temperature like the study of Li et al. [10] on ZnO-EG nanofluids. Investigations on the size effect of nanoparticles on the viscosity of nanofluids are few, and this can be referred to three reasons. The first reason is that measurements should be conducted, at the same time, for at least three nanoparticle sizes of the same type of nanofluids in the same base fluid. Secondly, the investigator should monitor with great attention particle distribution within the base fluid, and finally, perhaps many investigators have been frustrated by contradictory results on viscosity dependence on nanoparticles' size. Most studies on the influence of the size of nanoparticles showed a decrease in viscosity with increasing particle size. However, other studies have shown conflicting information. He et al.'s [11] and Nguyen et al.'s [12] studies showed a direct relation of viscosity with nanoparticles' size. Moreover, Nguyen et al. [12] have stated that at relatively low particle loading, nanoparticles' sizes have no virtual effect on the viscosity of nanofluids. Moreover, as nanoparticles' content increases, the effect of particles' size becomes significant and the higher viscosity will correspond to nanofluids of larger nanoparticle size. Prasher et al. [8], on the other hand, showed no significant effect on the viscosity of nanofluids by the size of nanoparticles. These discrepancies can be due to the variations in the production and measurement methods of various studies in the literature. Additionally, particle size range at each study is limited, and usually, two to three particle sizes are studied at a time that makes it difficult to evaluate the dependence of viscosity on particles' size. Furthermore, the addition of surfactants or other additives to nanofluids may affect the interpretation on particles' size dependence of viscosity, especially at high temperature where the interaction between nanoparticles and surfactant molecules is affected. The shape of nanoparticles is also an issue. If the particle sizes or diameters are the same but the shapes are different, such as spherical and rod-like, then viscosity and other properties will differ [13].

4. Experimental work

The viscosity of nanofluids is a function of many factors. Many researchers have considered a variety of such factors including type and size of the nanoparticle, compositional nature of the nanofluid mixture, as well as the temperature and pH of the mixture. The goal of this contribution is to examine and determine the effect of such variables on the dynamic viscosity of two types of nanofluids.

4.1 Selection of materials used

The fluids were purchased from the US Research Nanomaterials Company. This study focuses on the effect of particle size besides the effect of the nanoparticle

concentration and temperature. Therefore, the nanofluids used in this analysis were selected based on their particle size and type. Graphene-DI water dispersion was selected as a nonmetallic nanoparticle dispersion, and three ferrous oxide (Fe2O3)-DI water dispersions of different nanoparticle sizes were chosen as metallic oxide nanofluids. Graphene-DI water nanofluid has a weight fraction of 1%, a thickness between 0.55 and 1.2 nm, a diameter between 1 and 12 μm, specific surface area in the range of 500–1200 m^2/g, and a purity of 99.3%. The true density of the graphene was not provided by the supplier, and in this case, it was assumed to be 1 g/cm^3, for the sake of simplicity, as it has been found in the literature. Graphene is in sheet form of two-dimensional structures. It has excellent mechanical, thermal, and electrical properties. However, it is difficult to disperse graphene due to its large surface area. The US Research Nanomaterials Company labs are using a high-capacity ultrasonic equipment to disperse graphene in the specific dispersant, and the results show a very uniform and stable nanofluid. Three different particle sizes of ferrous oxide (Fe_2O_3) dispersed in DI water have been selected: 5, 10, and 30 nm. All iron oxides were dispersed in deionized water using a laser synthesizing method. Both 5- and 10-nm (Fe_2O_3)-DI water nanofluids have a weight fraction of 15 wt%, while 30-nm (Fe_2O_3)-DI water nanofluid has a weight fraction of 20 wt%. The purity of 5- and 10-nm nanofluids is 99.9%, whereas the 30-nm dispersion has a purity of 99.5%. The molar mass of nanoparticles is 159.69 g/mol and they have a true density of 5.24 g/cm^3. They are all spherical in shape. Five samples of graphene-DI water were prepared and they have volume fractions of 0.15, 0.45, 0.65, 0.85, and 1.00%. For iron oxide-DI water, the volume fractions were selected based on the stability of the diluted nanofluids and in a suitable range of volume fractions where other models of iron oxide nanofluid have been developed. The chosen volume concentrations for all three sets of Fe_2O_3-DI water were the same in order to examine the effect of particle size on viscosity. All prepared samples were ultrasonicated for around 2 hours at room temperature to ensure homogeneity and stability. Whenever these samples were kept for a long time, they were re-sonicated for 30 minutes to 1 hour prior to any measurement.

4.2 Zeta potential measurements

The second step was to take the readings of zeta potentials for all samples to confirm the stability of nanofluid samples. Zeta potential apparatus identifies the net charge on the nanoparticles, and accordingly gives an idea about the superficial properties of those particles in a suspension. The concept behind the zeta potential is that the ionized particles in a suspension are surrounded by two counter ion layers of the dispersant. The first film-like layer is called the Stern layer, while, the other loosely attached ions make up the diffusive ion layer, where ions' arrangement in this layer is affected by the thermal movements and electrical forces. As nanoparticles move in the dispersing fluid, the ions in the diffusive ion layer keep moving with the particle that they are associated to, separated from those ions in the liquid phase as if there is a boundary between them. This boundary is called the slipping plane. The difference in potentials between the slipping plane around those particles and fluid medium is the electrokinetic potential or in other words zeta potential ζ. When zeta potential value (ζ) between a point in the liquid phase and the slipping plane of particles is high (negative or positive), this will result in a high resistance of nanoparticles to agglomerate and vice versa. Therefore, zeta potential measurement is considered as an aid to identify the agglomeration of particles and, consequently, the stability of the nanofluid. Usually, when low zeta potential ($\pm\zeta$) of less than 25 mV is reported, this means the colloidal suspensions in the fluid tend to flocculate and thus the nanofluid is unstable. Zeta potential values ($\pm\zeta$) of

nanofluids between 30 and 40 mV are associated with a poorly stable suspension, while values ranging between 40 and 60 mV indicate good, stable suspensions, and those greater than 60 mV signify highly stable nanofluids. Hence, the zeta potential data have great advantages in commenting on the stability of the samples under study. Graphene-based nanofluids have an average zeta potential value ranging from 60 to 80, which is a signpost of excellent stability of the suspension. On the other hand, iron oxide samples showed fluctuating behavior. For instance, the average zeta potential value of 5 nm Fe_2O_3 in DI water is fluctuating in the approximate range of 70 to 290 mV. Overall, this indicates a highly stable 5-nm Fe_2O_3 nanofluid. The same thing is observed with the other two sets of Fe_2O_3-DI water. In the 10-nm Fe_2O_3-DI water system, the values of zeta potential are between 180 and 370 mV, while in the 30-nm Fe_2O_3-DI water system, there is a narrow range of potential between 270 and 350 mV. It is worth mentioning that the 30-nm Fe_2O_3-DI water nanofluid is highly stable, and the particles have no tendency to settle down even after a long time. However, in the 5-nm Fe_2O_3-DI water and 10-nm Fe_2O_3-DI water nanofluids, the nanoparticles lean toward settling down after a long time of around 1 hour after ultrasonication.

4.3 Viscosity measurements

The viscosity was measured by Cannon-Fenske capillary viscometer. The viscosity of the lowest and highest concentrations of graphene-based nanofluids was measured first to indicate the size of the capillary tube suitable for the rest of the measurements. The same step was repeated just with the Fe_2O_3 (size 5 nm) system. The viscosities of other ferrous oxide-based nanofluids were measured using the same capillary tube size. However, the Fe_2O_3 nanofluid of 30-nm particle size shows very low viscosity close to that of water. A thermostatic bath was used to regulate the surrounding temperature. The viscosity of all nanofluids was measured at temperatures of 25, 35, 45, 55, and 65°C. At each specific concentration and temperature, three readings of time which the fluid takes to flow from the upper mark to the lower mark of the capillary tube are taken. Viscosity measurement experiments have been conducted two times to check the results, and the averages of the two experiments have been calculated. The time is then converted to the kinematic viscosity by the following equation:

$$\nu = C \times t \tag{8}$$

where ν is the kinematic viscosity in (cSt), C is an approximate constant specified for each capillary viscometer in (cSt/s), and t is the time in (s). The kinematic viscosity can be defined as the ratio between the dynamic or absolute viscosity (μ) in (cp) and bulk density (ρ_{bulk}) in (g/cm^3) as stated in Eq. (9). The true density of all samples was provided by the US Research Nanomaterials Company, and it was 1 (g/cm^3) for all samples; therefore, kinematic viscosity and absolute viscosity are equal.

$$\nu = \frac{\mu}{\rho_{bulk}} \tag{9}$$

The results of the viscosity measurements are given in **Table 1**. The averages of the time of both experiments have been calculated, and the corresponding average viscosities at each volume fraction of nanoparticles and temperature are listed in **Table 1**. The standard deviation was also calculated for all viscosity readings of various samples at different temperatures using Eq. (10). For graphene-based

Nanofluid type (vol. %)	T (°C)	Experiment 1			Experiment 2			Average time (s)	Average viscosity (cp)
		Time readings (s)			Time readings (s)				
		1st	2nd	3rd	1st	2nd	3rd		
Graphene (0.15)	25	250.70	250.40	247.70	249.90	249.60	252.10	250.07	1.00
	35	201.80	204.73	205.08	207.80	205.93	205.78	205.18	0.82
	45	170.27	168.65	168.87	170.67	171.75	172.13	170.39	0.68
	55	143.77	143.28	142.30	146.37	148.73	147.70	145.36	0.58
	65	122.90	123.27	123.03	128.43	127.93	129.23	125.80	0.50
Graphene (0.45)	25	318.63	318.80	319.63	325.43	324.60	321.97	321.51	1.29
	35	260.00	258.41	258.90	260.93	260.85	261.23	260.06	1.04
	45	214.35	214.55	213.15	216.79	218.05	217.25	215.69	0.86
	55	181.30	182.73	182.53	183.49	183.93	182.93	182.82	0.73
	65	157.37	156.93	157.71	157.97	158.33	158.81	157.85	0.63
Graphene (0.65)	25	389.06	388.90	388.92	390.34	388.90	389.29	389.23	1.56
	35	313.48	314.35	315.70	313.73	314.71	316.16	314.68	1.26
	45	257.70	259.60	260.38	258.60	260.90	261.12	259.72	1.04
	55	217.63	217.77	218.39	219.67	218.49	219.11	218.51	0.87
	65	186.59	187.60	188.20	187.57	196.00	189.50	189.24	0.76
Graphene (0.85)	25	442.90	445.70	444.00	444.10	452.60	444.60	445.65	1.78
	35	357.95	357.38	358.08	359.25	357.13	356.28	357.68	1.43
	45	298.70	294.46	293.01	298.36	294.94	293.39	295.48	1.18
	55	249.57	245.32	250.05	249.58	245.48	248.85	248.14	0.99
	65	210.28	214.00	212.93	210.58	220.20	217.53	214.25	0.86
Graphene (1.00)	25	518.03	512.88	511.70	512.77	513.92	507.50	512.80	2.05
	35	415.14	414.23	414.85	415.56	416.73	410.95	414.58	1.66
	45	341.68	341.43	339.68	342.98	342.93	341.52	341.70	1.37
	55	287.22	289.43	287.92	286.98	288.67	286.58	287.80	1.15
	65	245.26	246.22	247.53	246.26	246.58	247.78	246.60	0.99
5-nm Fe_2O_3 (0.19)	25	345.70	348.28	360.18	343.06	337.00	405.38	356.60	1.43
	35	284.68	299.64	283.23	291.88	317.24	272.25	291.49	1.17
	45	233.60	230.72	235.91	222.32	234.28	241.01	232.97	0.93
	55	195.90	187.19	194.77	199.06	187.97	207.57	195.41	0.78
	65	158.00	158.98	170.48	165.88	164.86	165.80	164.00	0.66
5-nm Fe_2O_3 (0.29)	25	418.19	417.38	411.18	410.85	423.66	418.26	416.59	1.67
	35	328.32	350.46	383.52	339.52	334.86	337.92	345.77	1.38
	45	259.23	263.60	268.28	267.43	264.10	287.62	268.38	1.07
	55	222.13	218.10	223.89	228.17	224.23	231.01	224.59	0.90
	65	188.43	187.20	174.10	180.30	203.33	178.90	185.38	0.74
5-nm Fe_2O_3 (0.38)	25	523.26	523.85	522.28	529.10	512.59	526.35	522.91	2.09
	35	406.90	403.15	406.09	407.57	407.28	409.11	406.68	1.63
	45	322.94	318.47	320.18	318.79	316.60	316.25	318.87	1.28

Nanofluid type (vol. %)	T (°C)	Experiment 1			Experiment 2			Average time (s)	Average viscosity (cp)
		Time readings (s)			Time readings (s)				
		1st	2nd	3rd	1st	2nd	3rd		
	55	259.10	258.05	260.15	264.30	259.78	263.68	260.84	1.04
	65	217.54	217.55	216.57	213.46	210.19	213.77	214.84	0.86
5-nm Fe_2O_3 (0.48)	25	618.98	610.76	628.52	653.46	611.01	616.80	623.25	2.49
	35	467.39	474.10	476.73	476.51	477.00	479.23	475.16	1.90
	45	361.17	364.45	359.74	368.33	367.12	363.13	363.99	1.46
	55	282.21	294.03	282.59	285.49	282.61	277.41	284.06	1.14
	65	232.76	232.05	235.66	235.45	240.95	239.01	235.98	0.94
5-nm Fe_2O_3 (0.57)	25	771.14	774.59	772.17	773.82	770.81	767.10	771.60	3.09
	35	582.45	579.27	579.10	579.35	583.06	583.37	581.10	2.32
	45	430.28	433.95	432.11	432.92	437.02	393.79	426.68	1.71
	55	323.19	328.32	342.19	327.17	323.21	325.26	328.22	1.31
	65	269.22	271.84	272.04	276.15	273.60	258.92	270.29	1.08
10-nm Fe_2O_3 (0.19)	25	345.13	344.75	347.30	348.41	340.22	343.93	344.96	1.38
	35	281.63	281.65	276.83	308.73	274.35	274.20	282.90	1.13
	45	222.12	229.38	218.33	220.75	221.66	223.64	222.64	0.89
	55	190.41	191.77	192.49	189.12	192.06	193.14	191.50	0.77
	65	162.82	162.24	162.48	168.11	160.87	162.53	163.17	0.65
10-nm Fe_2O_3 (0.29)	25	409.43	406.30	408.83	410.54	408.27	407.91	408.54	1.63
	35	320.74	323.84	322.78	323.86	323.39	321.09	322.62	1.29
	45	254.38	258.13	259.79	255.49	251.67	255.28	255.79	1.02
	55	215.02	212.51	215.74	215.32	215.60	216.19	215.06	0.86
	65	180.16	180.20	178.89	181.24	185.30	182.34	181.36	0.73
10-nm Fe_2O_3 (0.38)	25	496.91	492.59	503.65	500.00	499.88	500.08	498.85	2.00
	35	390.19	391.83	392.82	393.28	386.54	393.11	391.29	1.57
	45	299.54	303.98	304.68	302.39	307.65	305.79	304.01	1.22
	55	244.85	244.55	249.01	252.55	241.54	249.36	246.98	0.99
	65	203.05	205.77	204.25	206.08	210.04	203.75	205.49	0.82
10-nm Fe_2O_3 (0.48)	25	575.27	615.91	604.10	598.38	621.24	597.00	601.98	2.41
	35	464.59	466.14	469.81	466.91	472.86	459.29	466.60	1.87
	45	353.15	359.48	354.52	358.46	360.12	356.03	356.96	1.43
	55	289.79	285.09	286.16	287.48	280.81	279.59	284.82	1.14
	65	236.61	237.00	234.25	235.54	237.90	236.55	236.31	0.95
10-nm Fe_2O_3 (0.57)	25	714.30	739.84	741.41	736.81	738.13	736.70	734.53	2.94
	35	548.79	548.98	548.72	549.32	548.28	549.01	548.85	2.20
	45	417.09	417.19	415.47	420.88	414.61	416.73	416.99	1.67
	55	320.33	324.88	328.10	321.04	319.04	325.37	323.13	1.29
	65	263.47	265.29	266.99	263.94	262.78	268.38	265.14	1.06
30-nm Fe_2O_3 (0.19)	25	233.03	232.60	233.46	232.50	232.30	232.47	232.73	0.93
	35	188.83	191.92	188.56	189.30	189.38	192.54	190.09	0.76

Nanofluid type (vol. %)	T (°C)	Experiment 1			Experiment 2			Average time (s)	Average viscosity (cp)
		Time readings (s)			Time readings (s)				
		1st	2nd	3rd	1st	2nd	3rd		
	45	158.42	160.94	157.05	158.71	156.22	159.62	158.49	0.63
	55	134.85	136.83	133.57	134.41	129.54	135.61	134.14	0.54
	65	114.80	118.47	116.95	117.53	117.50	115.71	116.83	0.47
30-nm Fe_2O_3 (0.29)	25	239.86	240.99	237.05	237.14	235.48	238.95	238.24	0.95
	35	191.74	193.20	194.00	195.66	195.17	195.56	194.22	0.78
	45	159.97	161.56	163.00	161.27	162.08	160.21	161.34	0.65
	55	137.24	135.68	137.24	137.83	139.32	136.73	137.34	0.55
	65	116.79	118.32	119.46	121.47	120.62	117.61	119.04	0.48
30-nm Fe_2O_3 (0.38)	25	245.77	247.34	244.72	248.23	247.53	245.35	246.49	0.99
	35	201.66	201.49	200.33	201.71	201.84	202.34	201.56	0.81
	45	164.51	165.07	166.13	165.14	167.18	166.17	165.70	0.66
	55	138.33	140.10	140.10	140.20	140.15	139.23	139.69	0.56
	65	120.95	121.65	121.04	121.15	123.68	121.61	121.68	0.49
30-nm Fe_2O_3 (0.48)	25	250.77	249.20	248.87	251.23	253.13	250.76	250.66	1.00
	35	206.93	207.65	207.57	207.73	207.68	206.93	207.42	0.83
	45	169.64	172.08	172.22	171.70	169.83	172.13	171.26	0.69
	55	142.51	141.89	143.99	143.24	144.36	144.07	143.34	0.57
	65	124.18	121.90	125.60	124.48	125.25	125.73	124.53	0.50
30-nm Fe_2O_3 (0.57)	25	258.38	259.87	258.61	259.09	260.06	258.49	259.08	1.04
	35	211.78	211.84	211.60	212.15	212.49	211.27	211.86	0.85
	45	175.71	174.29	174.04	176.14	175.46	175.86	175.25	0.70
	55	147.61	145.43	145.85	148.32	146.82	146.41	146.74	0.59
	65	128.39	127.24	126.91	129.12	126.87	128.04	127.76	0.51

Table 1.
Viscosity measurements for all nanofluid samples.

nanofluids, the average standard deviation was 1.88, while for iron oxide-based nanofluids, it was 4.22.

$$s = \sqrt{\frac{\sum_{i=1}^{N}(x_i - \overline{x})^2}{N-1}} \tag{10}$$

As shown in **Figure 1**, five graphene-based nanofluids at different concentrations (0.15, 0.45, 0.65, 0.85, and 1.00%) were tested under five different temperatures, which are 25, 35, 45, 55, and 65°C. It can be observed that as the temperature increases, the viscosity declines. Moreover, the viscosity rises with the increasing concentration. Since the stepwise increase between concentrations is the same, it can be seen that the gradual increase in viscosity is almost equal between any concentration and the one above. **Figures 2–4** present viscosity measurements for the iron oxide-based nanofluids for the particle sizes of 5, 10, and 30 nm,

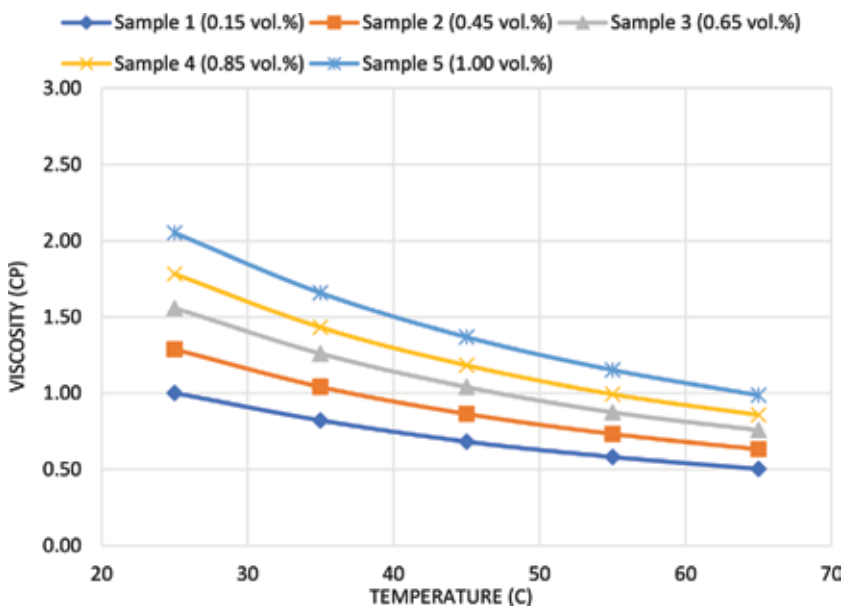

Figure 1.
Viscosity measurements of graphene samples.

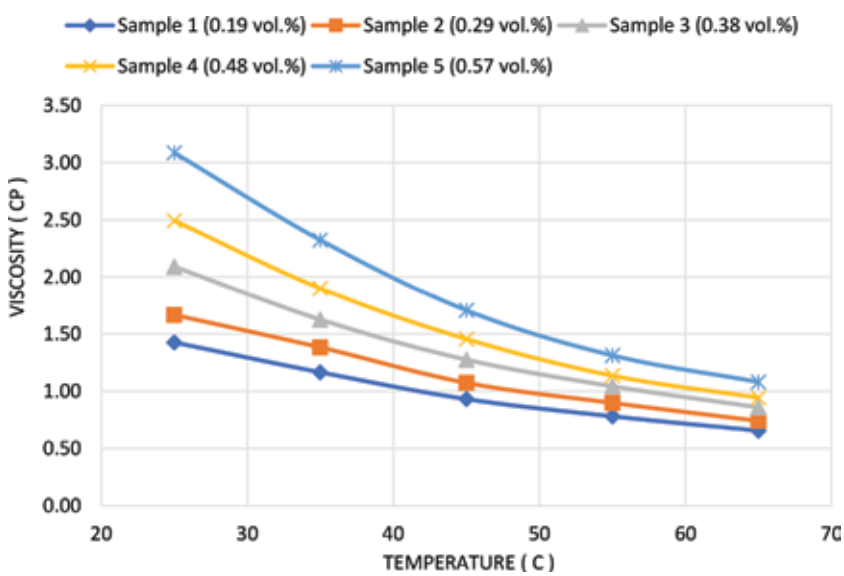

Figure 2.
Viscosity measurements of 5-nm Fe_2O_3-based nanofluid.

respectively. It is observed that the viscosity increases with the increase of concentration and with the decrease in temperature. It is also noticed that there is a slight increase in the viscosities of 5-nm Fe_2O_3 nanofluid compared with 10-nm Fe_2O_3 nanofluid.

It is observed that the viscosity increases with the increase of concentration and with decrease in temperature. Furthermore, it is observed that there is a gradual increase in the difference between any two lines, knowing that the stepwise increase in the concentration is even, at the same temperature for a given nanofluid. In many studies on the effect of nanoparticle size on the viscosity of a fluid, it was found that at very low volume fractions, the effect of particle size is not significant,

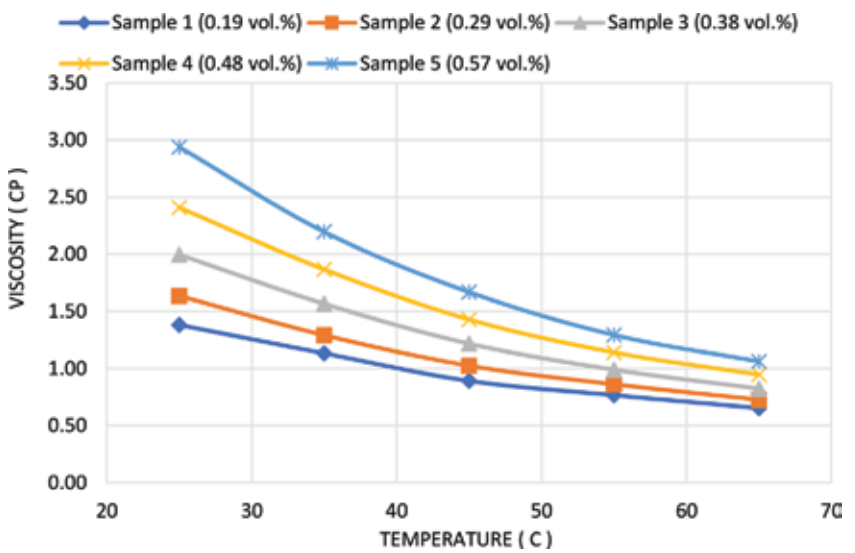

Figure 3.
Viscosity measurements of 10-nm Fe_2O_3-based nanofluid.

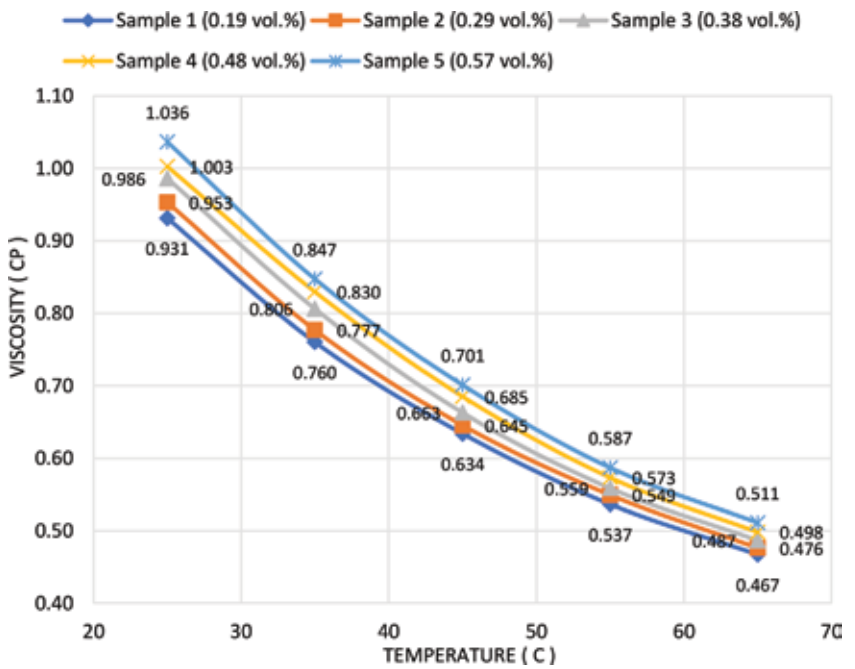

Figure 4.
Viscosity measurements of 30-nm Fe_2O_3-based nanofluid.

and at higher volume concentrations, the effect becomes more obvious. For example, when two aluminum oxide water nanofluids have a different particle size of 36 and 47 nm, and the same volume fraction of less than 4 vol%, the measured viscosities of both are virtually equal. But when the volume fraction has increased beyond 4 vol%, the viscosity of 36-nm Al_2O_3-water nanofluid is much higher than that of 47-nm Al_2O_3-water nanofluid. Few studies have been carried out to see the effect of particle size on the viscosity of nanofluids. Some of them concluded a reduction in viscosity with decreasing particle size like for the system of TiO_2-water

nanofluids with relatively large particle size (95, 132, and 230 nm) and low concentrations of less than 1.2 vol%. Many other studies have found an inverse relation between nanoparticle size and viscosity of nanofluid such as Namburu et al.'s study on aluminum oxide ethylene glycol-based nanofluid, Rudyak's experimental research on silicon oxide water-based nanofluids, and molecular dynamics simulations of Vakili-Nezhaad et al. [40, 41]. Until now, there has been no distinct explanation for this behavior of nanofluids.

5. Modeling and analysis

5.1 Calculating viscosity of nanofluids using models from literature

Since there are few models on the effect of nanoparticle size on viscosity along with the temperature and volume concentration factors, four models have been selected to reproduce the relative viscosity of graphene and ferrous oxide-based nanofluids. Three of them predict viscosity as a function of temperature, volume fraction, and size of nanoparticles. These models have been selected based on their specifications of nanoparticle material, base fluid, temperature range, and volume fraction. All chosen equations consider nonmetallic or metal oxide nanoparticles, which are dispersed in water at low volume fractions of less than 9 vol%, and viscosity is measured at temperatures ranging between 20 and 90°C. Average absolute deviations were calculated by Eq. (11) to comment on and verify the accuracy of the models.

$$AAD\% = \frac{1}{n}\left\{\sum_{i=1}^{n}\left|\frac{\left((\mu_r)_{exp} - (\mu_r)_{prd}\right)}{(\mu_r)_{exp}} \times 100\right|\right\} \tag{11}$$

The first model is that of Azmi et al. [14]. They have proposed Eq. (12) for the viscosity of Al_2O_3 and CuO nanoparticle in water as base fluid. Here, μ_{nf} and μ_w are the viscosity of nanofluid and water in cp, T_{nf} and T_w are temperatures of nanofluid and water in °C, Φ_p is the volume fraction of nanoparticles, and d_p is nanoparticles' size in nm.

$$\mu_{nf} = \mu_w\left(1 + \frac{\Phi}{100}\right)^{11.3}\left(1 + \frac{T_{nf}}{70}\right)^{-0.038}\left(1 + \frac{d_p}{170}\right)^{-0.061} \tag{12}$$

$$\mu_w = 0.00169 - 4.25263e-5 \times T_w + 4.9255e-7 \times (T_w)^2 - 2.09935e-9 \times (T_w)^3 \tag{13}$$

In this model, experimental results are taken from the works of Wang et al. [15], Pak and Cho [16], Zeinali Heris et al. [17], Nguyen et al. [12], He et al., (2007), Nguyen et al. [18], Lee et al. [19], Hwang et al. [20], Duangthongsuk and Wongwises [21], and Lee et al. [22] to build a new nonlinear regression equation. In these experimental works, the particles' sizes of aluminum oxide are 36 and 47 nm, while the particle size of copper oxide is 29 nm. All volume fractions that have been investigated are less than 4%, and viscosity was measured at ambient temperature. Eq. (12) has shown an average absolute deviation of 2.89% for calculating the viscosity of Al_2O_3 and CuO nanoparticles in water as base fluid. However, when it was used to calculate the viscosity of all ferrous oxide nanoparticles, the average absolute deviation (AAD%) was 38.48%. Moreover, it was observed that the lowest AAD% was that calculated for 30-nm Fe_2O_3-based nanofluids in water, where the particle size of this nanofluid is close to that of Al_2O_3-water and CuO-water

nanofluids used to generate this model. For graphene, the average absolute deviation (AAD%) between the experimental data and estimated viscosity using Eq. (12) was 41.02%. The second model is proposed by Khanafer and Vafai [23], and given by Eq. (14), where μ_{eff} is the dynamic viscosity of nanofluid in mPa.s (1 cp = 1 mPa.s), T is the temperature in °C, Φ_p is the volume fraction of nanoparticles, and d_p is nanoparticles' size in nm.

$$\mu_{eff} = -0.4491 + \frac{28.837}{T} + 0.574\Phi_p - 0.1634\Phi_p^2 + 23.053\frac{\Phi_p^2}{T^2} + 0.0132\Phi_p^3 - 2354.735\frac{\Phi_p}{T^3} + 23.498\frac{\Phi_p}{d_p^2} - 3.0185\frac{\Phi_p^3}{d_p^2} \tag{14}$$

This equation estimates the viscosity of various Al_2O_3-water nanofluids with volume fractions between 1 and 9% with particle size ranges from 13 to 131 nm, and at temperatures between 20 and 70°C. This equation was developed using various viscosity data of Al_2O_3-water in the literature which are presented in Keblinski et al. [24], Putra et al. [25], Nguyen et al. [12], and Anoop et al. [26]. Khanafer and Vafai [23] have stated that their regression equation shows a correlation coefficient of (R^2) of 99% for all experimental data of Al_2O_3-water nanofluids. When Khanafer and Vafai's [23] model was used to find the viscosity of all Fe_2O_3-deionized water nanofluids of our work at different conditions of temperatures and volume fractions, a 78.10% average absolute deviation (AAD%) was observed. For our graphene-based nanofluids, the AAD% was 77.74%. In both cases, the error was too high.

The model proposed by Sekhar and Sharma [27] is the third model used to predict the viscosity of the nanofluids of this study, and their correlation is shown in Eq. (15) below, where μ_r is the relative viscosity of the nanofluid to its base fluid, Φ is the volume fraction of nanoparticles, T_{nf} is the temperature in °C, and d_p is nanoparticles' size in nm.

$$\mu_r = 0.935\left(1 + \frac{T_{nf}}{70}\right)^{0.5602}\left(1 + \frac{d_p}{80}\right)^{-0.05915}\left(1 + \frac{\Phi}{100}\right)^{10.51} \tag{15}$$

Sekhar and Sharma referred to experimental measurements of Al_2O_3-water nanofluids' viscosity in literature, to cover diverse particle sizes, volume fractions, and temperatures. They have considered experimental data for viscosity of Al_2O_3-water nanofluids from studies of Pak and Cho [16], Das et al. [28], Prasher et al. [8], Jang et al. [29], Timofeeva et al. [30], Lee et al. [19], Williams et al. [31], Nguyen et al. [18], Tavman et al. [32], Anoop et al. [26], Chandrasekar et al. [33], Duan et al. [5], and Murshed [34] along with their measurements to develop Eq. (15). Therefore, this equation can predict the viscosity of Al_2O_3-water nanofluids of 13–100 nm particle size and volume fraction ranges between 0.01 and 5%, at temperature ranges from 20 to 70°C. This model has an average absolute deviation of 9% with all Al_2O_3-water nanofluids' experimental data of viscosity. Regarding our experimental data, a large deviation (AAD%) of 29.32 and 23.43% was shown when the viscosity of Fe_2O_3-deionized water and graphene-deionized water nanofluids was calculated using Eq. (15), respectively. The deviation between the calculated viscosity and the experimental results was the lowest for 30-nm Fe_2O_3-deionized water nanofluids (average 12.93%), while in other nanofluids the error was much higher.

The fourth examined model is the model developed by Ahammed et al. [35] for graphene-water-based nanofluids of 1–5-nm particle thickness. This model is presented in Eq. (16). It is obvious that this equation of relative viscosity is a

Model	5-nm Fe_2O_3-DI water	10-nm Fe_2O_3-DI water	30-nm Fe_2O_3-DI water	All Fe_2O_3-DI water nanofluids	0.875-nm graphene-DI water
Azmi et al. [14]	52.12	51.15	11.51	38.48	41.02
Khanafer and Vafai [23]	82.24	82.95	67.76	78.10	77.74
Sekhar and Sharma [27]	37.97	36.64	12.93	29.32	23.43
Ahammed et al. [35]	18.43	16.67	52.73	29.50	13.91

Table 2.
Average absolute deviations (%) between measured relative viscosities and estimated relative viscosities using different models for all Fe_2O_3- and graphene-based nanofluids in the present study.

function of two variables: temperature and volume fraction. T_∞ and T are the ambient temperature and nanofluid temperature in °C, respectively, and Φ is the volume fraction.

$$\frac{\mu_{nf}}{\mu_{bf}} = 4.682\left(\frac{T_\infty}{T}\right)^{0.00049}\Phi^{0.1794} \tag{16}$$

In this model, measurement of the viscosity was for three different volume fractions of graphene: 0.05, 0.1, and 0.15%, at nine temperatures between 10 and 90°C. The measured viscosities have an average absolute deviation of 2% with the calculated viscosities by Eq. (16). Eq. (16) has been used in this research to predict the viscosities of all graphene and ferrous oxide-based nanofluids. The correlation predicts the viscosity of the graphene-based nanofluids and all Fe_2O_3-deionized water nanofluids with the AAD% of 13.91 and 29.5%, respectively. It is also noticed that Eq. (16) represents the viscosity of 5- and 10-nm Fe_2O_3-deionized water nanofluids better than its prediction for the viscosity of 30-nm Fe_2O_3-deionized water nanofluids. Furthermore, it was expected that this equation will give better predictions of graphene-DI water nanofluid of our study; however, the deviation somehow was high (13.91%). **Table 2** shows the average absolute deviation (AAD%) between the predicted viscosities by all four models and our experimental data of all graphene and ferrous oxide water-based nanofluids.

5.2 Development of a new model for the viscosity of nanofluids

In this section, we aim to develop a new correlation for calculation of the viscosity of our nanofluids with higher accuracy compared to the models available in the literature. The model was developed based on Vaschy-Buckingham theorem or dimensionless analysis theorem, which will be elaborated here in brief. In Vaschy-Buckingham theorem or dimensionless analysis theorem, any equation that describes a physical phenomenon includes a number of (n) variables that can be rewritten as (n–k) independent dimensionless coefficients (π), where (n) is all physical quantities that are related or have effect on any physical phenomenon and k corresponds to the number of base quantities or fundamental dimensions such as dimensions of mass, length, and time for the mechanical system. In 1914, Buckingham [36] stated that any physical equation of different kinds of physical quantities can be written in the following form,

$$f(Q_1, Q_2, Q_3, ...Q_n) = 0 \tag{17}$$

If the physical equation contains some several quantities of any kind, the equation will be in form (18), in which r', r''.... etc. are the ratios of each one of these quantities to a chosen quantity of the same kind.

$$f(Q_1, Q_2, Q_3, ...Q_n, r', r''...) = 0 \tag{18}$$

At this stage, let us focus on the form (18), assuming that there are no several quantities of the same kind. Every complete physical equation has the form (19).

$$\sum M\, Q_1{}^{b_1} Q_2{}^{b_2} .....Q_{\mathrm{n}}{}^{b_n} = 0 \tag{19}$$

According to the dimensional homogeneity's principle of Fourier, any physical equation must be homogenous in dimensions, which means each term in the equation must have the same dimension. This can be done through dividing Eq. (19) by any term; thus, the resulting equation will be in the form (20), where Ns are dimensionless numbers, and $a_1, a_2...a_n$ are exponents that make all terms dimensionless (i.e., $a_1 + a_2 + ... + a_n = 0$)

$$\sum N\, Q_1{}^{a_1} Q_2{}^{a_2} .....Q_{\mathrm{n}}{}^{a_n} + 1 = 0 \tag{20}$$

Now, if

$$\pi = Q_1{}^{a_1} Q_2{}^{a_2} ....Q_{\mathrm{n}}{}^{a_n} \tag{21}$$

then, Eq. (20) will be in the form of Eq. (22)

$$\sum N\, \pi + 1 = 0 \tag{22}$$

Since π is dimensionless, the product of all $\pi's$, let say, $\pi_1{}^{x_1} \pi_2{}^{x_2} ....\pi_{\mathrm{i}}{}^{x_n}$, will also be dimensionless. In other words, each π is, now, an independent dimensionless product of quantities Q in Eq. (21); hence, Eq. (22) can be rewritten in the form (23) and (24). Note that up to this stage Fourier principle is still satisfied. Moreover, according to Eq. (20) and (21), every π term equals 1 (i.e., $[\pi_1] = [\pi_2] = [\pi_3] = ... = [\pi_i] = [1], and\ \sum_{j=1}^{n}(x_j) = 0$).

$$\sum N\, \pi_1{}^{x_1} \pi_2{}^{x_2} ....\pi_{\mathrm{i}}{}^{x_n} + 1 = 0 \tag{23}$$

$$\psi(\pi_1, \pi_2, \pi_3, ...\pi_i) = 0 \tag{24}$$

The aim of the previous steps is to convert Eqs. (17)–(24) by combining different Q variables in various ways into dimensionless terms. After that, Buckingham gave a restriction for the maximum number of dimensionless terms (i). Buckingham assumed that k is the number of the fundamental dimensions, n is the number of quantities (Qs) that can be derived from the base quantities, and, thus, i equals (n–k).

$$\left\{ \begin{array}{r} [\pi_1] = \left[Q_1{}^{\alpha_1} Q_2{}^{\beta_1} ...Q_{\mathrm{k}}{}^{\gamma_1} P_1\right] = [1] \\ [\pi_2] = \left[Q_1{}^{\alpha_2} Q_2{}^{\beta_2} ...Q_{\mathrm{k}}{}^{\gamma_2} P_2\right] = [1] \\ ..... \\ [\pi_{\mathrm{i}}] = \left[Q_1{}^{\alpha_i} Q_2{}^{\beta_i} ...Q_{\mathrm{k}}{}^{\gamma_i} P_i\right] = [1] \end{array} \right\} \tag{25}$$

Eq. (25) shows the form of independent dimensionless terms of a physical phenomenon. In order to get each dimensionless term, take k number of different kind quantities and let them be Q_1 to Q_k in all π equations. Then each remaining (n-k) of different kind quantities to be the ($P's$) terms in each π equation. $Q's$ are chosen such that they contain all base dimensions like mass, length, and time. Furthermore, it should be noted that those dimensions are not built on the size of the base quantities (fundamental dimensions). They are just dependent on the interrelation between them. Additionally, choosing different combinations of different kind quantities to be Q_1 to Q_k will result in a different structure of Eq. (24). In this study, it was assumed that the viscosity of a nanofluid is affected by the viscosity of the base fluid, particles' concentration, nanoparticles' diameter, particles' diameter of the base fluid, kinetic or thermal energy due to temperature (T), and interaction between particles through zeta potential (ζ), and electron charge (e) as stated in Eq. (26). Boltzmann's constant is considered to be the average kinetic energy of a particle due to the increase in temperature by 1 K. Although, both electron charge (e) and Boltzmann's constant (k) are constants, they are not dimensionless; thus, according to the Buckingham theorem, they are physical quantities that can be measured and derived from other quantities. Therefore, they appear in the following equation as two quantities.

$$f\left(\mu_{nf}, \mu_{bf}, \Phi, d_p, d_o, T, k, e, \zeta\right) = 0 \tag{26}$$

μ_{nf} and μ_{bf} are the viscosities of the nanofluids and water in cp, T is nanofluids' temperature in K; Φ is the volume fraction; d_p is nanoparticles' size in nm; d_o is the diameter of water molecule which is 0.275 nm; e is the electron charge which is 1.60218×10^{-19} C; ζ is the zeta potential in V; and k is the Boltzmann constant, $1.38066 \times 10^{-23} J/K$. In this model, prediction of viscosity was enhanced by including a term, which consists of two factors, kT and $e\zeta$. A closer look at Eq. (26) reveals that we have seven different kinds of quantities. Since μ_{nf} and μ_{bf} are of the same kind, and d_p and d_o are also of the same kind; then, Eq. (26) will be in the form of Eq. (27). Consequently, the physical equation has (n) different kinds of quantities (n = 7), where three of them are dimensionless ratios (i.e., $r' = \Phi, r'' = \frac{\mu_{nf}}{\mu_{bf}}, r''' = \frac{d_p}{d_o}$). The number of fundamental dimensions (k) is 5; these are mass (M), time (T), length (L), temperature (Θ), and electrical current (I).

$$f\left(Q_1, Q_2, Q_3, Q_4, r', r'', r'''\right) = f\left(T, k, e, \zeta, \Phi, \frac{\mu_{nf}}{\mu_{bf}}, \frac{d_p}{d_o}\right) = 0 \tag{27}$$

Eventually, based on the mentioned theory, the following form of function φ in Eq. (28) was obtained, in which all constants C_0, C_1, C_2, and C_3 are empirical constants to be obtained by nonlinear regression analysis using experimental data set.

$$\frac{\mu_{nf}}{\mu_{bf}} = C_0 \Phi^{C_1} \left(\frac{d_p}{d_o}\right)^{C_2} \exp\left(\frac{C_3 e\zeta}{kT}\right) \tag{28}$$

Microsoft Excel was used to list all independent and dependent variables and all data of trials to get the best fit's coefficients, while MATLAB was used to import the data from Excel and find the best regression coefficient in each trial. Changing initial values, repeating trials, and calculating the average absolute deviation

between the expected and the predicted relative viscosity were repetitive processes used to get the best nonlinear regression model for the viscosity of nanofluids. The optimized parameters of C_0, C_1, C_2, and C_3 which provide the best fit are tabulated in **Table 3** for both graphene- and Fe_2O_3-based nanofluids.

An average absolute deviation of 13.74% between the calculated relative viscosities by the new model and the experimental data for all iron oxide-based nanofluids was obtained. For graphene-based nanofluids, it was 5.82%. It is obvious that this model reduces the deviation for all types of nanofluids since it includes the nanoparticle's size effect besides the effect of kinetic and potential energies between nanoparticles. **Table 4** shows the overall average absolute deviations (AAD%) for all models from the literature and the new developed model in this research. It shows enhancement in estimating the viscosity of nanofluids by the new model.

A comparison between experimental data and calculated values by different models for graphene-based nanofluids was made. It was observed that most of the points calculated by the new model were in the range of −5 to +5% deviation from the experimental data resulting in an average absolute deviation of 5.82%. For the model proposed by Ahammed et al. [35], the calculated points are spread over a range of deviation from −10% and higher than +20%, resulting in an average absolute deviation of 13.91%. For the models of Sekhar and Sharma [27], Azmi et al. [14], and Khanafer and Vafai [23], most of the calculated points have deviations' ranges lower than −20%. The average absolute deviations of those models are 23.43, 41.02, and 77.74% respectively, and they underestimate the viscosity of graphene-based nanofluids. A similar comparison was made between the experimental data and calculated values by different models for Fe_2O_3-based nanofluids. It was noticed that most of the points of the new model are widely spread over the range of −20 to +20% deviations which finally gives an average absolute deviation of 13.74%. The model proposed by Ahammed et al. [35]

Constant	All Fe_2O_3-DI water nanofluids	Graphene-DI water nanofluids
C_0	191.791451	3.384594
C_1	0.590026	0.342364
C_2	−0.414975	0.674537
C_3	0.0165741	0.117727

Table 3.
Values of constants for the proposed new model.

Model	All Fe_2O_3-DI water nanofluids	Graphene-DI water nanofluids
Semi-empirical model (present work)	13.74%	5.82%
Ahammed et al. [35]	29.50%	13.91%
Sekhar and Sharma [27]	29.32%	23.43%
Azmi et al. [14]	38.48%	41.02%
Khanafer and Vafai [23]	78.10%	77.74%

Table 4.
Average absolute deviations between measured relative viscosities and predicted relative viscosities using different models for all Fe_2O_3- and graphene-based nanofluids.

underestimates the relative viscosity of 5- and 10-nm-sized Fe2O3-based nanofluids, while it overestimates the relative viscosity of 30-nm Fe_2O_3-based nanofluids. Most data points for this model are in the range from 1% to over 30% deviations, which resulted in an average absolute deviation of 29.50%. For models of Sekhar and Sharma [27], Azmi et al. [14], and Khanafer and Vafai [23], most of the points were found to lie on the ranges lower than −20% deviations, which resulted in the average absolute deviations of 29.32, 38.48, and 78.10%, respectively. The models proposed by Azmi et al. [14] and Khanafer and Vafai [23] underestimate the relative viscosities of all Fe_2O_3-based nanofluids, while the model of Sekhar and Sharma [27] overestimates the relative viscosity of 30-nm Fe_2O_3-based nanofluids. The model proposed by Sekhar and Sharma [27] underestimates the relative viscosity of 5- and 10-nm Fe_2O_3-based nanofluids.

6. Conclusions

This study focused on measuring the viscosity and analyzing the behavior of two types of nanofluids: ferrous oxide-DI water nanofluids (three sizes) and graphene-DI water nanofluids. The viscosity of graphene-based nanofluids was measured at different volume fractions of 0.15, 0.45, 0.65, 0.85, and 1.00%. We measured the viscosities of three different sizes of ferrous oxide-based nanofluids at volume fractions of 0.19, 0.29, 0.38, 0.48, and 0.57%. Zeta potential measurement was performed to check the stability of nanofluids, and all zeta potential values were above 60 mV, which indicates stabled suspensions. All viscosity measurements were conducted using capillary viscometer at temperatures ranging between 25 and 65°C. Both types of nanofluids showed increasing viscosity with increasing nanoparticle loading, and decreasing viscosity with increasing temperatures. Furthermore, testing ferrous oxide-based nanofluids of different sizes revealed an inverse relation between the size of nanoparticles and viscosity. A total of 100 data points were generated and compared with the calculated values using the most relevant models available in the literature. All those models showed relatively high deviations from measured viscosities. Therefore, similar to other researches in this field, we developed a new model for the best fit with our experimental data. This model was developed using the Buckingham Pi theorem and it has a better performance compared to the other published models. It seems that there is still a long way to go to come up with a unified and universal model for the prediction of the viscosity of nanofluids because of the very complex nature of such materials.

Author details

Majid Al-Wadhahi, G. Reza Vakili-Nezhaad* and Ohoud Al Ghafri
Petroleum and Chemical Engineering Department, College of Engineering, Sultan Qaboos University, Muscat, Oman

*Address all correspondence to: vakili@squ.edu.om

References

[1] Selvakumar RD, Dhinakaran S. Effective viscosity of nanofluids—A modified Krieger–Dougherty model based on particle size distribution (PSD) analysis. Journal of Molecular Liquids. 2017;**225**:20-27

[2] Rudyak VY. Viscosity of nanofluids. Why it is not described by the classical theories. Advances in Nanoparticles. 2013;**2**(03):266

[3] Mahbubul IM, Saidur R, Amalina MA. Latest developments on the viscosity of nanofluids. International Journal of Heat and Mass Transfer. 2012;**55**(4):874-885

[4] Nadooshan AA, Eshgarf H, Afrand M. Evaluating the effects of different parameters on rheological behavior of nanofluids: A comprehensive review. Powder Technology. 2018;**338**: 342-353

[5] Duan F, Kwek D, Crivoi A. Viscosity affected by nanoparticle aggregation in Al_2O_3-water nanofluids. Nanoscale Research Letters. 2011;**6**(1):248

[6] Gaganpreet, Srivastava S. Effect of aggregation on thermal conductivity and viscosity of nanofluids. Applied Nanoscience. 2012;**2**:325-331

[7] Ramachandran K, Kadirgama K, Awad OI, Ramasamy D, Samykano M, Azmi WH. Comprehensive review of principle factors for thermal conductivity and dynamic viscosity enhancement in thermal transport applications: An analytical tool approach. International Communications in Heat and Mass Transfer. 2018;**98**:13-21

[8] Prasher R, Song D, Wang J, Phelan P. Measurements of nanofluid viscosity and its implications for thermal applications. Applied Physics Letters. 2006;**89**(13):133108

[9] Namburu PK, Kulkarni DP, Misra D, Das DK. Viscosity of copper oxide nanoparticles dispersed in ethylene glycol and water mixture. Experimental Thermal and Fluid Science. 2007;**32**(2): 397-402

[10] Li H, Wang L, He Y, Hu Y, Zhu J, Jiang B. Experimental investigation of thermal conductivity and viscosity of ethylene glycol based ZnO nanofluids. Applied Thermal Engineering. 2015;**88**: 363-368

[11] He Y, Jin Y, Chen H, Ding Y, Cang D, Lu H. Heat transfer and flow behaviour of aqueous suspensions of TiO2 nanoparticles (nanofluids) flowing upward through a vertical pipe. International Journal of Heat and Mass Transfer. 2007;**50**(11–12): 2272-2281

[12] Nguyen CT, Desgranges F, Roy G, Galanis N, Maré T, Boucher S, et al. Temperature and particle-size dependent viscosity data for water-based nanofluids–hysteresis phenomenon. International Journal of Heat and Fluid Flow. 2007;**28**(6): 1492-1506

[13] Koca HD, Doganay S, Turgut A, Tavman IH, Saidur R, Mahbubul IM. Effect of particle size on the viscosity of nanofluids: A review. Renewable and Sustainable Energy Reviews. 2017;**82**: 1664-1674

[14] Azmi WH, Sharma KV, Mamat R, Alias ABS, Misnon II. Correlations for thermal conductivity and viscosity of water based nanofluids. In: IOP Conference Series: Materials Science and Engineering (Vol. 36, No. 1, p. 012029). IOP Publishing; 2012

[15] Wang X, Xu X, Choi S, U S. Thermal conductivity of nanoparticle-fluid mixture. Journal of Thermophysics and Heat Transfer. 1999;**13**(4):474-480

[16] Pak BC, Cho YI. Hydrodynamic and heat transfer study of dispersed fluids with submicron metallic oxide particles. Experimental Heat Transfer. 1998;**11**(2): 151-170

[17] Zeinali Heris S, Razbani MA, Estellé P, Mahian O. Rheological behavior of zinc-oxide nanolubricants. Journal of Dispersion Science and Technology. 2015;**36**(8):1073-1079

[18] Nguyen CT, Desgranges F, Galanis N, Roy G, Maré T, Boucher S, et al. Viscosity data for Al2O3–water nanofluid—Hysteresis: Is heat transfer enhancement using nanofluids reliable? International Journal of Thermal Sciences. 2008; **47**(2):103-111

[19] Lee JH, Hwang KS, Jang SP, Lee BH, Kim JH, Choi SU, et al. Effective viscosities and thermal conductivities of aqueous nanofluids containing low volume concentrations of Al2O3 nanoparticles. International Journal of Heat and Mass Transfer. 2008;**51** (11–12):2651-2656

[20] Hwang KS, Jang SP, Choi SU. Flow and convective heat transfer characteristics of water-based Al2O3 nanofluids in fully developed laminar flow regime. International Journal of Heat and Mass Transfer. 2009;**52**(1–2): 193-199

[21] Duangthongsuk W, Wongwises S. An experimental study on the heat transfer performance and pressure drop of TiO2-water nanofluids flowing under a turbulent flow regime. International Journal of Heat and Mass Transfer. 2010;**53**(1–3): 334-344

[22] Lee SW, Park SD, Kang S, Bang IC, Kim JH. Investigation of viscosity and thermal conductivity of SiC nanofluids for heat transfer applications. International Journal of Heat and Mass Transfer. 2011;**54**(1–3):433-438

[23] Khanafer K, Vafai K. A critical synthesis of thermophysical characteristics of nanofluids. International Journal of Heat and Mass Transfer. 2011;**54**(19–20):4410-4428

[24] Keblinski P, Phillpot SR, Choi SUS, Eastman JA. Mechanisms of heat flow in suspensions of nano-sized particles (nanofluids). International Journal of Heat and Mass Transfer. 2002;**45**(4): 855-863

[25] Putra N, Roetzel W, Das SK. Natural convection of nano-fluids. Heat and Mass Transfer. 2003;**39**(8–9):775-784

[26] Anoop KB, Kabelac S, Sundararajan T, Das SK. Rheological and flow characteristics of nanofluids: Influence of electroviscous effects and particle agglomeration. Journal of Applied Physics. 2009;**106**(3):034909

[27] Sekhar YR, Sharma KV. Study of viscosity and specific heat capacity characteristics of water-based Al2O3 nanofluids at low particle concentrations. Journal of Experimental Nanoscience. 2015;**10**(2):86-102

[28] Das SK, Putra N, Roetzel W. Pool boiling characteristics of nano-fluids. International Journal of Heat and Mass Transfer. 2003;**46**(5):851-862

[29] Jang SP, Lee JH, Hwang KS, Choi SU. Particle concentration and tube size dependence of viscosities of Al 2 O 3-water nanofluids flowing through micro-and minitubes. Applied Physics Letters. 2007;**91**(24):243112

[30] Timofeeva EV, Gavrilov AN, McCloskey JM, Tolmachev YV, Sprunt S, Lopatina LM, et al. Thermal conductivity and particle agglomeration in alumina nanofluids: Experiment and theory. Physical Review E. 2007;**76**(6): 061203

[31] Williams W, Buongiorno J, Hu LW. Experimental investigation of turbulent

convective heat transfer and pressure loss of alumina/water and zirconia/water nanoparticle colloids (nanofluids) in horizontal tubes. Journal of Heat Transfer. 2008;**130**(4):042412

[32] Tavman I, Turgut A, Chirtoc M, Schuchmann HP, Tavman S. Experimental investigation of viscosity and thermal conductivity of suspensions containing nanosized ceramic particles. Archives of Materials Science and Engineering. 2008;**34**(2):99-103

[33] Chandrasekar M, Suresh S, Bose AC. Experimental investigations and theoretical determination of thermal conductivity and viscosity of Al2O3/water nanofluid. Experimental Thermal and Fluid Science. 2010;**34**(2):210-216

[34] Murshed SS. Simultaneous measurement of thermal conductivity, thermal diffusivity, and specific heat of nanofluids. Heat Transfer Engineering. 2012;**33**(8):722-731

[35] Ahammed N, Asirvatham LG, Wongwises S. Effect of volume concentration and temperature on viscosity and surface tension of graphene–water nanofluid for heat transfer applications. Journal of Thermal Analysis and Calorimetry. 2016;**123**(2):1399-1409

[36] Buckingham E. On physically similar systems; illustrations of the use of dimensional equations. Physical Review. 1914;**4**(4):345

[37] Chen H, Ding Y, He Y, Tan C. Rheological behaviour of ethylene glycol based titania nanofluids. Chemical Physics Letters. 2007;**444**(4–6):333-337

[38] Hosseini MS, Mohebbi A, Ghader S. Correlation of shear viscosity of nanofluids using the local composition theory. Chinese Journal of Chemical Engineering. 2010;**18**(1):102-107

[39] Masoumi N, Sohrabi N, Behzadmehr A. A new model for calculating the effective viscosity of nanofluids. Journal of Physics D: Applied Physics. 2009;**42**(5):055501

[40] Vakili-Nezhaad GR, Al-Wadhahi M, Gujarathi AM, Al-Maamari R, Mohammadi M. Molecular dynamics simulation of water–graphene nanofluid. SN Applied Sciences. 2019;**1**(3):214

[41] Vakili-Nezhaad G, Al-Wadhahi M, Gujrathi AM, Al-Maamari R, Mohammadi M. Effect of temperature and diameter of narrow single-walled carbon nanotubes on the viscosity of nanofluid: A molecular dynamics study. Fluid Phase Equilibria. 2017;**434**:193-199

Section 3

Thermophysical Properties of Complex Plasmas

Chapter 6

Thermal Conductivity of Dusty Plasmas through Molecular Dynamics Simulations

Aamir Shahzad, Muhammad Qasim Khan, Muhammad Asif Shakoori, Maogang He and Yan Feng

Abstract

The studies of strongly coupled complex plasmas are of significant in the area of science and technology. The plasma thermal conductivity strongly coupled (complex) plasmas is of significant in scientific technology, because it behaves as complex fluids. The two-dimensional (2D) plasma thermal conductivity of strongly coupled complex dusty plasmas (SCCDPs) has been investigated by using the homogenous nonequilibrium molecular dynamics (HNEMD) simulations, proposed by Evan-Gillan scheme, at higher screening parameter κ. In our case, we have chosen particularly higher screening strength (κ) for calculating plasma thermal conductivity. The new simulations of plasma thermal conductivity are computed over an extensive range of plasma states (Γ, κ) for suitable system sizes by applying the HNEMD simulation method at constant external force field strength (F^*). It is found that the plasma thermal conductivity of $SCCDP_S$ decreases by increasing plasma states (Γ, κ). The calculations show that the kinetic energy of $SCCDP_S$ depends upon the system temperature ($1/\Gamma$) and it is independent of κ for higher screening parameter. The new results of thermal conductivity obtained from an improved HNEMD algorithm are in satisfactory agreement with earlier known numerical results and experimental data for 2D $SCCDP_S$. It is depicted that the HNEMD method is a powerful tool to calculate an accurate plasma thermal conductivity of 2D $SCCDP_S$.

Keywords: plasma thermal conductivity, strongly coupled, homogenous nonequilibrium molecular dynamics, force field strength, system size

1. Introduction

The thermophysical properties or physical properties of complex fluids are changed with the variation of pressure, temperature, and composition of the material, but the chemical properties remain unchanged. The phase transition of simple and complex liquids is explained by thermophysical properties [1]. Thermophysical properties consist of both thermodynamic and transport properties of fluid materials. Thermodynamic properties define the equilibrium conditions of the system which consist of temperature, heat capacity, entropy, pressure, internal energy, enthalpy and density whereas the transport properties include thermal conductivity, diffusion viscosity and waves with its instabilities. These transport properties tell

the transfer of energy and momentum to the system under consideration. The transport and thermodynamic properties contain information about the physical phenomena and help to design a system [2]. The thermal properties are calculated through experimentally, computer simulations and can predict through theoretically. The essential transport coefficient of dusty plasma is thermal conductivity and depends upon the internal energy of the particles. The thermal properties of dusty plasmas are computed for a wide combination of dusty plasma parameters by employing different computational techniques. It is a sensitive and complex parameter from the computational point of view because it directly depends on the internal energy of particles. At low temperature and high density, the thermal property of complex liquids/nonideal gases (dusty plasma) is dissimilar from ideal gases (H_2, O_2, N_2, and H_2O) at same higher system parameters. For the calculation of transport properties, particular numerical models are proposed in order to investigate thermal properties for an extensive range of system temperature and density values (Γ, κ). Complex fluids (dusty plasma fluids) have used for many purposes, like power generation, semiconductors industry, cosmetics, paper industry, etc.

1.1 Significance of thermal conductivity

Thermal conductivity is the measurement of heat transfer rate in materials; the experimental parameter gives the information at the microscopic level. It has treated via theoretically based on kinetic theory, Boltzmann equation and linear response theory. The management of thermal transport is in increasing demands in the field of modern technologies. It plays a critical role in a wide variety of practical applications, such as well-organized heat dissipation in nanoelectronics and heat conduction hindering in solid-state thermoelectric. It is well established that heat transport in semiconductors and insulators efficiently modulated by materials processing or structural engineering. Though, practically all the existing approaches include altering the original atomic structure of materials that would delay due to either irreversible structure change or limited tunability of thermal conductivity. The inherent relationship between phonon behaviors and interatomic electrostatic interaction is the efficiently manipulating by thermal transport in materials fundamental thermal physical problems. Electronics cooling or high performance thermal management systems here higher thermal conductivity is needed. Phonons play a dominant role in the thermal transport of semiconductors and insulators [3]. Thermal conductivity and mass transmission over a stretched heated surface with different effects have an abundant and extensive range of applications in various engineering and industrial disciplines. These include glass blowing, extrusion process, melt-spinning, design of heat exchangers, wire and fiber coating, glass fiber production, manufacturing of plastic and rubber sheets, etc. Dusty plasma complex liquids have used in various industries such as semiconductors, energy-powered engineering industries, and microelectronics, and currently, they have vastly used in the field of nanotechnology. It is very necessary to increases thermal conductivity, which increases heat transfer rates. The main concept of the thermal conductivity of different materials and fluids is to increase the transfer heat quickly [4].

1.2 Plasma

Plasma is an ionized gas that contains neutral particles (such as molecules, radicals, and atoms) electrons and positively charged ions. In the universe, 99% of physical matter is in the plasma state and the rest part of the world is only about 1% [5]. In science and technology, plasma has extensive applications and exists in various forms. In space, most of the visible things are in the plasma state, sun and

stars are the significant examples of plasma in our universe. Constitutes of plasma show different behaviors such as quasi-neutrality that comes when positive charges and negative charges density becomes equal. Criteria of plasma at the laboratory level must satisfy three conditions by which we can say that gas is in plasma state or not at a given temperature and number of particles per centimeter cubic. These are three conditions are: (i) $N_D \gg 1$, this mathematical condition shows that the number of particles inside the Debye sphere must be greater than unity; otherwise, that particular gas at given temperature and number of particles per centimeter cubic is not a plasma. Here, $N_D = \frac{4}{3}\pi n \lambda^3{}_{\mathrm{D}}$, where n is the number of particles, and λ_{D} is the Debye length. The size of the Debye length depends upon temperature and density. If the temperature is high, then the size of the Debye length will be large, and if the temperature is low, the size will be small. If the density of plasma is large, then the size of the Debye length will be small, and if the density of plasma is small, then the size of the Debye length will be large, (ii) $\lambda_{\mathrm{D}} < L$, the second condition shows that the size of the ionized system must be greater than the Debye length. Here L is the size of the ionized system, (iii) $\omega_{\mathrm{p}} > \upsilon_c$ or $T_c > 1$, the third condition shows that plasma frequency (ω_{p}) must be greater than the collisional frequency (υ_c), where $1/\omega_{\mathrm{p}} = T_c$, here ω_{p} is the plasma frequency and T_c is the mean time between collisions with neutral atoms [6].

1.2.1 Types of plasmas

Plasma can be described based on different characteristics, such as density, temperature, and degree of ionization of ionized gas. Based on these characteristics, we can differentiate plasma into different types, which have succinctly discussed below. The ratio between charged particles to the total number of particles, including ions and neutrals, is proportional to the degree of ionization of plasma. The charged particle collisions dominate in plasma if the degree of ionization is high. It is low if the collisions between charged particles and neutrals have not dominated. These types are given as (i) *Cold plasma*: the number of electrons and ions equally exists in the positive column of a glow discharged tube in case of nonthermal plasmas (cold plasmas) in the laboratory. The collisions between electrons and neutral atoms depend upon the gas pressure; if the gas pressure is low, then collisions between them are not frequent, and if the pressure of the gas is high, then collisions are more frequent. The motion of gas molecules and ions have overlooked as compared to the motion of electrons because electrons have very high energy than that of the molecules of gas. That is why the nonthermal equilibrium does not exist between them. In the case of cold plasma, the temperature sequence $T_e \gg T_i \gg T_g$ exists between electrons, ions, and gas molecules. In cold plasma, only the electric forces had considered, and the magnetic effects can have ignored. The cold plasma has various applications in different fields such as medical, for example, to sterilize the surface medical instruments, meat, and meat products. For increasing the surface energy of polymers, cold plasma technology has used. To increasing printability and adhesion, the recently developed cold plasma technology has been used. (ii) *Hot plasma*: hot plasma is also known as thermal or fully ionized plasma; the collisions between ions and neutral particles are more frequently at high pressure. The temperatures of both species are approximately equal that fulfill the basic conditions of hot plasma ($T_e \equiv Ti$). In other words, we can say that in hot plasma, all the species have the same temperature. In the hot plasma, the thermal agitations of electrons, ions, and gas molecules cannot have ignored. In the case of hot plasma, the number of charges present in the cloud around the charge ball will be less than the charges on the ball. The screening is not perfect and there is the leakage of electric potential in the order of KBT/e from the cloud. This leakage of electric

potential is responsible for waves [5]. (iii) *Ultracold plasma*: the type of plasma which happens at low temperature (~1 K) is known as ultracold plasma and it is created in several atomic systems containing cesium, rubidium, xenon, calcium, and strontium. Any atoms that can be simply laser-cooled and has a suitable laser wavelength for photoionization have used to create ultracold plasma. The particles have strongly interacted in ultracold plasmas because their thermal energy is less than that of Coulomb energy between the adjacent particles [7]. (iv) *Ideal plasma*: the type of plasma in which Coulomb collisions are negligible, and the potential energy is minimal than the kinetic energy, then such kind of plasma is called ideal plasma. This type of plasmas has small densities and very high temperatures.

1.2.2 Role of nonideal (complex) plasma

In nonideal plasmas, the Coulomb collisions are not negligible. The mean energy of interparticle interactions increases by increasing the density. Nonideal plasmas become when the mean K.E and the mean power of the interparticle interactions become comparable. It can occur in the dense planetary atmosphere during the hypersonic motion of bodies, as a result of simulation of matter by sharp shock, concentrated laser radiations, detonation, and electric explosion waves and under the powerful chemical and nuclear explosion conditions and electron and ion fluxes. Because Coulomb collisions are active in nonideal plasmas, so, on the bases of Coulomb coupling, the nonideal (complex) plasmas have categorized in two classes. (i) Strongly coupled dusty plasma (SCDP) and (ii) weakly coupled dusty plasma (WCDP). These two terms have described by using the plasma coupling parameter Γ of a collection of charged particles, which is the ratio between potential energy to kinetic energy. Mathematically Coulomb coupling parameter is given as, $\Gamma = \langle P.E\rangle / \langle K.E\rangle \equiv Q^2/dk_BT$. Strongly coupled plasmas, which are also known as nonideal plasmas, are the collection of a multicomponent charged particle that interacts with each other and remains at fixed positions. If the Coulomb coupling parameter "Γ" is more significant than unity ($\Gamma \geq 1$) then such type of plasma is called strongly coupled plasma. It is also known as cold plasma. In the laboratory, such type of plasma have generated at high density and low temperature. Due to significant interactions between neighboring dust charged particles, it has found in different phases, such as liquefy, liquid, cold liquids, and structural form. With the help of the coupling parameter structure of matter can be determined. If the Γ (Coulomb coupling) parameter is less than 1 ($\Gamma < 1$), then such type of plasma is called weakly coupled Dusty plasma (WCDP) or ideal plasma and has no structure like a gas. In weakly coupled Dusty plasmas, kinetic energy must be greater than the potential energy (K.E > P.E). $WCDP_S$ has also recognized as hot plasmas, and particle motion in WCP_S is just like a molecular motion in gases. In hot plasma, thermal agitations are present, and screening will not be perfect.

1.3 Complex (dusty) plasma and applications

Plasma consists of electrons, ions, and neutral atoms; in addition to dust particles is known as dusty (complex) plasma. Due to dust particles, the physical properties of the plasma become complicated; that is why we call them also complex plasma. The study of dusty plasmas has become a developing branch of plasma physics in the field of sciences, technologies, and space. The study of dusty plasmas had become interesting for research of laboratory plasma when the formation of dust and dust trapping was observed during the plasma etching of silicon wafers and to limit the deposition rate when powder formation in plasma-enhanced CVD was identified. Dust is present everywhere in the space, such as interplanetary dust

in planetary rings and in comet tails, and also it have present in the atmosphere and earth magnetosphere. These charged particles interact with each other and with the plasma constituents such as electrons, ions, and neutral atoms due to which plasma behavior becomes complicated [8]. These charged dust particles change the properties of plasma by electric and magnetic fields. The value of the Coulomb coupling parameter between dust particles is high due to the massive dust charge, which leads to the liquid and solid phase of the dust system at room temperature. For study the phase transitions and structural properties of solids, Yukawa balls and plasma crystals are appropriate systems. Plasma with dust particles can be termed as either "dust in plasma" or "dusty plasma" depending on the ordering of several characteristic lengths and radius between interacting particles (r_d and λ_D). If the Debye length of dust particles (λ_{Dd}) is less than the interparticle distance (r_d) then it is called dust in plasma. Mathematically it is written as $\lambda_{\mathrm{Dd}} < r$. Here "$r_d$" is the interparticle distance, and "λ_{Dd}" is the Debye length of dust particles. In this case, there are no dust particles in the plasma sphere. If the Debye length of dust particles (λ_{Dd}) is greater than the interparticle distance (r) then it is called dusty plasma. Mathematically it is written as $\lambda_{\mathrm{Dd}} > r$ and it shows that dust particles are present in the plasma sphere.

In industrial applications, dust particles distributed in the plasma and produced disturbing effects in plasma. This contamination in the plasma has devastating effects on the fabricated circuits. On the other side, applications such as surface processing make the use of dust particles that have spread in the plasma. For example, the growth of carbon-based nanostructures on the surface used for electronic devices such as sensors, silicon-based films which have used in solar cells, and flat-panel displays illustrates an enhanced performance of nanoparticles produced in the plasma through chemical reactions, are inserted into the film. Through plasma processing, the coating of particles has produced. Plasma-based materials processing technologies have widely used in the manufacturing of integrated circuits. To etch, sputter, or modify the surface properties of silicon wafer, chemically reactive plasma have used. The fine dust particles created in plasma chemical systems have useful and exciting features that also control their compositions and size. It has used to grow or modify existing materials.

1.3.1 Merits and demerits of dust particles

Initially, the dust has not considered a useful technological consequence in the plasma. It has simply considered an unwanted pollutant in the plasma. To minimize the negative influences of dust particles in the plasma leads to the development of material science. The nanoparticles have considered as the basic building blocks of nanotechnology in plasma discharges. There are many advantages of dust particles in dusty plasmas such that nanocrystalline silicon particles have used to enhance the lifetime and efficiency of silicon solar cells, which have developed in silane plasmas. Dust particles have used to improve the surface properties of materials by applying plasma-enhanced CVD systems. The thin films produced by PECVD systems of TiN in an amorphous Si_3N_4 matrix have very high elastic modulus and hardness. In hydrocarbon plasmas such as methane or acetylene, carbon-based nanostructures have developed to govern thin carbon films, which lead to materials of high hardness, wear-resistance, and chemical inertness. In Ar/CH_4 plasmas, the fabrication of nanocrystalline diamond films has done. These films have unique properties such as high hardness, chemical inertness, and extreme smoothness [9]. Dust particles are also used in the ceramic industry for sintering and in the fabrication of hard coatings, and also used in optical devices. Dust particles decrease the performance and the yield of many electronic devices. In the semiconductor industry, dust

particles reduced the performance and yield of semiconductors. Dust particle contamination in the medical field during the production of different kinds of medicines has serious issues. The dust particles are of micron-sized, which reduces the adhesion of thin films of different materials due to deposition on the surfaces and also creates dislocations. In industrial applications, dust particles contamination in the plasma creates many defects in the manufacturing of microchips and fabricated circuits. Dust particles disturb the stability and the safety of the plasma in fusion reactors.

2. Molecular dynamics simulations

Over the last seven decades, the computer performance's speed to elementary calculations has increased by 10^{15} factor. The computer memories, data storage also increased at a similar speed. Nowadays, by using computer simulation, we can save both time and money. The fundamental purpose of computer simulation is to guide the real experiment more precisely. Computer simulations used to predict various properties of gases, liquids, solids, and biological organisms. It is very useful for checking theoretical results, understanding experimental observation for the case where no academic data available. It also allows us to the identification of essential processes and visualization of the system [10]. The molecular dynamics simulations (MDS) one of the computer simulations techniques, in these technique atoms and molecules, are assumed to follow Newton's law as $F_i = ma_i \equiv md^2r/dt^2$, where F, m and a represent the force, mass, and accretions of ith particles in x-coordinate direction. In this book chapter, we integrate this equation by the predictor-corrector method. MDS has two basic types depends on the properties, which we are going to calculate one is equilibrium molecular dynamics simulations (EMDS), and another is nonequilibrium MDS (NEMDS). In this work, we have applied NEMDS to investigate the thermal conductivity of SCDPs at different dusty plasma parameters [11, 12].

2.1 Numerical model and algorithm

NEMDS is used to obtain the trajectory of dust particles' motion of a system [13] that interacts with each other through an interparticle Yukawa potential [14]. Homogeneous nonequilibrium molecular dynamic simulation (HNEMDS) approach have used for the calculation of thermal conductivity of complex (dusty) plasma liquids, which are molded, using a most common Yukawa (screened Coulomb) potential for charged particles [15] and has the following form,

$$\phi_Y(|\mathbf{r}|) = \frac{Q^2}{4\pi\varepsilon_0}.\frac{e^{-|\mathbf{r}|/\lambda_D}}{|\mathbf{r}|} \tag{1}$$

Here "$\boldsymbol{r}$" is the magnitude of interparticle distance, Q is the charge of dust particles, and λ_D is the Debye screening length. We have three normalized (dimensionless) parameters to characterize the Yukawa interaction model $\phi_Y(|\mathbf{r}|)$: (i) the plasma Coulomb coupling parameter define as: $\Gamma = \left(Q^2/4\pi\varepsilon_0\right).(1/a_{ws}k_BT)$, where a_{ws} is Wigner Seitz radius and it is equal to $(n\pi)^{-1/2}$, here n is the number of particles per unit area (N/V). The k_B and T are Boltzmann constant and absolute temperature of the system, (ii) the screening strength (dimensionless inverse) $\kappa = {}^{aws}/_{\lambda_D}$, and (iii) normalized external force field strength, $F^* = (F_Z).\left(a_{ws}/\mathbf{J}_Q\right)$ [15, 16]. We have applied periodic boundary conditions and Gaussian thermostat in

canonical ensemble (*NVT*) in order to constant temperature for a Yukawa system. The further detail of these three dimensionless parameters is given in our earlier work of Refs. [15–17]. We started from a well-known, the Green-Kubo relations (GKR_S) for the hydrodynamic transport coefficients of uncharged particles [18]. This important GKR_S of pure liquids have applied to calculate the thermal conductivity of 2D and 3D $SCCDP_S$ [11, 12, 19–27].

$$\lambda = \frac{1}{2k_B A T^2} \int_0^\infty \langle \mathbf{J}_Q(t).\mathbf{J}_Q(0) \rangle dt, \tag{2}$$

where in Eq. (2), k_B is the Boltzmann's constant, A is the system area, T is the system temperature, and $\mathbf{J_Q}$ is the current heat vector at time t of 2D case. In our MD simulation, the angular brackets represent an ensemble average. In this model, the expression for the microscopic heat current vector $\mathbf{J_Q}$ [16, 17] can be given by

$$\mathbf{J}_Q(t)A = \sum_{i=1}^{N} E_i \frac{\mathbf{p}i}{m} - \frac{1}{2}\sum_{i \neq j} (\mathbf{r}i - \mathbf{r}j).\left(\frac{\mathbf{p}i}{m}.\mathbf{F}ij\right) \tag{3}$$

Where $\mathbf{F}_{ij}$ is the total interparticle force at time t, on particle i due to j, $\mathbf{r}_{ij} = \mathbf{r}_i - \mathbf{r}_j$ are the position vectors (interparticle separation), and $\mathbf{P}_i$ is the momentum vector of the ith particle. Where, E_i is the total energy of particle i, and is given by the expression as

$$E_i = \frac{\mathbf{p}^2{}_i}{2m} + \frac{1}{2}\sum_{i \neq j} \phi_{ij} \tag{4}$$

Where ϕ_{ij} is the Yukawa pair potential between particle i and j and given by Eq. (1). Here, in Eq. (4) the first term represents the kinetic energy (K.E), and the second term represents the potential energy (P.E). The Evan's [28–30] proposed the non-Hamiltonian linear response theory (LRT), has been used for a moving system representing the equation of motion

$$\dot{\mathbf{r}}_i = \frac{\mathbf{p}_i}{m} \tag{5}$$

$$\dot{\mathbf{p}}_i = \sum_{J=1}^{N} \mathbf{F}_i + \mathbf{D}_i(\mathbf{r}_i, \mathbf{p}_i).\mathbf{F}_e(t) - \alpha \mathbf{p}_i \tag{6}$$

In Eq. (6), $\mathbf{F}_i = \left(-\partial\phi_{ij}/\partial r_i\right)$ is the total Yukawa interparticle force acting on particle i in an N-particle system and $\mathbf{D}_i = \mathbf{D}_i(\mathbf{r}_i, \mathbf{p}_i)$ is the phase space distribution function with $\mathbf{r}_i$ and $\mathbf{P}_i$ being the coordinate and momentum vectors of the ith particle. Mechanical work is performed through the externally applied force field $\mathbf{F}_e(t)$ and thus the equilibrium cannot be maintained. In the above expression, α is the Gaussian thermostat multiplier that keeps the system temperature [15–22, 28] and it is given as

$$\alpha = \frac{\sum_{i=1}^{N}\left[\mathbf{F}_i + \mathbf{D}_i(\mathbf{r}_i, \mathbf{p}_i).\mathbf{F}_e(t)\right].\mathbf{p}_i}{\sum_{i=1}^{N} p_i^2/m_i} \tag{7}$$

When an external force field parallel to the z-axis is of the form $\mathbf{F}_e(t) = (0, F_Z)$, in the limit $t \to \infty$ [15, 31] then, the thermal conductivity is calculated as

$$\lambda = \frac{1}{2k_B A T^2} \int_0^\infty \left\langle \mathbf{J}_{Q_z}(t) \mathbf{J}_{Q_z}(0) \right\rangle dt = \lim_{F_z \to 0} \lim_{t \to \infty} \frac{-\left\langle \mathbf{J}_{Q_z}(t) \right\rangle}{T F_z} \tag{8}$$

In Eq. (8), $\mathbf{J}_{Q_Z}(t)$ is the z-component of the current heat vector and the external force field $\mathbf{F}_e(t) = (F_Z)$ [15–22, 31].

In this study we have used the same method as employed in our earlier work of 3D strongly coupled dusty plasmas [11, 12]. The most computational time consuming part of used algorithm is to compute the interparticle interactions (force and internal energy). It has been shown in our previous work that the proposed method has advantage to calculate Yukawa forces and relevant energy in appropriate computational time with reasonable computational power. In our present case, the HNEMD method is used to compute the thermal conductivity of 2D plasma systems and production stage of thermal conductivity is obtained between $10^6/\omega_p$ and $2 \times 10^6/\omega_p$ time units for each plasma states. It shows that the used method is computational time cost-effective and power saving as compared to earlier methods based on different numerical schemes [12, 14, 26, 27].

3. Simulation results and discussion

In this section, the processing of the data of our computer simulation gave us the numerical results of the thermal conductivity of 2D complex (dusty) plasmas. We have used HNEMD simulations over the wide range of plasma Coulomb Couplings Γ (=10, 500) and four higher Debye screening strengths κ (= 4.5, 5.0, 5.5, and 6) at constant low normalized external force field strength F^*(=0.02). In the present work, our 2D SCDPs through HNEMD simulations have carried out for a constant number of particles (N = 400) in a simulation box with edges length (L_x, L_y). We have applied to the squared simulation box wraparound periodic boundary conditions (PBC). For nonequilibrium conditions of the systems, we run our MDS code 200000 time steps. Here we have used constant dt = 0.001 in integrated equation via predictor-corrector algorithm for the calculations of dust particles positions, velocity and acceleration. For each time step, the position, velocity, acceleration and forces of each spherical dust particles are calculated and update it. The HNEMD method is more powerful for computing forces and energy of Yukawa interactions and more effective as compared to earlier numerical methods of 2D and 3D ([13, 14, 23–27] and their references herein).

Figures 1 and **2** present the simulation results obtained by applying the Evan-Gillan HNEMD approach of thermal conductivity (λ_0) with appropriate normalization (plasma frequency, ω_p) as $\lambda_0 = \lambda/nm\omega_P a^2$, at the normalized external constant force field strength F^* (0.002) for 2D SCDPs systems. In every graph, demonstrate the comparison of thermal conductivity present results with previously known 2D SCDPs results that investigate through MD simulations techniques as GKR-EMD of Khrustalyov and Vaulina [27] at the higher scaling factor ($\xi = \infty$), and NEMD simulation data of Hou and Piel [26].

Figures 1 and **2** display the normalized thermal conductivity (λ_0) calculated at higher Debye screening strengths (κ = 4.5, 5, 5.5, 6) with setting N = 400 particles [22]. These **Figures 1** and **2** have plotted between Coulomb coupling (Γ) parameter and normalized thermal conductivity (λ_0) taken along the axis, x and y, respectively. It is noted that our simulation results are in better accordance with the earlier known numerical simulation results of 2D Yukawa liquids, at N = 400 [22]. It has investigated that, our new calculations for λ_0 at the lower value of

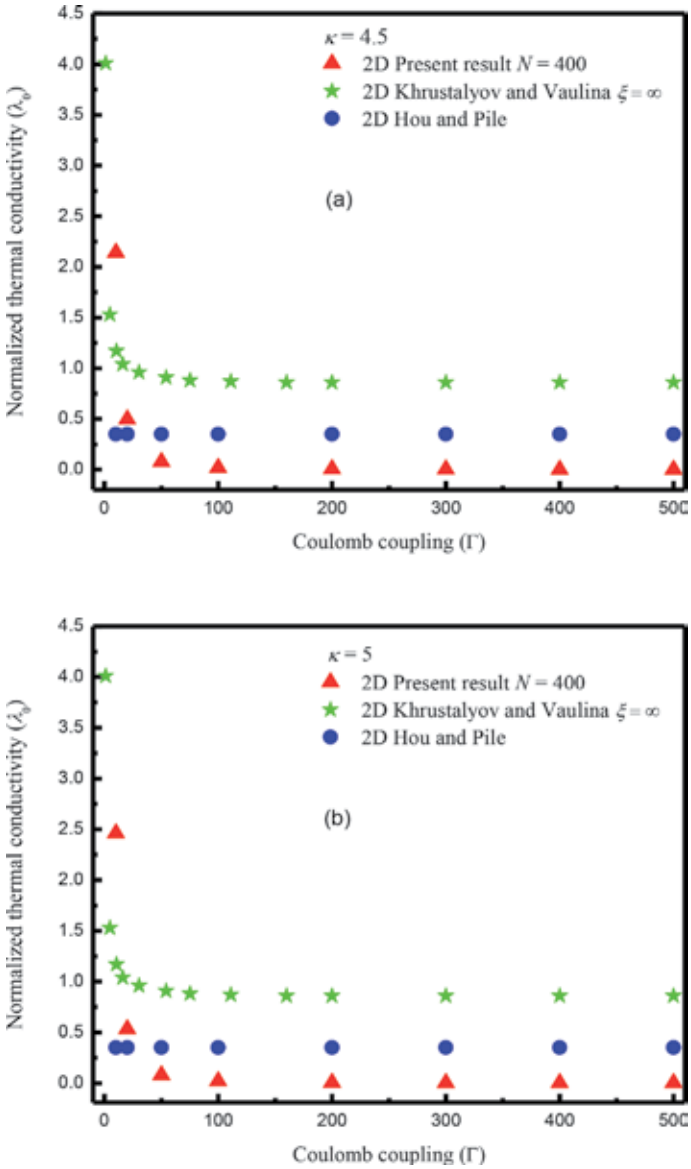

Figure 1.
Normalized plasma thermal conductivity (λ_o) results from comparison versus coulomb coupling Γ ($10 \leq \Gamma \leq 500$) (system temperature) for SCCDP$_S$ computed from HNEMD at higher Debye screening, (a) κ = 4.5 and (b) κ = 5. Two-dimensional, GKR-EMD results of Khrustalyov and Vaulina (KV) [27] at the higher scaling parameter (ξ = ∞), and NEMD results of Hou and Piel (HP) [26]: current results (with 400 particles).

coupling Γ (≡ 20) are lower than that of GK-EMD of Khrustalyov and Vaulina (KV) at the higher factor of scaling $\xi = \infty$ [27], and higher than 2D-NEMD estimations of Hou and Piel [26]. It is important to note that a constant behavior of λ_0 has examined at intermediate -higher Coulomb couplings ($50 \leq \Gamma \leq 500$) at constant force field $F^* \equiv 0.02$ [11], and well agreed with the previously known 2D SCDPs numerical simulation results of GKR-EMD [27] and NEMD [26] estimations. Moreover, it has observed that from the present simulation data, the existence of λ_0 is present for the entire range of plasma coupling Γ ($10 \leq \Gamma \leq 500$) at higher Debye screening (κ). The remains within an acceptable limited statistical uncertainty and also confirming the earlier computer simulation calculations of

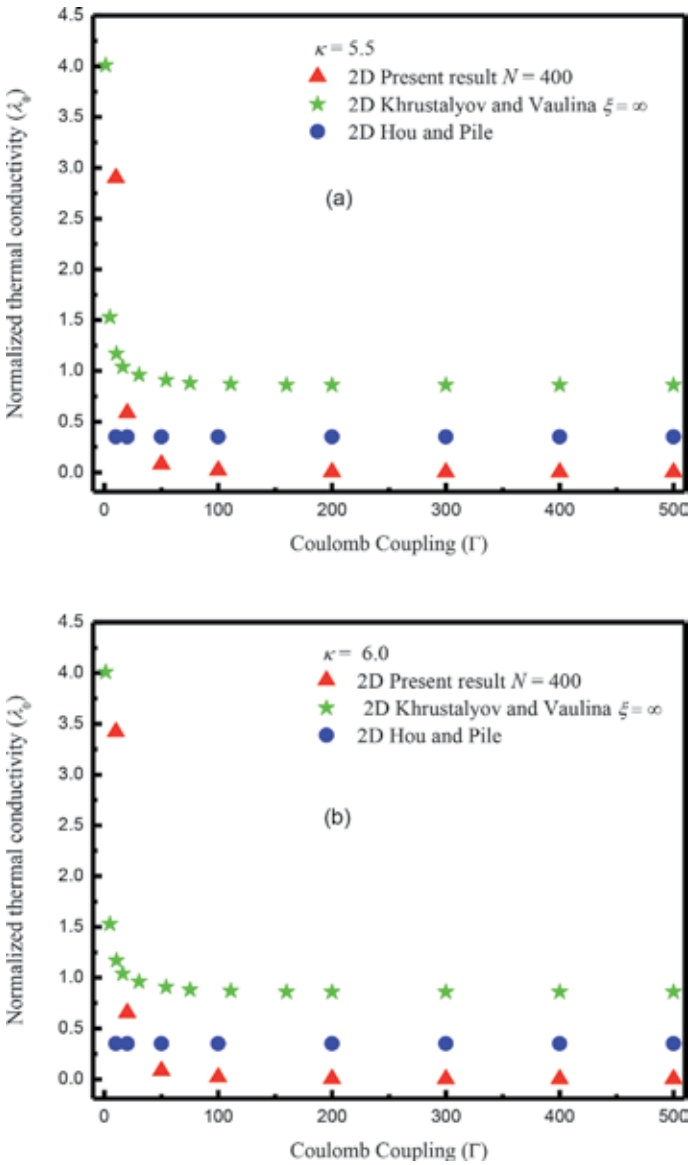

Figure 2.
Normalized plasma thermal conductivity (λ_o) results from comparison versus Coulomb coupling Γ ($10 \leq \Gamma \leq 500$) (system temperature) for SCCDP$_S$ computed from HNEMD at higher Debye screening, (a) $\kappa = 5.5$ and (b) $\kappa = 6$. Two-dimensional, GKR-EMD results of Khrustalyov and Vaulina (KV) [27] at the higher scaling parameter ($\xi = \infty$), and NEMD results of Hou and Piel (HP) [26]: current results (with 400 particles).

Shahzad and He [22]. The present simulation results show that the λ_0 decreases towards the higher Γ along with increasing the Debye screening (κ) [13]. It has investigated that our calculation of λ_0 for the lower value of Γ indicates that the interactions between the particles are very feeble, and the effectiveness of the screening parameter is large, and the K.E of particles is maximum. At intermediate-higher plasma coupling ($50 \leq \Gamma \leq 500$), the present results are below than the earlier 2D GKR-EMD numerical results of Khrustalyov and Vaulina [27] at the higher parameter of scaling $\xi = \infty$ [11], and 2D NEMD simulation estimations of Hou and Piel [24]. It has also observed that the presented simulation results are in better accordance with the previously known numerical results of 2D

Yukawa liquids at a normalized constant force field strength of $F^* = 0.02$. It is noted from these figures, our 2D HNEMD simulation results of λ_0 at the higher value of Debye screenings (κ = 4.5, 5, 5.5, 6) existing from nonideal state Γ (=10) to a strongly coupled liquid state Γ (= 180) and further strongly coupled liquid state Γ (=180) to strongly coupled solid-state ($180 \leq \Gamma \leq 500$). **Figures 1** and **2** show that the λ_0 exists for lower plasma coupling $\Gamma \leq 20$, which is the clear contradiction with the previously known simulation results of Donkó and Hartmann [13] where the λ_0 have not found at $\Gamma \leq 20$. Moreover, **Figures 1** and **2** show that the present simulation results have constant (straight line) behavior of λ_0 with increasing coulomb coupling (Γ). For higher Debye screening (κ) values for 2D $SCDP_S$, that is the unlike to the simulation results of Shahzad and He [22], where the λ_0 displays a slightly growing behavior with increasing Γ for κ = 4. The possible reason for the difference between the present results and the previously known results of λ_0 may be the numerical error among HNEMD, NEMD, and GKR-EMD data.

It has proposed from these figures that measured results of λ_0 are in good accordance with earlier results at intermediate-high Γ. Nonetheless, a few outcomes veer at the lower Γ points; however, all within the statistical limited uncertainty range. **Figures 1** and **2** demonstrates that the presented HNEMD approach may accurately calculate the plasma thermal conductivity of strongly coupled complex (dusty) plasmas. We have shown that the present approach has excellent execution, and its exactness is exceptionally near to prior EMD and NEMD methods. It has concluded that our results rely upon the plasma parameters of Coulomb coupling and Debye screening strength, affirming previous simulations. Besides, it has demonstrated that the position of minimum value of thermal conductivity shifts towards higher Γ with an increase in κ, as expected in earlier numerical approaches. It is noticed that the improved HNMED method is excellent for lower system sizes with constant external force field strength, where the signal to noise ratio is acceptable for equilibrium plasma thermal conductivity [31–33].

4. Summary

In this work, we have derived the plasma thermal conductivity of 2D SCDPs liquids over a suitable range of plasma couplings ($10 \leq \Gamma \leq 500$) and screening strengths ($4.5 \leq \kappa \leq 6$) at constant external force field strength by using HNEMD approach. Calculations have carried out employing HNEMD are in reasonable agreement with the earlier results measured from EMD and NEMD for SCDPLs. New investigations show that the minimum values of thermal conductivity shifts towards higher Γ with an increase of screening κ but remains within a reasonably limited statistical uncertainty, confirming the earlier simulation results. It has shown that the plasma thermal conductivity depends on plasma parameters (Γ, κ) in 2D complex dusty systems that illustrate earlier results of SCCDPLs. This chapter provides the understanding and investigation of the nonlinear regime of the SCCNPs for a suitable low value of external force field strength. In future work, the newly obtained results for thermal conductivity may be advantageous for developing new techniques of complex (dusty) plasmas diagnostics and also for improving the current experimental techniques for understanding the many nonideal systems like dusty plasmas, polymers, and biological and medical solutions The remarkable outputs obtained from the successful development of employed model and can be used by the research labs and academia for their validation. The general experimentation on small scale and later on technological trials in industries will lead to the use of this plasma property for technology development purpose.

Acknowledgements

The authors thank Z. Donkó (Hungarian Academy of Sciences) for providing his thermal conductivity data of Yukawa Liquids for the comparisons of their simulation results, and useful discussions. They are grateful to the National Advanced Computing Center of National Center of Physics (NCP), Pakistan, for allocating computer time to test and run their MD code.

Abbreviations

SCCNPs	strongly coupled complex nonideal plasmas
HNEMD	homogeneous nonequilibrium molecular dynamics
Γ	Coulomb coupling
κ	Debye screening length
F^*	external force field strength
HNEMD	homogenous nonequilibrium molecular dynamics
NEMD	nonequilibrium molecular dynamics
MD	molecular dynamics
InHNEMD	inhomogenous nonequilibrium molecular dynamics
SCP	strongly coupled plasma
EMD	equilibrium molecular dynamics
λ	thermal conductivity
λ_0	normalized thermal conductivity
PBCs	periodic boundary conditions
VP	variance procedure
HPMD	homogenous perturbed MD
N	number of particles

Author details

Aamir Shahzad[1,2*], Muhammad Qasim Khan[1], Muhammad Asif Shakoori[2], Maogang He[2] and Yan Feng[3]

1 Molecular Modeling and Simulation Laboratory, Department of Physics, Government College University Faisalabad (GCUF), Faisalabad, Pakistan

2 Key Laboratory of Thermo-Fluid Science and Engineering, Ministry of Education (MOE), Xi'an Jiaotong University, Xi'an, People's Republic of China

3 Center for Soft Condensed Matter Physics and Interdisciplinary Research, College of Physics, Optoelectronics and Energy, Soochow University, Suzhou, China

*Address all correspondence to: aamirshahzad_8@hotmail.com; aamir.awan@gcuf.edu.pk

References

[1] Fortov VE, Vaulina OS, Lisin EA, Gavrikov AV, Petrov OF. Analysis of pair interparticle interaction in nonideal dissipative systems. Journal of Experimental and Theoretical physics. 2010;**110**:662-674

[2] Wakeham WA, Nagashima A, Sengers JV. Measurement of the transport properties of Fluids. In: Experimental Thermodynamics. Vol. **3**. Malden, MA: Blackwell Science; 1991

[3] Qin G, Qin Z, Yue S-Y, Yan Q-B, Ming H. External electric field driving the ultra-low thermal conductivity of silicene. Nanoscale. 2017;**9**(21):7227-7234

[4] Khan H, Haneef M, Shah Z, Islam S, Khan W, Muhammad S. The combined magneto hydrodynamic and electric field effect on an unsteady Maxwell nanofluid flow over a stretching surface under the influence of variable heat and thermal radiation. Applied Sciences. 2018;**8**(2):160

[5] Chen FF. Introduction to Plasma Physics and Controlled Fusion. 2nd ed. New York: Springer Verlag; 2006

[6] Chen FF. Industrial Applications of Low-Temperature Plasma Physics. Los Angeles: University of California; 1995. pp. 90024-91594

[7] Killian T, Pattard T, Pohl T, Rost J. Ultracold neutral plasmas. Physics Reports. 2007;**449**:77

[8] Piel A. Plasma Physics: An Introduction to Laboratory, Space, and Fusion Plasmas. Heidelberg, Berlin: Springer Science & Business Media; 2010. pp. 1-378. DOI 10.1007/978-3-642-10491-6

[9] Merlino RL. Dusty plasmas and applications in space and industry. Plasma Physics Applied. 2006;**81**:73-110

[10] Frenkel D. Simulations: The dark side. The European Physical Journal Plus. 2013;**128**(1):10

[11] Shahzad A, Haider SI, Kashif M, Shifa MS, Mu T, He MG. Thermal conductivity of complex plasmas using novel Evan-Gillan approach. Communications in Theoretical Physics. 2018;**69**(6):704

[12] Shahzad A, Shakoori MA, He MG, Yang F. Dynamical structure factor of complex plasmas for varying wave vectors. Physics of Plasmas. 2019;**26**: 023704

[13] Donkó Z, Hartmann P. The thermal conductivity of strongly coupled Yukawa liquids. Physical Review E. 2004;**69**(1):016405

[14] Ott T, Bonitz M. Effective coupling parameter for 2D Yukawa liquids and non-invasive measurement of plasma parameters. 2010. arXiv preprint arXiv: 1010.6193

[15] Shahzad A, He MG, Irfan Haider S, Feng Y. Studies of force field effects on thermal conductivity of complex plasmas. Physics of Plasmas. 2017;**24**(9):093701

[16] Shahzad A, He MG. Thermal conductivity of three-dimensional Yukawa liquids (dusty plasmas). Contributions to Plasma Physics. 2012; **52**(8):667-675

[17] Shahzad A, He MG. The numerical experiment of thermal conductivity in two-dimensional Yukawa liquids. Physics of Plasmas. 2015;**22**(12):123707

[18] Hansen JP, McDonald IR. Theory of Simple Liquids. London: Academic; 1986 (1976; Google Scholar: 179)

[19] Shahzad A, He MG. Thermal conductivity calculation of complex (dusty) plasmas. Physics of Plasmas. 2012;**19**(8):083707

[20] Shahzad A, Aslam A, He MG. Equilibrium molecular dynamics simulation of shear viscosity of

two-dimensional complex (dusty) plasmas. Radiation Effects and Defects in Solids. 2014;**169**(11):931-941

[21] Shahzad A, He MG. Interaction contributions in thermal conductivity of three dimensional complex liquids. AIP Conference Proceedings. 2013;**1547**: 172-180

[22] Shahzad A, He MG. Homogeneous nonequilibrium molecular dynamics evaluation of thermal conductivity in 2D Yukawa liquids. International Journal of Thermophysics. 2015;**36** (10–11):2565-2576

[23] Salin G, Caillol JM. Equilibrium molecular dynamics simulations of the transport coefficients of the Yukawa one component plasma. Physics of Plasmas. 2003;**10**(5):1220-1230

[24] Faussurier G, Murillo MS. Gibbs-Bogolyubov inequality and transport properties for strongly coupled Yukawa fluids. Physical Review E. 2003;**67**(4): 046404

[25] Donko Z, Hartmann P. Shear viscosity of strongly coupled Yukawa liquids. Physical Review E. 2009;**78**: 026408

[26] Hou LJ, Piel A. Heat conduction in 2D strongly coupled dusty plasmas. Journal of Physics A: Mathematical and Theoretical. 2009;**42**(21):214025

[27] Khrustalyov YV, Vaulina OS. Numerical simulations of thermal conductivity in dissipative two-dimensional Yukawa systems. Physical Review E. 2012;**85**(4):046405

[28] Evans DJ. Homogeneous NEMD algorithm for thermal conductivity—Application of non-canonical linear response theory. Physics Letters A. 1982;**91**(9):457-460

[29] Evans D, Morriss G. Statistical Mechanics of Nonequilibrium Liquids. London: Academic; 1990

[30] Shahzad A, Sultana M, Aslam A, He MG. Molecular dynamics simulations of thermal conductivity in 2D complex Yukawa liquids. IOP Conference Series: Materials Science and Engineering. 2013;**60**:012038

[31] Shahzad A. Impact of Thermal Conductivity on Energy Technologies. London: IntechOpen; 2018. DOI: 10.5772/intechopen.72471

[32] Shahzad A, Haider SI, He MG, Yang F. Introductory Chapter: A Novel Approach to Compute Thermal Conductivity of Complex System, a Chapter from the Book of Impact of Thermal Conductivity on Energy Technologies. London: IntechOpen; 2018. 3 p. DOI: 10.5772/intechopen. 75367

[33] Shahzad A, He M-G. Thermal Conductivity and Non-Newtonian Behavior of Complex Plasma Liquids, a Chapter from the Book of Thermoelectrics for Power Generation—A Look at Trends in the Technology. InTech: Rijeka, Croatia; 2016. p. 305. DOI: 10.5772/65563

Chapter 7

Waves and Instabilities in E × B Dusty Plasma

Sukhmander Singh

Abstract

Hall thrusters are common examples of E × B configuration, where electron trajectory gets trapped along the external magnetic field lines. This significantly increases the residence time of electrons in the plasma discharge channel. Hall thrusters are potential candidates for spacecraft station keeping, rephrasing and orbit topping applications because of its high thrust resolutions and efficiency. The goal of this chapter is to explain the working principle of Hall thrusters and to characterize the resistive instability in hot dusty plasma. The studies of these instabilities are useful to design efficient Hall thrusters and to understand the solar dusty plasma. The large amplitude of these oscillations has an adverse effect on the power processing unit of the devices. This reduces the efficiency and specific impulse and shortens the operating life of the Hall thruster. The theory of linearization of fluid equation for small oscillation has been given. The chapter also discusses the origin of plasma oscillation in a plasma discharge mechanics.

Keywords: plasma oscillations, instabilities, Hall thrusters, resistive plasma, growth rate

1. Introduction to E × B devices

There are some devices where plasma is weakly magnetized because of the larger Larmor radius of the massive ions against the length of the discharge channel. Electrons get trapped along the magnetic field lines in the channel. Hall thrusters and magnetrons are the common examples of E × B devices. The E × B configuration is used to confine electrons, increasing the electron residence time and allowing ionization and plasma sustainment. Hall thrusters have emerged as an integral part of propulsion technology. Unlike chemicals and electric rockets, in a Hall thruster, the propulsion thrust is achieved by gas which has high atomic number and low ionization potential. For this Xenon is mostly used. In the discharge channel, Xenon is ionized and then accelerated by electrostatic forces. Hall thrusters are versatile electric propulsion devices, where thrust efficiencies can exceed 50% and specific impulses are typically between 20 min and 1 h. The specific impulse has the dimension of time and is a measure for the effective lifetime of the thruster, when lifting its own propellant from the earth's surface. The specific impulse is defined as $I_{sp} = T/\dot{m}_p g$, where $\dot{m}_p$ is the mass flow rate; T is the thrust, which is the total force undergone by the Hall Thruster in relation to the acceleration of the ions; and g is the acceleration due to gravity. If the propellant is fully ionized, the specific impulse is equal to the mean axial component of the final ion velocity divided by g.

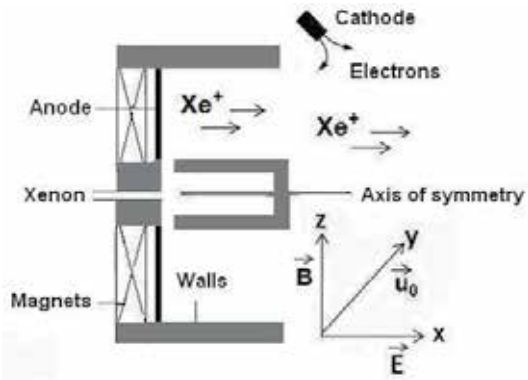

Figure 1.
Schematic diagram of a typical Hall plasma thruster [3].

It is interesting that these thrusters adjust their thrust and impulse by varying the acceleration voltage and the flow rate of the propellant. The fine tuning of the thrust correction can be done for the compensation of atmospheric drag for low-flying satellites using its high thrust resolution. The necessary thrust for such applications ranges from micro-Newtons to some Newtons with electric input powers of some 10 to some 10,000 Watts [1–4].

Figure 1 shows the internal components of a Hall thruster which is generally made of an axis-symmetric cylindrical discharge chamber. A cathode is fixed outside to produce electrons to neutralize the outer surface of the device to overcome the space-charging problems. A high atomic weight number and low ionization potential gases are preferred propellant (Xenon, Argon) for Hall thrusters to get more thrust. The propellant enters from the left side of the channel via anode and gets ionized through the hollow cathode of the device. The electric field of strength ~1000 V/m gets generated inside the discharge channel along the axial direction of the device. By using magnets around the annular channel and along the thruster centreline, a radial magnetic field of moderate strength (~150–200 G) is created, which is strong enough for the electrons to get magnetized, i.e. they are able to gyrate within the discharge channel, but the ions remain unaffected due to their Larmor radius much larger than the dimension of the thruster [3].

We used a Cartesian coordinate system to understand the different forces on the particles inside the channel and let us suppose, the X-axis represents, the axis of the thruster. Generally, the applied electric and magnetic fields are in axial (along X axis) and radial (along Z axis) directions, respectively, of the device. Therefore because of the perpendicular electric and magnetic fields, the Lorentz forces act on the electrons along the Y axis ($\vec{E} \times \vec{B}$ azimuthal direction). Since electrons have smaller Larmor radius than the length of the channel, therefore electrons rotate along the azimuthal direction under the influences of the Lorentz force [1–4].

2. Review on plasma instabilities in Hall thrusters

It is well known that plasma pressure drives the instabilities in plasma. Therefore the confined plasma is prone to non-equilibrium thermodynamic state. Therefore it must be important to know the consequences of these instabilities. It has been established that the amplitude and frequency of the oscillations in the Hall thrusters depend on mass flow rate, discharge voltage, geometry, magnetic field profile and

cathode operation mode. On the other hand, the plasma in a Hall thruster does not stay uniform, and an inhomogeneous plasma immersed in the external electric and magnetic fields is not in the thermodynamically equilibrium state; this deviation in general is a source of plasma instabilities.

In Hall thrusters, from low frequencies (few Hertz) to high frequencies (few GHz), oscillation spectra have been observed on theoretically as well as experimentally based studies. The oscillations in the range of 10–20 kHz are called as discharge oscillations, and oscillations in the range of 5–25 kHz are said to be ionization-driven oscillations. The drift instabilities and density gradient plasma are responsible to produce oscillations in the range of 20–60 kHz in a Hall thruster. The oscillations in the range of 70–500 kHz are also called transient time oscillations and are the order of ion residence time in the channel of the device. The oscillations associated with azimuthal waves are represented by high-frequency (0.5–5 MHz) oscillations [5]. Litvak and Fisch [6] have developed an analytical model for electrostatic and electromagnetic resistive instabilities in a Hall plasma for azimuthal disturbances. Singh and Malik investigated resistive instabilities for axial and azimuthal disturbances in a Hall thrusters [7, 8]. Fernandez et al. [9] did simulations for the growth of resistive instability. Litvak and Fisch [10] have analysed gradient-driven Rayleigh-type instabilities in a Hall thruster using two fluid hydrodynamic equations. Ducrocq et al. [11] have investigated high-frequency electron drift instability in the cross-field configuration of a Hall thruster. Barral and Ahedo [12] have developed a low-frequency model of breathing oscillations in Hall discharges, where they observed that unstable modes are strongly nonlinear and are characterized by frequencies obeying a scaling law different from that of linear modes. Chesta et al. [13] have developed a theoretical model to obtain the growth rate and frequencies of axial and azimuthally propagating plasma disturbances.

3. Studies of fine particles in plasma

The presence of heavy fine particles with a size of 1–50 microns and mass of orders 10^{-10} to 10^{-15} kg in a classical plasma acts as a external component in plasma. If the density of the dust particles is less than the plasma density, the system is called dusty plasma. These fine particles acquire some charges from the electrons to get charged. The magnitude of charge on dust grain is not constant. It depends on the type of dust grain, the surface properties of dust grain, the dust dynamics, the temperature, the density of plasma and the wave motion in the medium.
The presence of fine particles in a plasma makes it more complex and these particles alter the dynamics of the plasma species which generate new propagating modes by exhibit their own dynamics. The dusty plasmas have an exciting property which has attracted researchers over the world in this area [14–22]. The presence of charged dust grains modifies the ion-acoustic waves, lower hybrid waves, ion-acoustic and introduces dust acoustic waves and dust ion acoustic waves [22]. Verma et al. have studied the electrostatic oscillation in the presence of grain charge perturbation in a dusty plasma [23]. They studied the property of electrostatic oscillation and instability phenomena taking into account the temporal evolution of the grain charge in an unmagnetized dusty plasma. Cui and Goree have studied the effect of fluctuations of the charge on a dust grain in plasma [24]. Sharma and Sugawa studied the effect of ion beam on dust charge fluctuations [25]. It is observed that growth rate of the instability increases with the relative density of negatively charged dust.
If dust particle charge is eZ_d. The quasineutrality condition is given for dust particles by $n_{e0} = n_{i0} + Z_d n_{d0}$.

4. Electron plasma discharge oscillation

When electrons are displaced from the equilibrium position of the charged particles relative to the uniform background of the ions in plasma, an electric field is developed in such a direction that it tries to pull the electrons back to its equilibrium position to restore the neutrality. Because of the inertia effect, the electrons overshoot the equilibrium position, and now the electric field is developed in the opposite direction which again tries to pull back the electrons to their position of equilibrium. The massive ions are supposed to be fixed in the background and are not capable to respond the oscillating field generated by the oscillation of electrons. If n_0 is the number of electrons per unit volume in infinite sheet plasma of thickness x, let the electron be displaced (as shown in **Figure 2**) to the right from their equilibrium position which results to generate surface charge density $\sigma = en_0x$ on the left side of the sheet and equal and opposite surface charge density on the right side of the sheet. The generated electric field $\vec{E} = {}^{en_0x}/_{\varepsilon_0}$ tries to pull the electrons back, and thus oscillation takes place in plasma. From Newton's second law, we write $m_e \frac{d^2x}{dt^2} = -e\vec{E} = -\frac{e^2n_0x}{\varepsilon_0}$. Thus the solution of the above second-order differential equation is given by $x(t) = A\cos(\omega_{pe}t)$, where $\omega_{pe} = \sqrt{\frac{e^2n_0}{m_e\varepsilon_0}}$ is the plasma frequency or character frequency at which imbalance charges oscillate. Using the values of various parameters, plasma frequency f (Hz) for electron is in the order $\approx 9\sqrt{n_0}$(Hz), when the electron density is taken per m^3. For example, for plasma having an electron density of 10^{18}/m^3, we have $f \approx 9$ GHz. Generally the plasma frequency lies in the microwave region. The above equation also shows that group velocity of these oscillations is zero, and hence there is no propagation of information. These waves are called stationary waves.

5. Plasma oscillation when the motion of ions is also taken into account

Let x_1 and x_2 are the displacement from the equilibrium positions of electrons and ions, respectively, then the equation of motions is

$$m_e \frac{d^2x_1}{dt^2} = -\frac{e^2n_0(x_1 - x_2)}{\varepsilon_0} \tag{1}$$

$$m_i \frac{d^2x_2}{dt^2} = \frac{e^2n_0(x_1 - x_2)}{\varepsilon_0} \tag{2}$$

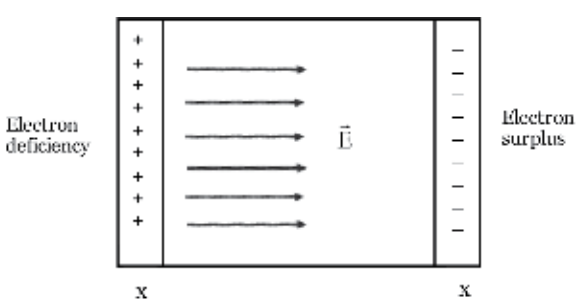

Figure 2.
Schematic of electron displacement in plasma sheet of thickness x.

By combining the above equations, we obtain

$$\frac{d^2(x_1 - x_2)}{dt^2} = -\frac{e^2 n_0 (x_1 - x_2)}{\varepsilon_0}\left(\frac{1}{m_e} + \frac{1}{m_i}\right) \tag{3}$$

or

$$\frac{d^2 X}{dt^2} = -\frac{e^2 n_0 X}{m_e \varepsilon_0}\left(1 + \frac{m_e}{m_i}\right) \tag{4}$$

where $X = x_1 - x_2$.
Therefore the frequency of oscillation is

$$\omega^2{}_{pie} = \frac{e^2 n_0}{m_e \varepsilon_0}\left(1 + \frac{m_e}{m_i}\right) = \omega^2{}_{pe}\left(1 + \frac{m_e}{m_i}\right) \tag{5}$$

5.1 Frequency of oscillation for pair plasma

The pair plasma comprise of particles with opposite charge but equal mass, which gives plasma frequency $\omega_{ie} = \sqrt{2}\omega_{pe}$.

6. Concept of plasma resistivity

The equation of motion for electron in unmagnetized cold plasma can be given by the equation $m\left(\frac{\partial \vec{v}_e}{\partial t} + \left(\vec{v}_e \cdot \vec{\nabla}\right)\vec{v}_e\right) = -e\vec{E} - mv\vec{v}_e$. In a steady state, the collisional friction balances the electric acceleration, and the above equation results to $\vec{E} = -\frac{mv\vec{v}_e}{e}$. Since electrons move with respect to the ions, they carry the current density $\vec{J} = -ne\vec{v}_e$. Substituting the current density into electric field equation yields $E = \eta J$. Here we have defined the plasma resistivity $\eta = \frac{mv}{ne^2}$. Therefore plasma resistivity depends on the collision frequency between the neutral particles with plasma species.

7. Plasma model and basic equations

A Hall thruster with two-component plasma consisting of ions and electrons is considered in which only the electrons are magnetized and the ions are not. For the case of simplicity, the presence of dust particles has been ignored; otherwise the mathematical expression would become cumbersome. In order to realize the exact behaviour and the consequences of finite temperature on the thruster efficiency, it is of much importance to investigate the plasma disturbances in Hall thrusters by including the finite temperatures of the plasma species.

As discussed in Section 1, the electrons experience force along the azimuthal direction, and ions are accelerated along the exit side of the device to produce thrust by the external electric field. We use the common symbols to write the continuity and equation of motion for the ions and electrons under the thermal effects of ion and electron pressure gradient forces. The collision momentum transfer frequency (v) between the electrons and neutral atoms is also taken into account to see the resistive effects in the plasma:

$$\frac{\partial n_i}{\partial t} + \vec{\nabla} \cdot \left(\vec{v}_i n_i\right) = 0 \tag{6}$$

$$\frac{\partial \vec{v}_i}{\partial t} + \left(\vec{v}_i \cdot \vec{\nabla}\right)\vec{v}_i = \frac{e\vec{E}}{M} - \frac{\vec{\nabla} p_i}{M n_i} \tag{7}$$

$$\frac{\partial n_e}{\partial t} + \vec{\nabla} \cdot \left(\vec{v}_e n_e\right) = 0 \tag{8}$$

$$\frac{\partial \vec{v}_e}{\partial t} + \left(\vec{v}_e \cdot \vec{\nabla}\right)\vec{v}_e = -\frac{e}{m}\left(\vec{E} + \vec{v}_e \times \vec{B}\right) - v\vec{v}_e - \frac{\vec{\nabla} p_e}{m n_e} \tag{9}$$

8. Linearization of fluid equations

We consider the perturbed densities for ions and electrons as n_{i1} and n_{e1} velocities as $\vec{v}_{i1}$ and $\vec{v}_{e1}$ indicated by subscript 1 along with their unperturbed values as v_0 and u_0 in the X and Y directions respectively. The unperturbed part represents the state of the plasma in the absence of oscillations and is indicated by a subscript 0. The unperturbed density is taken as n_0, the electric field (magnetic field) as $\vec{E}_0(\vec{B}_0)$ and the perturbed value of the electric field (magnetic field) as $\vec{E}_1(\vec{B}_1)$. To linearize all the equations, let us write $n_i = n_0 + n_{i1}$, $\vec{v}_i = \vec{v}_{i1} + \vec{v}_0$, $\vec{B} = \vec{B}_1 + \vec{B}_0$ and $\vec{E} = \vec{E}_1 + \vec{E}_0$. In view of small variations of both the density and magnetic field along the channel, the plasma inhomogeneities are neglected. The perturbations of the ion and electron densities are taken small enough $(n_{i1}, n_{e1} << n_0)$ so that the collisional effect due to the velocity perturbations dominate over the one due to the density perturbation. Since $\vec{v}_0$ and u_0 are constant, the terms $\left(\vec{v}_0 \cdot \vec{\nabla}\right)n_0$, $n_0\left(\vec{\nabla} \cdot \vec{v}_0\right)$ and $n_1\left(\vec{\nabla} \cdot \vec{v}_0\right)$ are equal to zero. Further the terms $\left(\vec{v}_1 \cdot \vec{\nabla}\right)n_1$ and $n_1\left(\vec{\nabla} \cdot \vec{v}_1\right)$ are neglected as they are quadratic in perturbation. The linearized form of the above equations thus reads

$$\frac{\partial n_{i1}}{\partial t} + v_0 \frac{\partial n_{i1}}{\partial x} + n_0\left(\vec{\nabla} \cdot \vec{v}_{i1}\right) = 0 \tag{10}$$

$$\frac{\partial \vec{v}_{i1}}{\partial t} + v_0 \frac{\partial \vec{v}_{i1}}{\partial x} = \frac{e\vec{E}_1}{M} - \frac{\vec{\nabla} p_i}{M n_0} \tag{11}$$

$$\frac{\partial n_{e1}}{\partial t} + u_0 \frac{\partial n_{e1}}{\partial y} + n_0\left(\vec{\nabla} \cdot \vec{v}_{e1}\right) = 0 \tag{12}$$

$$\frac{\partial \vec{v}_{e1}}{\partial t} + u_0 \frac{\partial \vec{v}_{e1}}{\partial y} = -\frac{e}{m}\left(\vec{E}_1 + \vec{v}_{e1} \times \vec{B}_0 + \vec{u}_0 \times \vec{B}_1\right) - v\vec{v}_{e1} - \frac{\vec{\nabla} p_e}{m n_0} \tag{13}$$

The initial drifts v_0 and u_0 of the ions and electrons in the channel are related to the electric and magnetic fields according to $v_0 \frac{\partial v_0}{\partial x} = \frac{eE_0}{M}$ and $u_0 = -\frac{E_0}{B_0}$ obtained from the unperturbed part of Eqs. (7) and (9). The electron pressure in Eqs. (9) and (13) is given by $p_e = Y_e n_e T_e$ together with T_e as the electron temperature, which we consider to be constant, and Y_e as the ratio of specific heats.

Normal mode analysis: We seek the sinusoidal solution of the above equations; therefore the perturbed quantities are taken as $f_1 \sim \exp\left(i\omega t - i\vec{k} \cdot \vec{r}\right)$. Then the

time derivative $(\partial/\partial t)$ can be replaced by $i\omega$ and the gradient $\vec{\nabla}$ by ik. Here $f_1 \equiv n_{i1}, n_{e1}, \vec{\upsilon}_{i1}, \vec{\upsilon}_{e1}, \vec{E}_1$ and $\vec{B}_1$ together with ω as the frequency of oscillations and $\vec{k}$ as the propagation vector.

9. Dispersion equation and growth rate of electrostatic oscillations

Since, we are only interested in electrostatic oscillations, and therefore in the meanwhile, the perturbed magnetic field can be ignored in Eq. (13). By using Fourier analysis in Eq. (10) and Eq. (13), the perturbed ion and electron densities are given as follows:

$$n_{i1} = \frac{n_0}{(\omega - k_x \upsilon_0)}\left(k_x \upsilon_{i1x} + k_y \upsilon_{i1y}\right) \tag{14}$$

$$n_{e1} = \frac{n_0}{(\omega - k_y u_0)}\left(k_x \upsilon_{e1x} + k_y \upsilon_{e1y}\right) \tag{15}$$

Using Eq. (11) into Eq. (14) gives

$$n_{i1} = \frac{ek^2 n_0 \varphi}{M(\omega - k_x \upsilon_0)^2}\left(1 - \frac{k^2 {V_{thI}}^2}{(\omega - k_x \upsilon_0)^2}\right)^{-1} \tag{16}$$

where we used $k^2 = {k_x}^2 + {k_y}^2$.

The expression for the electron density n_{e1} contains the velocity components υ_{e1x} and υ_{e1y}, which are derived in terms of the potential φ under the assumption $\Omega >> \omega$, $k_y u_0$ and υ in view of the oscillations observed in Hall thrusters [13, 22, 23]. Letting $\omega - k_y u_0 - i\upsilon \equiv \hat{\omega}$, $\frac{eB_0}{m} \equiv \Omega$, $\sqrt{\frac{Y_e T_e}{m}} \equiv V_{th}$, $\sqrt{\frac{n_0 e^2}{m\varepsilon_0}} \equiv \omega_e$ and $\sqrt{\frac{n_0 e^2}{M\varepsilon_0}} \equiv \omega_i$.

we use Eq. (13) to write the velocity components

$$i\left(\omega - k_y u_0 - i\upsilon\right)\upsilon_{e1x} = \frac{e}{m}\frac{\partial \varphi}{\partial x} - \Omega \upsilon_{e1y} + \frac{ik_x n_{e1} {V_{thE}}^2}{n_0} \tag{17}$$

$$i\left(\omega - k_y u_0 - i\upsilon\right)\upsilon_{e1y} = \frac{e}{m}\frac{\partial \varphi}{\partial y} + \Omega \upsilon_{e1x} + \frac{ik_y n_{e1} {V_{thE}}^2}{n_0} \tag{18}$$

Further simplification gives

$$\begin{aligned} \upsilon_{e1x} = {} & \frac{1}{m\Omega^2}\left(iek_y\Omega\varphi - \frac{im\hat{\omega}k_x {V_{thE}}^2 n_{e1}}{n_0} + k_x\hat{\omega}e\varphi - \frac{im\Omega k_y {V_{thE}}^2 n_{e1}}{n_0}\right) \\ & + \frac{i\hat{\omega}^2}{m\Omega^3}\left(ek_y\varphi - \frac{mk_y {V_{thE}}^2 n_{e1}}{n_0}\right) \end{aligned} \tag{19}$$

$$\begin{aligned} \upsilon_{e1y} = {} & \frac{1}{m\Omega^2}\left(\frac{imk_x {V_{thE}}^2 \Omega n_{e1}}{n_0} + k_y\hat{\omega}e\varphi - ik_x\Omega e\varphi - \frac{m\hat{\omega}k_y {V_{thE}}^2 n_{e1}}{n_0}\right) \\ & + \frac{i\hat{\omega}^2}{m\Omega^3}\left(\frac{mk_x {V_{thE}}^2 n_{e1}}{n_0} - k_x e\varphi\right) \end{aligned} \tag{20}$$

With the above velocity components, the perturbed electron density n_{e1} can be expressed in terms of perturbed potential as follows:

$$n_{e1} = \frac{en_0\hat{\omega}k^2\varphi}{m\Omega^2(\omega - k_y u_0) + m\hat{\omega}k^2 V_{thE}{}^2} \tag{21}$$

Finally, we use the expressions for the perturbed ion density n_{i1} and electron density n_{e1} in Poisson's equation $\varepsilon_0\nabla^2\varphi = e(n_{e1} - n_{i1})$ in order to obtain

$$-k^2\varphi = \frac{\omega_e{}^2\hat{\omega}k^2\varphi}{\Omega^2(\omega - k_y u_0) + \hat{\omega}k^2 V_{thE}{}^2} - \frac{\omega_i{}^2 k^2\varphi}{(\omega - k_x v_0)^2 - k^2 V_{thI}{}^2} \tag{22}$$

Since the perturbed potential is $\varphi \neq 0$, we have from Eq. (21)

$$\frac{\omega_e{}^2\hat{\omega}}{\Omega^2(\omega - k_y u_0) + \hat{\omega}k^2 V_{thE}{}^2} + \frac{(\omega - k_x v_0)^2 - k^2 V_{thI}{}^2 - \omega_i{}^2}{(\omega - k_x v_0)^2 - k^2 V_{thI}{}^2} = 0 \tag{23}$$

This is the dispersion relation that governs the electrostatic waves in the Hall thruster's channel.

9.1 The limiting case

For smaller oscillations, that is, $\omega << |k_y u_0|$, the above relation yields

$$(\omega - k_x v_0)^2 = \frac{(k_y u_0 + iv)\begin{bmatrix} k^2 V_{thI}{}^2\omega_e{}^2 \\ +k^2 V_{thE}{}^2(\omega_i{}^2 + k^2 V_{thI}{}^2)\end{bmatrix} + \Omega^2 k_y u_0(\omega_i{}^2 + k^2 V_{thI}{}^2)}{(k_y u_0 + iv)(\omega_e{}^2 + k^2 V_{thE}{}^2) + \Omega^2 k_y u_0} \tag{24}$$

Now, using the conditions $\Omega < \omega_e > \omega_i$ and $V_{thI} << V_{thE}$ in the above equation and letting $\omega_1 = \sqrt{\frac{(\Omega^2\omega_i{}^2 + \omega_e{}^2 k^2 V_{thI}{}^2)}{(\Omega^2 + \omega_e{}^2)}}$,

$$(\omega - k_x v_0)^2 \approx \omega_1{}^2 \frac{\left[1 + \frac{iv\omega_i{}^2 k^2 V_{thE}{}^2}{k_y u_0(\Omega^2\omega_i{}^2 + \omega_e{}^2 k^2 V_{thI}{}^2)}\right]}{\lfloor 1 + \frac{iv\omega_e{}^2}{k_y u_0(\Omega^2 + \omega_e{}^2)}\rfloor} \tag{25}$$

Since the last terms in the second brackets of the numerator and denominator in the right-hand side of Eq. (25) are small, we obtain the following

$$\omega - k_x v_0 \approx \pm\omega_1\left[1 + \frac{ivk^2 V_{thE}{}^2\omega_i{}^2}{2k_y u_0(\Omega^2\omega_i{}^2 + \omega_e{}^2 k^2 V_{thI}{}^2)}\right]\lfloor 1 - \frac{iv\omega_e{}^2}{2k_y u_0(\Omega^2 + \omega_e{}^2)}\rfloor \tag{26}$$

10. Instability analysis

The roots ω_j of the above polynomial may be real and/or complex number. For a real root, sinusoidal behaviour gives $\exp\left(i\omega_j t - i\vec{k}\cdot\vec{r}\right)$ showing an oscillatory

behaviour. For complex roots which always occur in complex conjugate, we write $\omega_j = \omega_{rj} - i\gamma_j$, where ω_{rj} and γ_j are real numbers and the sinusoidal behaviour becomes $e^{t\gamma_j} \exp\left(i\omega_{rj}t - i\vec{k}\cdot\vec{r}\right)$ which is showing an exponentially growing wave for a positive value of γ_j or an exponentially damped wave for a negative value of γ_j. Since the complex roots always appear in a conjugate pair, i.e. we have both negative and positive values of γ_j simultaneously. Hence, for the complex roots, one of the waves is always unstable.

Finally, the growth rate γ of the resistive instability is calculated from Eq. (26) as below:

$$\gamma \approx \frac{v\omega_1}{2k_y u_0}\left[\frac{\omega_e{}^2}{\Omega^2+\omega_e{}^2} - \frac{\omega_i{}^2 k^2 V_{thE}{}^2}{\Omega^2\omega_i{}^2 + \omega_e{}^2 k^2 V_{thI}{}^2}\right] \tag{27}$$

The corresponding real frequency is obtained as

$$\omega_r \approx k_x v_0 \pm \omega_1\left[1 + \frac{v^2 k^2 V_{thE}{}^2 \omega_i{}^2 \omega_e{}^2}{4k_y{}^2 u_0{}^2\left(\Omega^2+\omega_e{}^2\right)\left(\Omega^2\omega_i{}^2 + \omega_e{}^2 k^2 V_{thI}{}^2\right)}\right] \tag{28}$$

From Eq. (27), it is obvious that growth rate is directly proportional to the collisional (dissipative effects) frequency of the electrons which depends on various plasma parameters.

The results obtained in Eq. (27) matches with Litvak and Fisch [6] when the thermal effects become ignorable (i.e. $T_i = T_e = 0$). Under this situation, the growth rate takes the form

$$\gamma \approx \frac{v}{2k_y u_0}\sqrt{\frac{\Omega^2\omega_i{}^2}{\left(\Omega^2+\omega_e{}^2\right)}}\left[\frac{\omega_e{}^2}{\left(\Omega^2+\omega_e{}^2\right)}\right]. \tag{29}$$

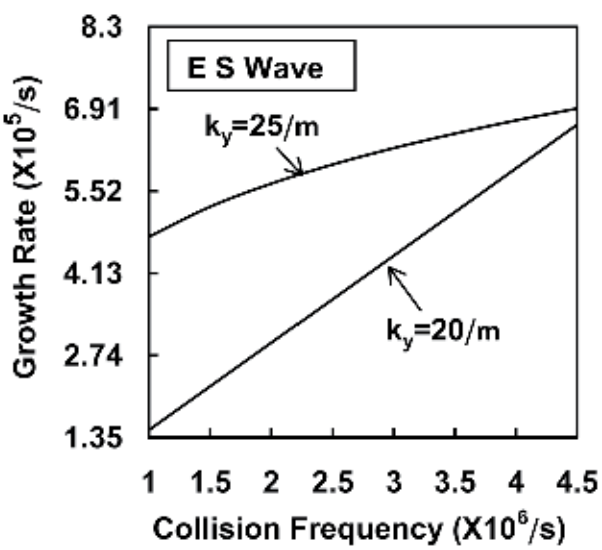

Figure 3.
Variation of growth rate γ with collision frequency for different values of azimuthal wave number in a plasma having Xe ions (M = 131 amu), when $T_e = 10$ eV, $n_o = 10^{18}/m^3$, $u_o = 10^6$ m/s and B = 0.02 T.

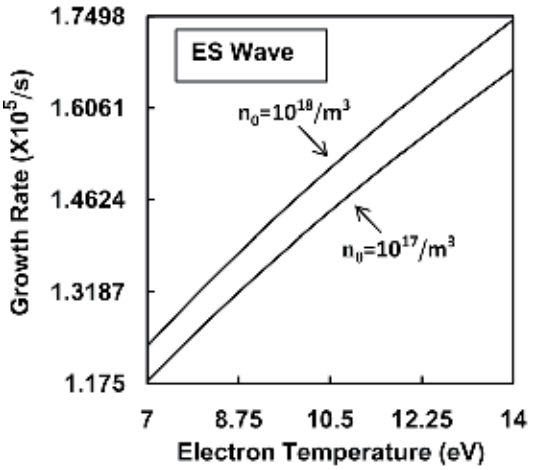

Figure 4.
Variation of growth rate γ with electron temperature for different values of plasma density in a plasma having Xe ions (M = 131 amu), when $v = 10^6$/s, $k_y = 20$/m, $u_o = 10^6$ m/s and $B = 0.02$ T.

In terms of lower hybrid frequency $\omega_{LH} = \sqrt{\frac{\Omega^2\omega_i^2}{\Omega^2+\omega_e^2}}$ and in the limit $\Omega << \omega_e$, the growth rate can be written as $\gamma \approx \pm\, \omega_{LH}\frac{v}{2k_y u_0}$.

The above relation matches with Eq. (21) of [6].

Since it is not possible to find an analytical solution of the above equation, we look for the numerical solution along with typical values of B_0, n_0, T_e, u_0, k_y, v and v_0. In Hall plasma thrusters, these parameters can have the values as thruster channel diameter = 4–10 cm, $B_0 = 100 - 200$ G, $n_0 = 5 \times 10^{17} - 10^{18}/\text{m}^3$, $T_e = 10 - 15$ eV, $u_0 \sim 10^6$ m/s, $v \sim 10^6$/s and $v_0 = 2 \times 10^4 - 5 \times 10^4$ m/s [6–10]. With regard to the value of k_y, we constraint $k_y = -m/r$ (where r is the radius of thruster channel) together with $m = 1$ for the azimuthal mode propagation [6, 7]. Accordingly we set $k_y = 20$/m; however, for higher mode (m > 1) or larger value of k_y, the wavelength would be much smaller than the azimuthal dimension of the channel. The variations of the resistive growth rate are seen in the figures by solving Eq. (23) numerically. Some propagating modes and instabilities with smaller growth are also observed during the analysis of Eq. (23).

Figure 3 confirms that the growth rate of the instability gets enhanced with the increase of collision frequency of the electrons due to the resistive coupling of the oscillations to the electron azimuthal drift. The growth rate also increases with the increase of the electron temperature (**Figure 4**), and it also increases with higher electron density of plasma. Therefore it can be concluded that the collisional effect is responsible to unstable the plasma system. The numerical value of the growth under the collision frequency is observed in the order of $\sim 10^5$/s.

11. Conclusions

In conclusions, we can say that the waves propagating in azimuthal and axial direction in a Hall thruster channel become unstable due to the resistive coupling to the electrons' $\vec{E} \times \vec{B}$ flow in the presence of their collisions. By controlling the various parameters, the growth rate and the propagating frequency of the oscillation may be controlled to optimize the performance and lifetime of the device.

Acknowledgements

The University Grants Commission (UGC), New Delhi, India, is thankfully acknowledged for providing the startup grant (No. F. 30-356/2017/BSR).

Author details

Sukhmander Singh
Plasma Waves and Electric Propulsion Laboratory, Department of Physics, Central University of Rajasthan, Ajmer, Kishangarh, India

*Address all correspondence to: sukhmandersingh@curaj.ac.in

References

[1] Ahedo E. Plasmas for space propulsion. Plasma Physics and Controlled Fusion. 2011;**53**(12):124037. DOI: 10.1088/0741-3335/53/12/124037

[2] Kaufman HR. Technology of closed-drift thrusters. AIAA Journal. 2012; **23**(1):78-86. DOI: 10.2514/3.8874

[3] Singh S, Malik HK. Resistive instabilities in a Hall thruster under the presence of collisions and thermal motion of electrons. The Open Plasma Physics Journal. 2011;**4**:16-23. DOI: 10.2174/1876534301104010016

[4] Boeuf JP, Garrigues LJ. Low frequency oscillations in a stationary plasma thruster. Journal of Applied Physics. 1998;**84**(7):3541-3554. DOI: 10.1063/1.36852

[5] Choueiri EY. Plasma oscillations in Hall thrusters. Physics of Plasmas. 2001; **8**(4):1411-1426. DOI: 10.1063/1.1354644

[6] Litvak AA, Fisch NJ. Resistive instabilities in Hall current plasma discharge. Physics of Plasmas. 2001; **8**(2):648-651. DOI: 10.1063/1.1336531

[7] Singh S, Malik HK, Nishida Y. High frequency electromagnetic resistive instability in a Hall thruster under the effect of ionization. Physics of Plasmas. 2013;**20**:102109

[8] Malik HK, Singh S. Resistive instability in a Hall plasma discharge under ionization effect. Physics of Plasmas. 2013;**20**:052115

[9] Fernandez E, Scharfe MK, Thomas CA, Gascon N, Cappelli MA. Growth of resistive instabilities in E×B plasma discharge simulations. Physics of Plasmas. 2008;**15**:012102

[10] Litvak AA, Fisch NJ. Rayleigh instability in Hall thrusters. Physics of Plasmas. 2004;**11**:1379-1382

[11] Ducrocq A, Adam JC, Heron A, Laval G. High-frequency electron drift instability in the cross-field configuration of Hall thrusters. Physics of Plasmas. 2006;**13**:102111

[12] Barral S, Ahedo E. Low-frequency model of breathing oscillations in Hall discharges. Physical Review E. 2009;**79**: 046401

[13] Chesta E, Meezan NB, Cappelli MA. Stability of a magnetized Hall plasma discharge. Journal of Applied Physics. 2001;**89**:3099-3107

[14] Resendes DP. Dipolar interaction in a colloidal plasma. Physical Review E. 2000;**61**(1):793

[15] Resendes DP, Mendonca JT, Shukla PK. Formation of dusty plasma molecules. Physics Letters A. 1998; **239**(3):181-186

[16] Resendes DP, Shukla PK. Self-excited oscillations of charged dust grains in the plasma sheath. Physica Scripta. 2001;**T89**:101

[17] Rosenberg M. Ion-and dust-acoustic instabilities in dusty plasmas. Planetary and Space Science. 1993; **41**(3):229-233

[18] Rosenberg M. Ion-dust streaming instability in processing plasmas. Journal of Vacuum Science & Technology, A: Vacuum, Surfaces, and Films. 1996;**14**(2):631-633

[19] Salimullah M, Shukla PK. On the stability of self-gravitating magnetized dusty plasmas. Physics of Plasmas. 1999; **6**(3):686-691

[20] Rao NN, Shukla PK, Yu MY. Dust-acoustic waves in dusty plasmas. Planetary and Space Science. 1990; **38**(4):543-546

[21] Pandey BP, Avinash K, Dwivedi CB. Jeans instability of a dusty plasma. Physical Review E. 1994;**49**(6):5599

[22] Shukla PK, Mamun AA, editors. Handbook of Introduction to Dusty Plasma Physics. Bristol: IOP Publishing; 2002. DOI: 10.1088/0741-3335/44/3/701

[23] Varma RK, Shukla PK, Krishan V. Electrostatic oscillations in the presence of grain-charge perturbations in dusty plasmas. Physical Review E. 1993;**47**(5): 3612

[24] Cui C, Goree J. Fluctuations of the charge on a dust grain in a plasma. IEEE Transactions on Plasma Science. 1994; **22**(2):151-158

[25] Sharma SC, Sugawa M. The effect of dust charge fluctuations on ion cyclotron wave instability in the presence of an ion beam in a plasma cylinder. Physics of Plasmas. 1999;**6**(2): 444-448

Edited by Aamir Shahzad

This book assists in the exchange of research and progress outcomes concerned with the latest issues in thermophysical properties (TPPs) of complex liquids research, development, and production. Topics cover the control of transport properties of metallic alloys, thermal analysis of complex plasmas and instabilities in plasma devices, thermophysical properties at nanolevel, theoretical background of viscosities of hydrocarbons at varying temperature and pressure ranges, molecular modeling, and experimental investigations based on nanofluids and ionic conduction in solid-state electrolytes for thermodynamic data. This book enables global researchers to tackle the challenges that continue to generate cost-effective TPPs and the latest understanding in the development of complex materials and the collaboration of modern thermophysical generating technologies. Moreover, it provides a platform for different regional authors to exchange scientific knowledge and generate enthusiasm for science and technology.

Published in London, UK

IntechOpen

ISBN 978-1-83880-458-9
9 781838 804589